

February 1989

Integration Effects of Pylon Geometry on a High-Wing Transport Airplane

(NASA-TP-2877) INTEGRATION EFFECTS OF PYLON
GEOMETRY ON A HIGH-WING TRANSPORT AIRPLANE
(1988) 70 p

183-103-1

CONF-88

CONF-88

1989-10-10

John R. Carlson
and Milton Lamb

**NASA
Technical
Paper
2877**

1989

Integration Effects of Pylon Geometry on a High-Wing Transport Airplane

John R. Carlson
and Milton Lamb
*Langley Research Center
Hampton, Virginia*

NASA
National Aeronautics and
Space Administration
Office of Management
Scientific and Technical
Information Division

Summary

A 1/24-scale wide-body high-wing transport model was tested in the Langley 16-Foot Transonic Tunnel at free-stream Mach numbers of 0.7 and 0.8 and angles of attack from -3° to 4° to determine the installation effects of a series of pylons that had differing cross-sectional shapes. Pylon toe angle was varied from 5° inboard to 5° outboard. A new concept in pylon cross-sectional shape, that is, a "compression" pylon, was developed and tested. This pylon was designed to reduce wing-pylon junction velocities and therefore reduce installed drag. Model aerodynamic forces and moments and wing static pressures were measured for the complete model configuration.

Results of the wind tunnel investigation show that the installed drag was lowest for the compression pylon design and the flow under the wing in the pylon-wing junction was kept comparable to clean wing velocities. The predicted trends in pylon side force and airplane drag with pylon toe angle compared marginally with the experimental data.

Introduction

For the United States aircraft industry to maintain its competitive position, future transport airplanes must perform substantially better than today's airplanes. The task of improving their performance is very demanding and will require the development and application of many new and innovative technologies. Among the technologies that must be improved are the methods used to install the engine on the airframe. The objective of airframe-propulsion integration research is to minimize the drag penalties (which can be as much as 3 to 5 percent of the aircraft drag) associated with integration of the engine and to develop possible methods of creating and taking advantage of favorable interference effects that may reduce the aircraft drag. The combination of advanced transport wings with thick supercritical airfoils and the larger high-bypass-ratio turbofans make the task of engine integration increasingly difficult, particularly because higher velocities occur in the leading edge region. This work will require an extensive integration program involving experimental studies and guidance from theoretical prediction methods.

The NASA Langley Research Center has initiated a program to study the effects of turbofan nacelle and pylon geometries on the interference drag associated with engine installation on transport configurations. Reference 1 presents data that illustrate how significantly the nacelle-pylon-wing geometry can affect interference drag. Alternate nacelle arrangements have

been studied for eliminating the unfavorable interference associated with engine installation. (See refs. 2 through 6.) A number of problems occur for the conventional pylon-mounted nacelle arrangement, which does not seem to lend itself to any obvious optimization procedure. Strong inboard and moderate outboard shocks and shock-induced flow separation on the pylon and wing are typically associated with this conventional arrangement. Pylon leading edge flow interacting with the wing upwash and sidewash, the adverse gradients in the wing stagnation region, and the channel flow with subsequent possible flow separation all contribute to the interference drag.

A previous investigation (unpublished) of a typical wing-pylon-nacelle installation, shown in figure 1, showed that much of the interference drag remained after removal of the nacelle. In addition, questions remained as to the side loading of the pylon and its relation to the total aircraft drag. Reference 1 presented the concept of allowing a properly contoured pylon to generate a lift force with a component in the thrust direction of the aircraft, as shown in figure 2. This concept could possibly reduce aircraft drag. As a result of these questions a series of wing-pylon configurations were developed and examined numerically using a current panel method in an attempt to correlate pylon toe angle with total airplane drag. In addition, a new concept in pylon cross-sectional shape, that is, "compression" pylon, was developed.¹ The design philosophy was twofold. First, in an attempt to reduce the local flow velocities in the wing-pylon junction, the pylon sides were made flat and continuously diverging for most of the pylon surface under the wing. Second, the pylon closure occurred aft of the wing trailing edge. The closure was actually enforced by the first design condition but further removed the pylon's adverse pressure gradient recovery region from the wing's trailing edge recompression region. This could have the added benefit of reducing the likelihood of flow separation in this region.

This paper presents the results of a wind tunnel experiment investigating the effects of pylon cross-sectional shape and pylon toe angle on airplane drag. Model aerodynamic forces and static pressures on the wing in the vicinity of the pylon were measured. The investigation was conducted in the Langley 16-Foot Transonic Tunnel at free-stream Mach numbers of 0.7 and 0.8 and angles of attack from -3° to 4° .

Symbols and Abbreviations

b wing span, 63.121 in.

¹ The authors would like to acknowledge J. Claude Patterson, Jr., for his initiating concepts in the development of the compression pylon design.

C_D	drag coefficient, $\text{Drag}/q_\infty S$
ΔC_D	installation drag, $C_{D_{WB P}} - C_{D_{WB}}$
C_L	lift coefficient, $\text{Lift}/q_\infty S$
C_p	pressure coefficient, $(p - p_\infty)/q_\infty$
C_p^*	critical pressure coefficient (local Mach number of 1.0)
C_Y	side force coefficient, $\text{Side force}/q_\infty S$
$C_{Y_{\text{pylon}}}$	side force coefficient on pylon
c	local chord measured in wing reference plane, in.
\bar{c}	mean aerodynamic chord, $\frac{2}{3} \left(c_r + c_t - \frac{c_r c_t}{c_r + c_t} \right)$, 9.107 in.
c_{av}	average wing chord, $\frac{c_r + c_t}{2}$, 8.390 in.
c_r	reference root chord at model centerline, 12.639 in.
c_t	reference tip chord, 4.142 in.
D	drag force, lb
N	normal force, lb
L	lift force, lb
M	free-stream Mach number
p	local static pressure, lb/in ²
p_∞	free-stream static pressure, lb/in ²
q_∞	free-stream dynamic pressure, lb/in ²
S	wing reference area, 529.59 in ²
T	thrust force, lb
x	local axial dimension, in.
y	local lateral dimension, in.
V	free-stream velocity, ft/sec
α	angle of attack, deg
η	semispan location, $2y/b$
Subscripts:	
B	aircraft body
exp	experimental
P	pylon

theory	calculated with VSAERO
W	wing

Abbreviations:

BL	butt line of model (lateral dimension), in.
FS	fuselage station (axial dimension from nose of model), in.
VSAERO	Vortex Separation Aerodynamic Program
WRP	wing reference plane

Experimental Apparatus and Procedures

Wind Tunnel

A high-wing transport model was tested in the Langley 16-Foot Transonic Tunnel to investigate the installation effects associated with pylons having various cross-sectional shapes. The tunnel is an atmospheric transonic single-return type with continuous air exchange and is capable of operation at Mach numbers from 0.2 to 1.3 with an accuracy of ± 0.005 . The average Reynolds number varies from approximately 1.46×10^6 per foot at a free-stream Mach number of 0.2 to approximately 4.10×10^6 per foot at a free-stream Mach number of 1.3. The test section is octagonal and slotted at the vertices and has an equivalent circular diameter of 15.9 ft. A detailed description of the tunnel is presented in reference 7.

Model and Support System

The 1/24-scale model, shown in figure 3, represents a wide-body high-wing transport with a thick supercritical airfoil. The model was mounted on a sting-supported six-component, strain-gauge balance. Details of the fuselage, wing, and wing pressure orifice locations can be found in references 2 and 4. A series of pylons with different cross-sectional shapes were installed on the wing without a nacelle attached. A close-up view from below of the pylon installation is shown in figure 4. The side force induced by the pylon was determined by removing the right-hand pylon and measuring the resulting asymmetric load. No significant side force was measured with the symmetrically mounted pylons; therefore the asymmetric side force measured on the model balance was taken to be the pylon-induced side force. The lift and drag data were obtained with both pylons installed on the wing.

The pylons were designed to extend 25 percent of the local wing chord below the wing at 37 percent

of the wing span. This was where previous nacelles and pylons have been installed. Each pylon had a 45° leading edge sweep with the leading and trailing edges being parallel. The pylon toe angle could be varied from +5° (leading edge toed inboard) to -5° (leading edge toed outboard). Six pylon cross-sectional shapes were tested, with the general design parameters shown in table 1. The wing planform and pylon cross-section and planform shapes are shown in figure 5, and the pylon airfoil coordinates are listed in table 2. The first three pylons were "conventionally" shaped consisting of an NACA 0012, an NACA 4412, and a contoured airfoil consisting of an NACA 0012 thickness distribution applied along a computed lower surface streamline. The second set of three pylons (designated A, B, and C) were of the compression pylon shape, with variations in divergence angle and length.

Instrumentation and Data Reduction

The model aerodynamic forces and moments were obtained by an internally mounted six-component strain-gauge balance. Model surface static pressures and sting cavity pressures were measured using electronically scanned pressure (ESP) sensors. The model angle of attack was computed by correcting the support strut angle both for sting deflections determined from balance loads and for tunnel upflow determined from inverted model runs in a previous tunnel entry. Sting cavity pressures were used to correct the longitudinal balance components for pressure forces in the sting cavity.

The accuracy of the angle-of-attack measurements was $\pm 0.02^\circ$. The accuracies of the force and pressure coefficients are presented in the following table:

	Coefficient error at—	
	$M = 0.7$	$M = 0.8$
Pressure coefficient	± 0.014	± 0.010
Normal force coefficient	$\pm .008$	$\pm .007$
Axial force coefficient	$\pm .0003$	$\pm .0003$
Side force coefficient	$\pm .002$	$\pm .002$

Tests

Data were obtained at free-stream Mach numbers of 0.7 and 0.8 and Reynolds numbers of approximately 2.5 million and 3.0 million based on the mean aerodynamic chord of the wing. The model angle of attack was varied from -3° to 4° . Boundary-layer transition on the model was fixed using grit transition

strips. A 0.1-in.-wide strip of No. 100 carborundum grit was attached 1.0 in. behind the nose of the fuselage. Strips of No. 90 and No. 80 grit were applied to the upper and lower wing surfaces, respectively, in rearward locations in order to better model the full-scale boundary-layer thickness at the trailing edge of the wing (ref. 8). A 0.1-in.-wide strip of No. 100 grit was attached 1.0 in. downstream and parallel to the pylon leading edge.

Computational Program and Modeling

The code used in part of this investigation was the Vortex Separation Aerodynamic Program (VSAERO) of reference 9. This method has been shown to be applicable to the prediction of some subsonic aerodynamic characteristics of a transport (for example, see refs. 10 and 11). VSAERO computes a surface singularity solution to the Laplace equation using quadrilateral panels to represent arbitrary three-dimensional bodies. Source and doublet singularities are distributed in a piecewise continuous fashion on each panel. Dirichlet boundary conditions are applied at the boundary to determine the doublet strength. A more detailed discussion of the method appears in reference 9.

This code includes features such as an iterative boundary-layer model, wake shape iteration, jet exhaust simulation, on- and off-body streamline calculations, and off-body velocity calculations. A major limitation in the use of the code is the incompressible nature of the basic equation. However, the subcritical results were adjusted for compressibility effects using a Prandtl-Glauert correction.

Approximately 700 panels were used to represent one-half of the aircraft model and VSAERO wing-wake models were attached to the trailing edges of the wing and pylon. The calculations performed were inviscid with rigid wakes. Total configuration drag and pylon side force were plotted versus pylon toe angle for a constant total configuration lift coefficient. Forces and moments were computed by VSAERO using pressure-area integration. For this investigation, the pylons did not actually intersect with the wing, but were butted to the lower surface. The calculations were performed with a 1000-panel version of VSAERO on a Control Data CYBER 170 series computer.

Presentation of Results

The aerodynamic force data presented are model lift, drag, and side force and are shown graphically. The pressure data obtained are from instrumentation just inboard and just outboard of the pylon. Data were obtained for two Mach numbers, 0.7 and 0.8,

the latter being the assumed cruise condition, and at nominal angles of attack from -3° to 4° ($C_L = 0$ to 0.80). Though the data at $C_L < 0.3$ are academic in nature, in that this would be an unusual condition for an airplane at these Mach numbers, these data show the sensitivity of the flow to off-design conditions.

Selected data are discussed and presented in the following figures:

Figure

Effect of pylon toe angle on airplane aerodynamic characteristics for conventional pylon shapes	6
Effect of pylon toe angle on airplane aerodynamic characteristics for compression pylon shapes	7
Effect of pylon toe angle on wing chordwise pressure distributions for conventional pylon shapes. $C_L \approx 0.5$	8
Effect of pylon toe angle on wing chordwise pressure distributions for compression pylon shapes. $C_L \approx 0.5$	9
Effect of pylon toe angle on selected aerodynamic characteristics at constant total airplane lift coefficient	10
Effect of conventional pylon shape on aerodynamic characteristics for pylon toe angle of 0°	11
Effect of compression pylon shape on aerodynamic characteristics for pylon toe angle of 0°	12
Effect of conventional pylon shape on wing chordwise pressure distributions for pylon toe angle of 0° . $C_L \approx 0.5$	13
Effect of compression pylon shape on wing chordwise pressure distributions for pylon toe angle of 0° . $C_L \approx 0.5$	14
Effect of pylon shape on wing chordwise pressure distributions. $C_L \approx 0.5$	15
Effect of pylon shape on incremental airplane drag for pylon toe angle of 0°	16

Results and Discussion

Effect of Pylon Toe Angle

The effects of pylon toe angle on selected model aerodynamic characteristics are shown in figures 6 and 7. Plots of model lift coefficient versus pylon side force are shown for the NACA 0012, NACA 4412, and compression type A pylons, and plots of lift coefficient versus drag coefficient are shown for all pylon configurations. Correspondingly, wing pressure distributions are shown in figures 8 and 9, at $M = 0.7$ and 0.8 for each pylon configuration.

Static pressure data were obtained on the wing over a range of pylon toe angle, but for greater clarity of the pressure distribution plots, only data for the clean wing and for 0° and maximum toe angles are presented. Data are also cross-plotted in figure 10 at a constant lift coefficient to provide pylon side force versus pylon toe angle and drag coefficient versus pylon toe angle for the NACA 0012, NACA 4412, and compression type A pylons.

Aerodynamic data for conventional pylons.

The effects on airplane lift and drag due to variation of the toe angle of the NACA 0012, the NACA 4412, and the contoured pylon (fig. 6) were generally similar in trend and showed small changes (typically less than 5 airplane drag counts) in level at the cruise lift coefficients ($C_L = 0.51$ at $M = 0.7$ and $C_L = 0.45$ at $M = 0.8$). Large deviations occurred, though, at the lower (i.e., off-design) lift coefficients where the polar curves separate widely for the NACA 0012 pylon (compare the separation of drag coefficient data symbols in figs. 6(a) and 6(b)). When comparing figures 6(a), 6(c), and 6(e) for $M = 0.7$ and figures 6(b), 6(d), and 6(f) for $M = 0.8$, note that the difference among the drag polars (generally for $C_L < 0.3$) lessened when the shapes progressed from the NACA 0012 to the NACA 4412 and then to the contoured pylon.

The effects of pylon toe angle on side force coefficient (figs. 6(a) to 6(d)) were similar, though different in level, between the NACA 0012 and NACA 4412 pylons. The side force coefficient curves at $M = 0.7$ were generally regular and displayed consistent trends of increasing outward (i.e., in the lateral direction from wing root to tip) force on the pylons as the pylon was set from a leading edge toed inward to a leading edge toed outward position. The slopes of the side force versus lift force did not significantly differ between these two pylons, though the absolute levels for the NACA 0012 pylon were consistently higher than those for the NACA 4412 pylon. This was not an unexpected result as the NACA 4412 airfoil camber line should have caused this pylon to "lift" more in the outboard direction at a given toe angle.

These trends in pylon side force (i.e., increasing outward force with pylon toe changing from inboard to outboard) do not change significantly at $M = 0.8$ for lift coefficients near cruise (i.e., $C_L \approx 0.45$). Though, it is interesting to note that at the lower lift coefficients ($C_L < 0.2$) the side force trend with pylon toe angle for the NACA 4412 pylon becomes somewhat chaotic. A significant change in the spanwise flow on the wing could cause this reversal in the pylon side force.

Aerodynamic data for compression pylons.

Figure 7 shows the effects on airplane lift and drag due to the installation of three compression pylons. In general, the trends observed for the compression pylons were similar to those for the conventional pylons, with smaller changes due to pylon toe angle. It is possible that these pylon shapes were less sensitive to the changes in the wing flow occurring at the lower lift coefficients (i.e., less divergence between the drag polars at the lower lift coefficients) or that changes in the flow due to the other pylon shapes did not occur with the compression contour. Consequently, the problems causing the polar divergences did not occur. As expected, the overall level of drag of the airplane increased for all three pylons at $M = 0.8$.

Compression pylon side force coefficients were obtained only for pylon A, shown in figures 7(a) and 7(b) for $M = 0.7$ and 0.8 , respectively. The side force trends with toe angle for pylon A at both Mach numbers were very similar to the trends observed for the NACA 0012 pylon, that is, an increasing outward force on the pylon as the leading edge is toed from inward to outward, and the general slope of the side force versus model lift force curves were similar.

Wing pressure data for conventional pylons. Upper and lower wing chordwise pressure coefficient distributions for the conventional pylons are shown in figure 8. Data for wing stations adjacent to the pylon (inboard and outboard of the pylon) for three pylon toe angles are plotted with data for the clean wing configuration at $M = 0.7$ and 0.8 . All the data were plotted at the model angle of attack that most closely matched a lift coefficient of 0.5 . In general, changes in the wing pressure distributions due to pylon installation were more substantial inboard of the pylon and less significant outboard of the pylon. Several other investigations have also shown this result (refs. 1 to 4). Furthermore, the changes in the wing pressure distributions, particularly due to variation of the pylon toe angle, were typically smaller on the wing upper surface than on the wing lower surface. Therefore, the following discussion concentrates on the influence of the pylon on the lower wing surface flow in the inboard region.

The installation of the NACA 0012 pylon (figs. 8(a) to 8(d)) caused expected acceleration of flow along the inboard wing station. Changing toe angle from $+5^\circ$ (toed in) to -5° (toed out) consistently reduced the local velocity peak under the wing leading edge with no significant effect on conditions downstream of $x/c = 0.4$. Presumably, as the pylon leading edge is toed outward, less surface curvature is encountered by the flow turning into the inboard wing-pylon junction, thus decreasing the flow

acceleration problem. The outboard wing lower surface (fig. 8(b)) would then have higher leading edge velocities, though much smaller change in magnitude, compared with the clean wing distribution. Somewhat similar results were observed for this pylon at $M = 0.8$ (figs. 8(c) and 8(d)) with the addition of strong wing lower surface shocks and possible separation, particularly for 5° toe in, where separation possibly occurred near $x/c = 0.3$ and again at $x/c = 0.5$. The generally flatter nature and poor pressure recovery trend of the wing lower surface pressure distributions at $M = 0.8$ (fig. 8(c)) from $x/c = 0.5$ to 1.0 indicate possible separation of the wing boundary layer for all three toe angles.

Variation of toe angle of the NACA 4412 pylon (figs. 8(e) to 8(h)) had similar, though typically lesser, effects on the wing pressure distributions, compared with the NACA 0012 pylon installation, for both $M = 0.7$ and $M = 0.8$. For $M = 0.7$ the highest lower surface flow acceleration occurred with pylon toe angle of 5° in. The velocity peak shifted upstream, from $x/c = 0.2$ for the NACA 0012 pylon to $x/c = 0.1$ for the NACA 4412 pylon (compare figs. 8(a) and 8(e)) and was smaller in magnitude. Though the leading edge velocity peaks were nearly equal in magnitude between the two pylons at $M = 0.8$, one notable feature of the NACA 4412 pylon installation was the improved pressure recovery (closely following the clean wing distribution) on the wing lower surface for $x/c > 0.4$ (compare figs. 8(g) and 8(c)). This is attributed to the NACA 4412 shape having less inboard surface curvature in the region of flow recompression ($x/c = 0.5$ to 1.0), which improved the recovery trend.

The wing pressure distributions for the contoured pylon, plotted in figures 8(i) to 8(l), show this pylon affecting the wing flow least of the conventional pylons. Note that the data are only for the range of toe angle from -2° to 2° . The typical suction peaks on the wing lower surface leading edge were roughly equal to those for the NACA 4412 pylon at $M = 0.7$ (compare figs. 8(i) and 8(e)), and were considerably suppressed at $M = 0.8$ (compare figs. 8(g) and 8(k)). The contoured and NACA 4412 pylons have very similar leading edge shapes so that fairly similar flows would be expected over the first 10 percent of the wing. The longer, flatter inboard side of the contoured shape tends to reduce the velocity perturbations over a larger fraction of chord, but the flow velocity levels are higher (fig. 8(i)) at $x/c = 0.2$ to 0.4 . Though this mixed result was not considered generally beneficial, because of the possible lift loss incurred, neither was the trailing edge pressure recovery adversely affected at $M = 0.7$. The data at $M = 0.8$ (fig. 8(k)) and $x/c = 0.65$

to 0.9, however, do indicate incipient separation of the wing boundary layer (compare clean wing data with installed pylon data). Typically, suppression of the lower surface flow velocity is desired to reduce the likelihood of flow separation near the leading edge with pylons installed. The trade-off that occurs is the increase in drag that is typical with the loss of wing leading edge suction.

Wing pressure data for compression pylons. Upper and lower wing chordwise pressure coefficient distributions for the compression pylon installations are shown in figure 9. Data for wing stations adjacent to the pylon (inboard and outboard of the pylon) for three pylon toe angles are plotted with data for the clean wing configuration at $M = 0.7$ and 0.8 . All the data were plotted at the model angle of attack that most closely matched a lift coefficient of 0.5 . Also note that for compression pylons A and C data are plotted for toe angles of -5° , 0° , and 5° , while for pylon B data are plotted for toe angles of -2° , 0° , and 5° .

The trends of the wing pressure distributions due to variation of toe angle for the compression pylons were similar to the changes observed previously for the conventional pylons, except that the degree of change was considerably smaller and these changes were fairly consistent from pylon to pylon. The mild departures of the installed pressure distribution from the clean wing distributions were relatively localized, typically occurring on the inboard row around $x/c = 0.1$ on the upper surface and around $x/c = 0.2$ to 0.3 on the lower surface at $M = 0.8$. This could contribute to a lower drag in that section. In general, the installation of these pylon types has not incurred the typical losses due to wing boundary-layer separation and excessive velocities, between $x/c = 0.1$ and 0.4 , observed for the conventional pylons.

Aerodynamic data at constant lift coefficient. The effect of pylon toe angle on pylon side force and total airplane drag is presented in figure 10. The data are plotted for the NACA 0012 pylon, the NACA 4412 pylon, and compression pylon A.

Preliminary investigations on the effects of pylon shape and toe angle were performed using VSAERO. These calculations indicated that minimum total airplane drag appeared to coincide with either zero pylon side force or minimum pylon side force. There was little useful agreement between the VSAERO calculations and the experimental data. Neither zero side force crossing nor the slopes matched (compare dashed lines with symbols) with different resulting conclusions. A contributing factor to the discrepancy between the theory and the data could be that

even at the lower Mach number of 0.7 , some regions of supersonic flow did occur, particularly in the leading edge areas of the wing, because of the angle of attack of the model and some pylon interference. Any additional drag effects due to supersonic regions of flow would not be accounted for by the method used. A more complete and detailed modeling of the wing-pylon junction might resolve some differences between the calculated and measured pylon loads.

The experimental data show a linear trend of pylon side force with toe angle for the three asymmetric pylons. The experimental data show that for the conventionally shaped pylons (figs. 10(a) and 10(b)), there is some loading of the pylon when airplane drag is a minimum. The minimum appears close to a toe angle of 0° for the NACA 0012 pylon at $M = 0.7$ and 0.8 , though data scatter and axial force accuracy make the minimum difficult to discern. Approximately 2° of leading edge toe in was required for minimum airplane drag with the NACA 4412 pylon (fig. 10(b)). At this point, the NACA 4412 pylon was loaded roughly twice as much as the NACA 0012 pylon. The toe angle at which minimum drag occurred was, again, about the same for both Mach numbers.

As can be seen in figure 10(c), the variation in the measured side force for compression pylon A had trends slightly different from those for the conventional pylons. At $M = 0.7$, the drag minimum coincided with zero pylon side force, that is, approximately 2° toe in, rather than the slightly loaded condition observed previously. The data at $M = 0.8$ show the pylon side force crossing occurring closer to 1° toe in, which coincides with a small shift in the minimum of the airplane drag plot.

Effect of Pylon Shape

Selected data, previously shown, are replotted to more easily show the effect of pylon shape on airplane aerodynamic characteristics and wing pressure coefficient distributions. All these figures show data for a pylon toe angle of 0° . Figures 11 and 12 show selected model aerodynamic data and figures 13 and 14 show wing pressure distributions for model data at $C_L \approx 0.5$. A direct comparison between wing pressure distributions for the NACA 0012 pylon and compression pylon A, at $M = 0.7$ and 0.8 , is shown in figure 15, and the effect of each pylon on incremental total airplane drag is plotted in figure 16.

Aerodynamic data for conventional pylons. The data at $M = 0.7$ show little effect of an installed pylon on the lift-curve slope (top part of fig. 11(a)) and little change, in lift-curve slope, from pylon to pylon, though there is some lift loss at all angles of attack due to the pylon installation. The NACA 4412

pylon (fig. 11) had generally the highest installed drag at both $M = 0.7$ and $M = 0.8$. The lower Mach number data, $M = 0.7$, showed little difference in the lift versus drag characteristics of the NACA 0012 and the contoured pylons, while the transonic data, $M = 0.8$, showed a crossover of these data (fig. 11(b)). The contoured pylon installation had less total drag at the lower lift coefficients, $C_L < 0.5$, as well as the lowest minimum drag, near $C_L = 0.17$, of the three conventionally shaped pylons.

Aerodynamic data for compression pylons.

No significant differences in the lift curve were observed among the compression pylons and clean wing-body configuration (fig. 12(a)). The lift loss, at a fixed angle of attack, incurred with the installation of the conventional pylons was not observed for the compression pylons. Some lift loss was observed at $M = 0.8$ (upper part of fig. 12(b)), though, as before, the effect was smaller than the conventional pylon installation effects. The thinnest pylon, B, had the least installed drag at both $M = 0.7$ and $M = 0.8$, and the drag curves for pylons A and C were similar in trend and level, but with slightly higher installed drag than pylon B, over the lift coefficient range.

Wing pressure data for conventional pylons. Figure 13 is a comparison of the effect of conventional pylon shape, for a toe angle of 0° , on wing pressure coefficient distributions. Upper and lower surface data are plotted at wing stations just inboard and outboard of the pylon, at $M = 0.7$ and 0.8 . All three pylon installations resulted in an acceleration of the wing upper surface leading edge flow (figs. 13(a) and (b)) at $M = 0.7$ and $x/c < 0.1$ to roughly the same level and do not appear to have had any adverse effects on the upper surface flow. As observed before, most of the pylon's influence at $M = 0.7$ was observed along the wing lower surface inboard of the pylon. The highest peak velocity, around $x/c = 0.2$, occurred with the NACA 0012 pylon installation because of the greater extent of pylon curvature in the leading edge region. Smaller velocity peaks typified the NACA 4412 and contoured pylon installations because of less curvature around the leading edge and a flatter inboard side. The NACA 4412 pylon had the least effect on the wing pressures downstream of $x/c = 0.35$ where the recovery in the lower surface cusp flow very closely matched that of the clean wing. This preserved the aft loaded nature of the supercritical airfoil more than the other two pylons. The favorable pressure distributions observed here seem to contradict the previous discussion concerning the aerodynamic data for a toe angle of 0° , where the NACA 4412 pylon installation had the highest installed drag (see fig. 11(a)). Though a

pylon may have beneficial (over other pylons) effects on the wing flow, the drag of the pylon itself can nullify these advantages. The NACA 4412 pylon was previously noted to have roughly twice as much side loading as the NACA 0012 pylon and a resulting increase in the induced drag (from the pylon "lifting") might be expected.

Comparisons of the wing pressure distributions at $M = 0.8$ (figs. 13(c) and (d)) show trends similar to those observed at $M = 0.7$. A relatively large leading edge flow velocity and possible lower surface flow separation, inboard of the pylon, characterize the NACA 0012 pylon installation. The "concave down" pressure recovery in the lower surface cusp region, $x/c = 0.55$ to 0.9 , indicates a thickening boundary layer and incipient separation. The contoured pylon suppressed the leading edge flow velocity at $x/c = 0.1$ to 0.2 , more than the NACA 4412 pylon, though the flow did not recover in the trailing edge region quite as strongly as for the NACA 4412 pylon.

Wing pressure data for compression pylons. Figure 14 is a comparison of the effect of compression pylon installations on wing pressure distributions. Upper and lower surface data are plotted at wing stations just inboard and outboard of the pylons at $M = 0.7$ and 0.8 . All data are for pylons set at a toe angle of 0° and a lift coefficient of approximately 0.5 . At $M = 0.7$ the largest effects due to this type of pylon installation (fig. 14(b)) occurred downstream of $x/c = 0.5$, on the wing lower surface outboard of the pylon. In this instance, a mild elevation of the wing flow velocities occurred because the compression pylon continued thickening toward the wing trailing edge, while in comparison, the conventional pylons were becoming thinner. Little change in this effect on the wing pressure distributions was observed from pylon to pylon. The data for $M = 0.8$ on the wing lower surface inboard of the pylon (fig. 14(c)) show a significantly slower and smaller region of supersonic flow, at $x/c = 0.2$ to 0.4 , due to pylon installation, as compared with the conventional pylon installation (see fig. 13(c)). As stated previously, the flat nature of the compression pylon appears to control the wing-pylon junction flow and suppress the typical velocity peaks present. Slightly elevated flow velocities outboard of the pylon on the wing lower surface were, as before, also observed at $M = 0.8$.

Comparison of conventional and compression pylons. Wing pressure coefficient data on the wing in the vicinity of the pylon for the NACA 0012 pylon, compression pylon A, and the clean wing are plotted in figure 15 at $C_L \approx 0.5$. Data at $M = 0.7$ are shown in figures 15(a) and 15(b) and at $M = 0.8$

are shown in figures 15(c) and 15(d). Typical of the more conventionally shaped pylons, the lower surface wing flow velocities increase on the inboard row from about $x/c = 0.2$ to 0.4 at both $M = 0.7$ and $M = 0.8$. Though, only at $M = 0.8$ did the flow exceed sonic speeds in that region with flow recovery via a moderate shock and incipient separation in the trailing edge region. The upper surface leading edge pressures were significantly lower at $M = 0.8$, with a shock at $x/c = 0.2$ and again at some point further downstream (though there were no experimental data plotted past $x/c = 0.4$, the flow must become subsonic at some later point because of the subsonic free-stream condition). Also fairly typical for conventional under-the-wing-mounted pylons was the relatively small effect on the flow on the outboard wing panel.

The inboard lower surface flow velocities for the compression pylon were much lower than those for the NACA 0012 pylon (fig. 15(a)). Though the flow velocities were still slightly higher than the clean wing data for the region from $x/c = 0.15$ to approximately 0.5 , the reduced curvature of the pylon shape prevented the extreme flow acceleration observed previously. The character of this flow was essentially the same as for the clean wing with only slight changes in the pressure recovery. The compression pylon increased the inboard upper surface flow velocity substantially for the first 40 percent of the wing chord because of the blockage of the spanwise flow spilling over the leading edge. This effect was still less than the velocity increase due to the NACA 0012 pylon. The leading edge of the compression pylon was much smaller than the NACA 0012 pylon and consequently presents less frontal surface in the wing leading edge region. No areas of excessive flow velocities or separation were observed for the compression pylon.

Incremental drag due to installing pylons.

The installed incremental drag coefficient (i.e., total airplane drag with pylons installed minus total airplane drag without pylons installed) is presented in figure 16 for $M = 0.7$ and 0.8 for all six of the pylon shapes tested. The shaded area indicates the amount of installed drag that may be attributed to calculated skin friction. The unshaded area represents the combined value of form, wave, and interference drag. Overall, the compression pylon series had a lower installed drag than the more conventionally shaped pylons. Compression pylon B was the same length as pylon A but with one-half the thickness, that is, 6 percent thick based on the local wing chord. Previous pylons tested, for example, in reference 6, were only as thin as 8 percent for a

conventional under-the-wing installation. Favorable interference due partially to the thinness and lack of curvature of pylon B resulted in this configuration having an incremental drag coefficient of less than skin friction drag of the pylon. Because the pylon was not instrumented, it is hard to be conclusive as to the reason for this result. Of the conventional pylons, the NACA 0012 shape had the lowest installed drag at $M = 0.7$ and the contoured pylon had the lowest at $M = 0.8$. Of the compression pylons, there was little difference between pylon A and the longer pylon C (150 percent of local wing chord in length, providing a smaller trailing edge closure angle).

Conclusions

An experimental investigation has been conducted in the Langley 16-Foot Transonic Tunnel at free-stream Mach numbers of 0.7 and 0.8 and angles of attack from -3° to 4° to determine the installation effects of a series of pylons that had differing cross-sectional shapes and to determine the effect of pylon toe angle on airplane drag. Six pylon shapes were studied: three conventional shapes (consisting of an NACA 0012, an NACA 4412, and a contoured shape) and three compression pylon shapes (with variation of divergence angle and length). The results are summarized as follows:

1. Conventionally shaped pylons show a large degree of adverse interference in the inboard wing-pylon junction in the form of moderate to large regions of supersonic flow and some evidence of mild flow separation due to the large curvature and pylon thickness in the leading edge region.
2. The compression pylon shape had the lowest pylon drag at both Mach 0.7 and Mach 0.8 . This shape was able to suppress the velocities in the inboard region of the pylon-wing junction and reduce the extent of supersonic flow and likelihood of flow separation through reduction in pylon curvatures and delay of the maximum thickness of the pylon further downstream of the wing leading edge region.
3. Conventional pylons were slightly loaded and compression pylons were unloaded when airplane drag appeared to be at a minimum at fixed lift coefficients. Data scatter and axial force accuracy made the effects of pylon toe angle on model drag difficult to discern.
4. Results predicted by VSAERO (Vortex Separation Aerodynamic Program) agreed poorly with the experimental side force and drag data. Inadequate modeling of the junction region, supercritical flow, and viscous effects likely contributed to the discrepancies encountered.

References

1. Henderson, William P.; and Patterson, James C., Jr.: Propulsion Installation Characteristics for Turbofan Transports. AIAA-83-0087, Jan. 1983.
2. Lee, Edwin E., Jr.; and Pendergraft, Odis C., Jr.: *Installation Effects of Long-Duct Pylon-Mounted Nacelles on a Twin-Jet Transport Model With Swept Supercritical Wing*. NASA TP-2457, 1985.
3. Henderson, William P.; and Abeyounis, William K.: *Aerodynamic Characteristics of a High-Wing Transport Configuration With an Over-the-Wing Nacelle-Pylon Arrangement*. NASA TP-2497, 1985.
4. Abeyounis, William K.; and Patterson, James C., Jr.: *Effect of Underwing Aft-Mounted Nacelles on the Longitudinal Aerodynamic Characteristics of a High-Wing Transport Airplane*. NASA TP-2447, 1985.
5. Putnam, Lawrence E.; Reubush, David E.; and Lee, Edwin E., Jr.: Effects of Over-the-Wing Pylon-Mounted Engines on Transport Airplane Performance. *Proceedings of the Workshop on Engine-Airframe Integration (Short-Haul Aircraft)*, S. N. B. Murthy, ed., Rep. No. PU-R1-78, Project SQUID Headquarters, Purdue Univ., May 1977, pp. 265-289.
6. Lamb, Milton; and Abeyounis, William K.: *Integration Effects of Underwing Forward- and Rearward-Mounted Separate-Flow, Flow-Through Nacelles on a High-Wing Transport*. NASA TM-87627, 1986.
7. Corson, Blake W., Jr.; Runckel, Jack F.; and Igoe, William B.: *Calibration of the Langley 16-Foot Transonic Tunnel With Test Section Air Removal*. NASA TR R-423, 1974.
8. Blackwell, James A., Jr.: *Preliminary Study of Effects of Reynolds Number and Boundary-Layer Transition Location on Shock-Induced Separation*. NASA TN D-5003, 1969.
9. Maskew, Brian: Prediction of Subsonic Aerodynamic Characteristics: A Case for Low-Order Panel Methods. *J. Aircr.*, vol. 19, no. 2, Feb. 1982, pp. 157-163.
10. Lord, W. K.; and Zysman, S. H.: VSAERO Analysis of a Wing/Pylon/Nacelle Configuration. AIAA-86-1523, June 1986.
11. Yaros, Steven F.; Carlson, John R.; and Chandrasekaran, Balasubramanyan: *Evaluation of Three Numerical Methods for Propulsion Integration Studies on Transonic Transport Configurations*. NASA TM-87727, 1986.

Table 1. Pylon Configuration Data

Pylon type	Length, percent <i>c</i>	Thickness, percent <i>c</i>	Leading edge divergence, deg	Trailing edge closure, deg
NACA 0012	100	12		
NACA 4412	100	12		
Contoured	100	12		
Compression A	125	12	2.4	19.5
Compression B	125	6	.7	10.9
Compression C	150	12	2.4	10.0

Table 2. Pylon Airfoil Coordinates

$[c = 9.972 \text{ in. } (\eta = 0.37)]$

(a) NACA 0012 pylon

x/c	y/c
0	0
.0125	.01894
.0250	.02615
.0500	.03555
.0750	.04200
.1000	.04683
.1500	.05345
.2000	.05738
.2500	.05941
.3000	.06002
.4000	.05803
.5000	.05294
.6000	.04563
.7000	.03664
.8000	.02623
.9000	.01448
.9500	.00807
1.0000	0

Table 2. Continued

(b) NACA 4412 pylon

x/c	y/c (inboard)	y/c (outboard)
0	0	0
.0125	-.0143	.0244
.0250	-.0195	.0339
.0500	-.0249	.0473
.0750	-.0274	.0576
.1000	-.0286	.0659
.1500	-.0288	.0789
.2000	-.0274	.0880
.2500	-.0250	.0941
.3000	-.0226	.0976
.4000	-.0180	.0980
.5000	-.0140	.0919
.6000	-.0100	.0814
.7000	-.0065	.0669
.8000	-.0039	.0489
.9000	-.0022	.0271
.9500	-.0016	.0147
1.0000	0	0

Table 2. Continued

(c) Contoured pylon

x/c	y/c (inboard)	y/c (outboard)
0	0	0
.0125	-.01430	.02440
.0250	-.01950	.03390
.0500	-.02400	.04730
.0750	-.02400	.05760
.1000	-.02400	.06590
.1500	-.02400	.07890
.2000	-.02400	.08800
.2500	-.02400	.09410
.3000	-.02400	.09760
.4000	-.02403	.09203
.5000	-.02294	.08294
.6000	-.02063	.07063
.7000	-.01464	.05864
.8000	-.00523	.04723
.9000	.00952	.03848
.9500	.01693	.03307
1.0000	.02800	.02800

Table 2. Continued

(d) Compression pylon A

x/c	y/c
0	0
.0013	.0067
.0050	.0117
.0109	.0152
.0188	.0174
.0283	.0187
.0394	.0195
.0500	.0200
.1260	.0232
.2057	.0266
.3719	.0336
.5382	.0406
.7044	.0476
.8707	.0546
.9115	.0562
.9522	.0577
.9930	.0585
1.0338	.0578
1.0745	.0541
1.1153	.0459
1.1561	.0332
1.1839	.0234
1.2117	.0136
1.2394	.0037
1.2500	0

Table 2. Continued

(e) Compression pylon B

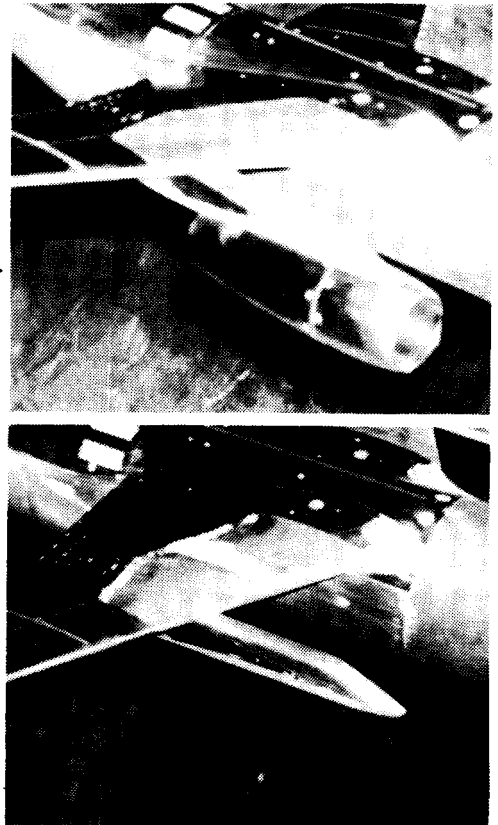
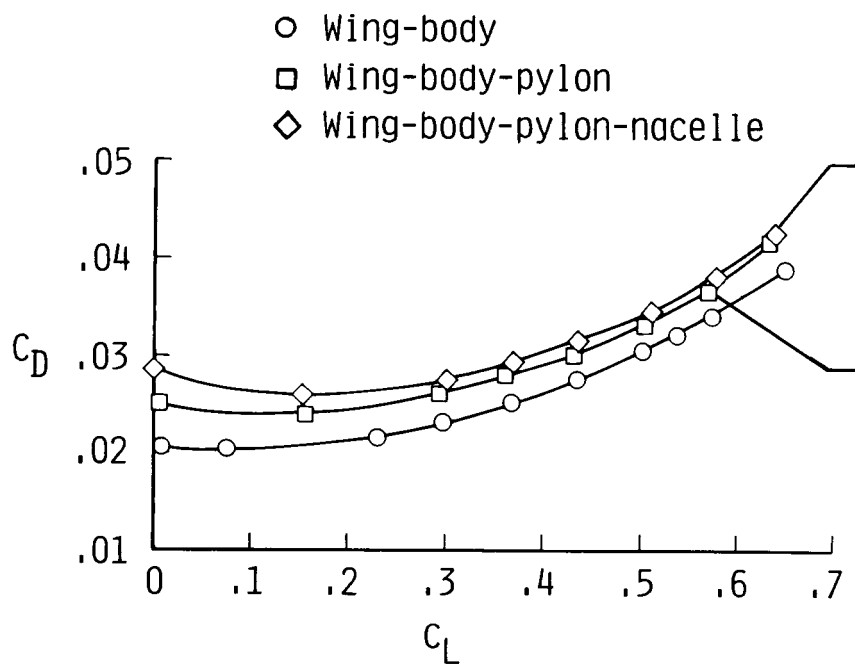
x/c	y/c
0	0
.0013	.0072
.0050	.0126
.0109	.0161
.0188	.0183
.0283	.0194
.0394	.0198
.0500	.0200
.2057	.0219
.3719	.0239
.5382	.0259
.7044	.0279
.8707	.0299
.9115	.0304
.9522	.0308
.9930	.0311
1.0338	.0308
1.0745	.0290
1.1153	.0248
1.1561	.0180
1.1839	.0127
1.2117	.0073
1.2394	.0020
1.2500	0

Table 2. Concluded

(f) Compression pylon C

x/c	y/c
0	0
.0013	.0067
.0050	.0117
.0109	.0152
.0188	.0174
.0283	.0187
.0394	.0195
.0500	.0200
.2057	.0266
.3719	.0336
.5382	.0406
.7044	.0476
.8707	.0546
.9353	.0570
.9998	.0580
1.0644	.0571
1.1290	.0543
1.1936	.0494
1.2582	.0417
1.3228	.0312
1.3783	.0215
1.4339	.0117
1.4894	.0019
1.5000	0

ORIGINAL PAGE IS
OF POOR QUALITY



L-83-8543 & L-83-9109

Figure 1. Installation effects of pylon and of pylon-nacelle. $M = 0.8$.

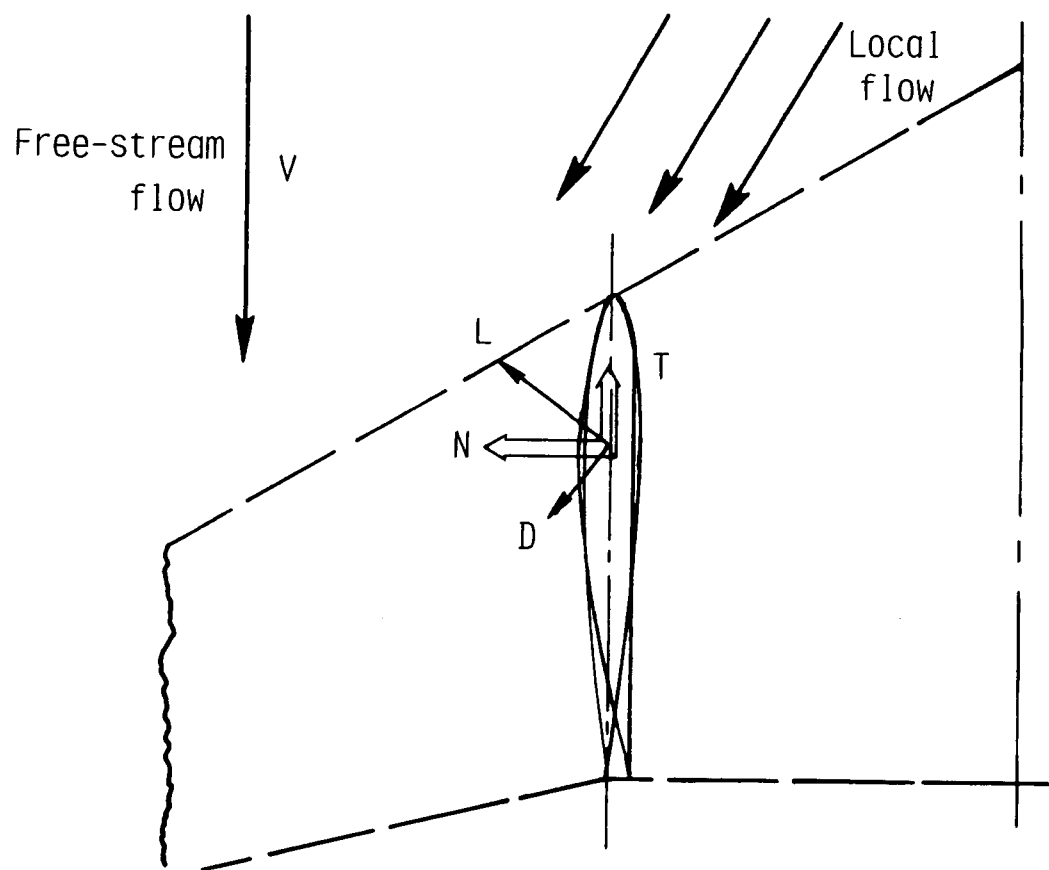
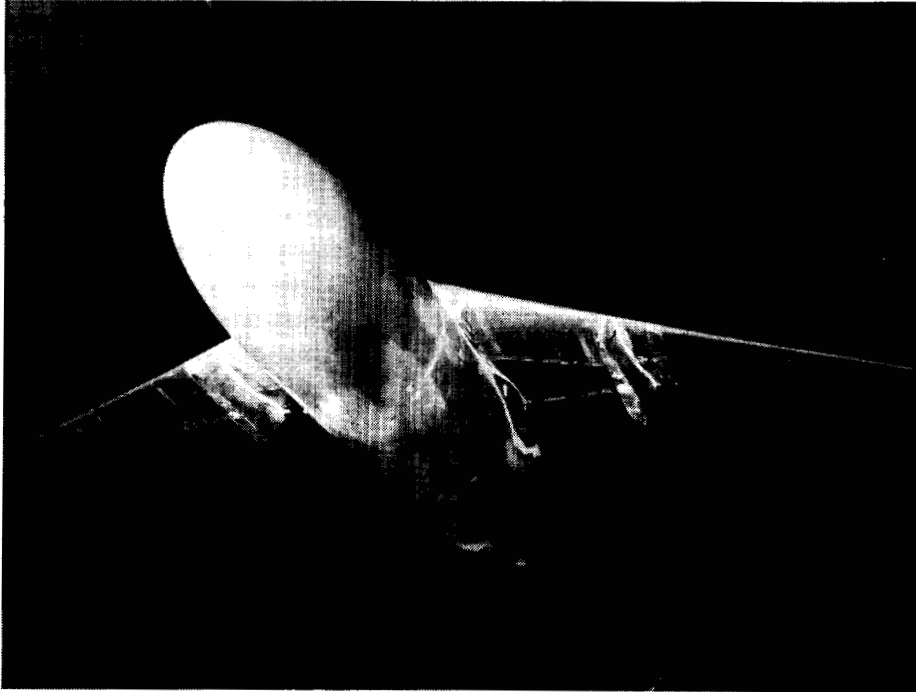


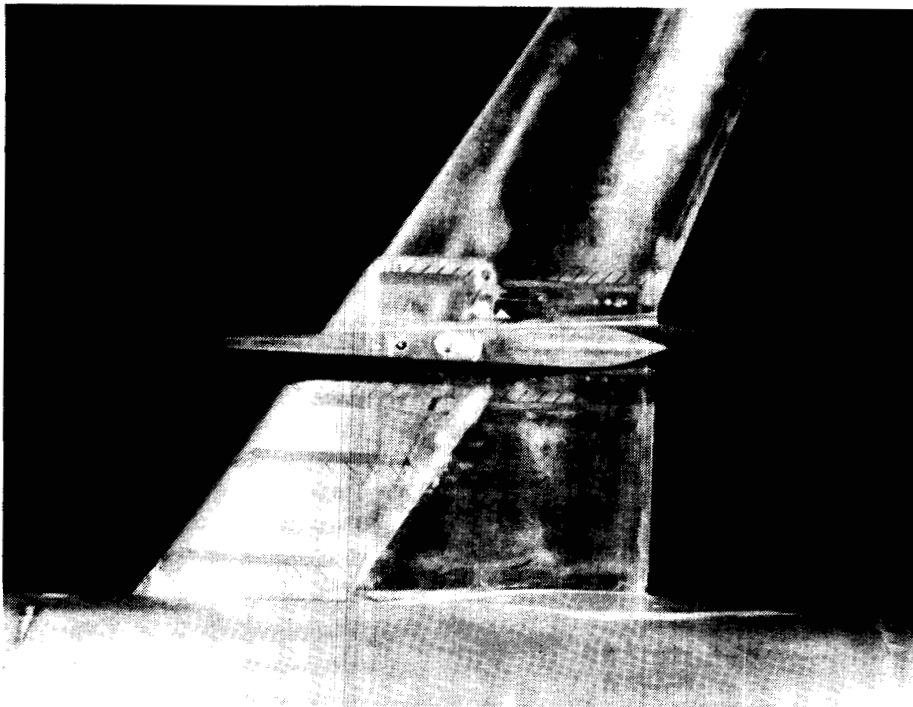
Figure 2. Illustration of interaction between local flow and pylon.

ORIGINAL PAGE IS
OF POOR QUALITY



L-86-11390

Figure 3. Model with pylons in Langley 16-Foot Transonic Tunnel.



L-89-15

Figure 4. View from below the wing of the pylon installation on the wind tunnel model.

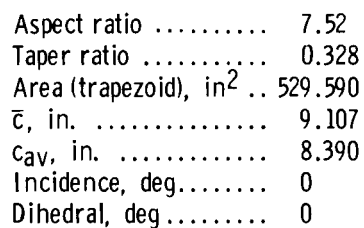
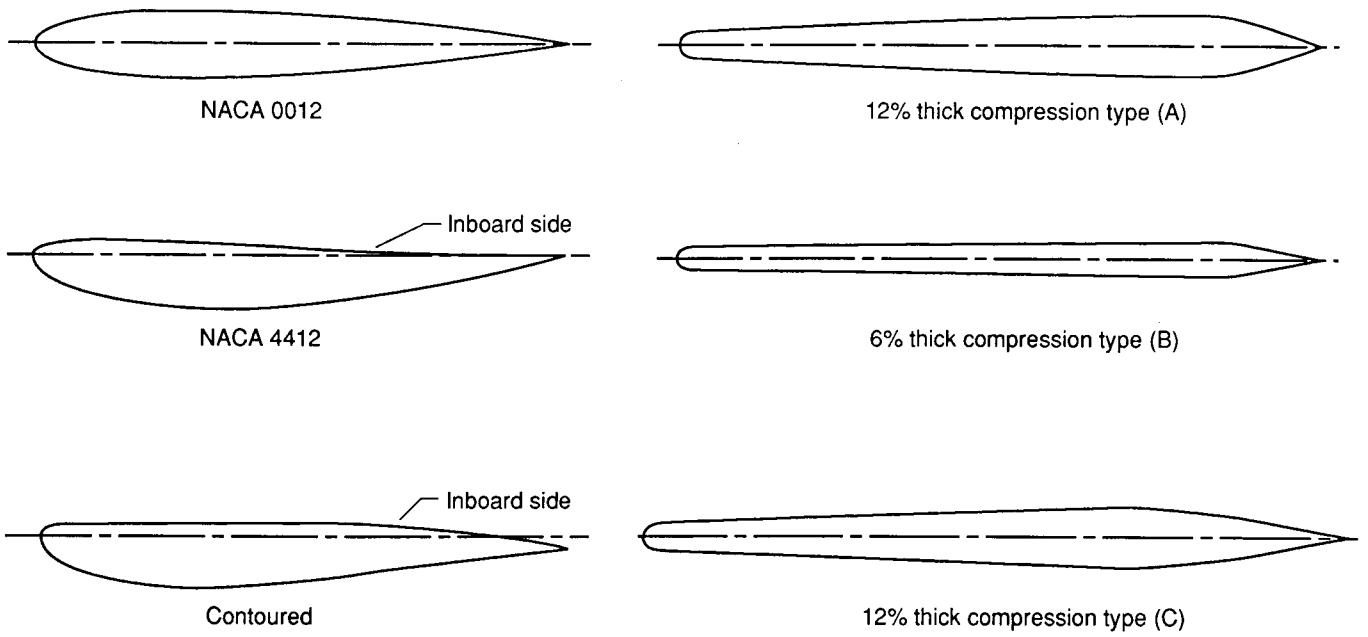
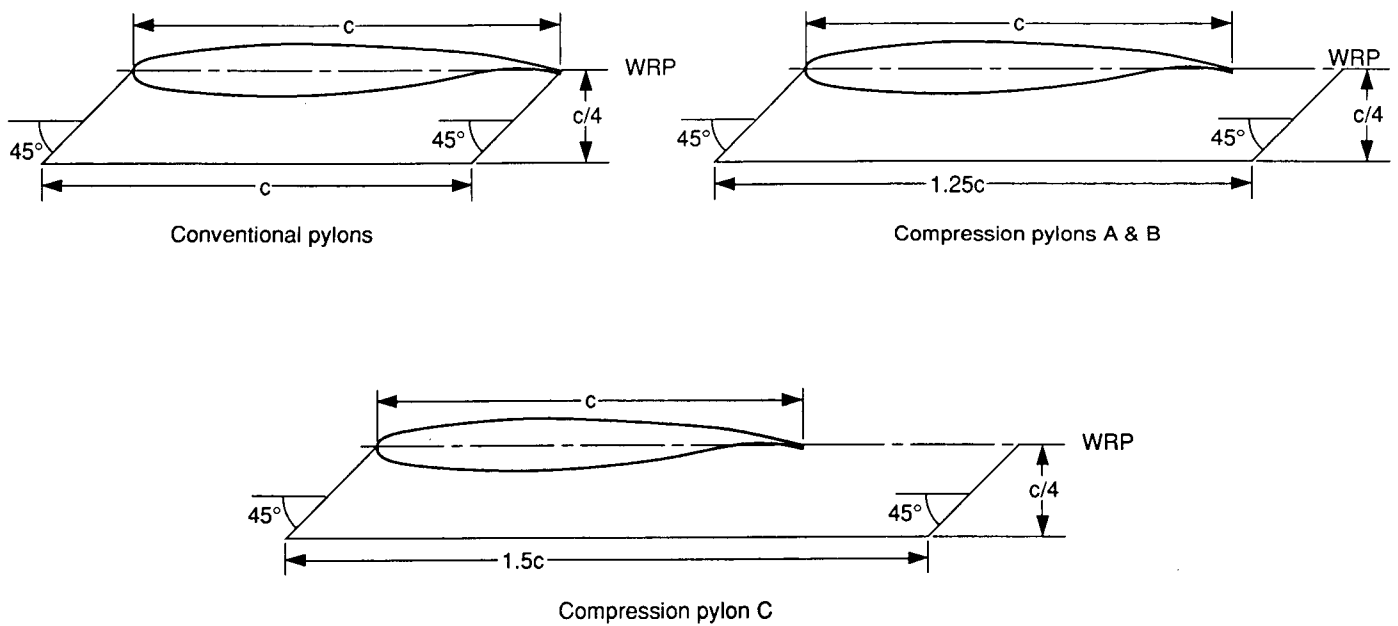


Figure 5. Wing and pylon geometry.

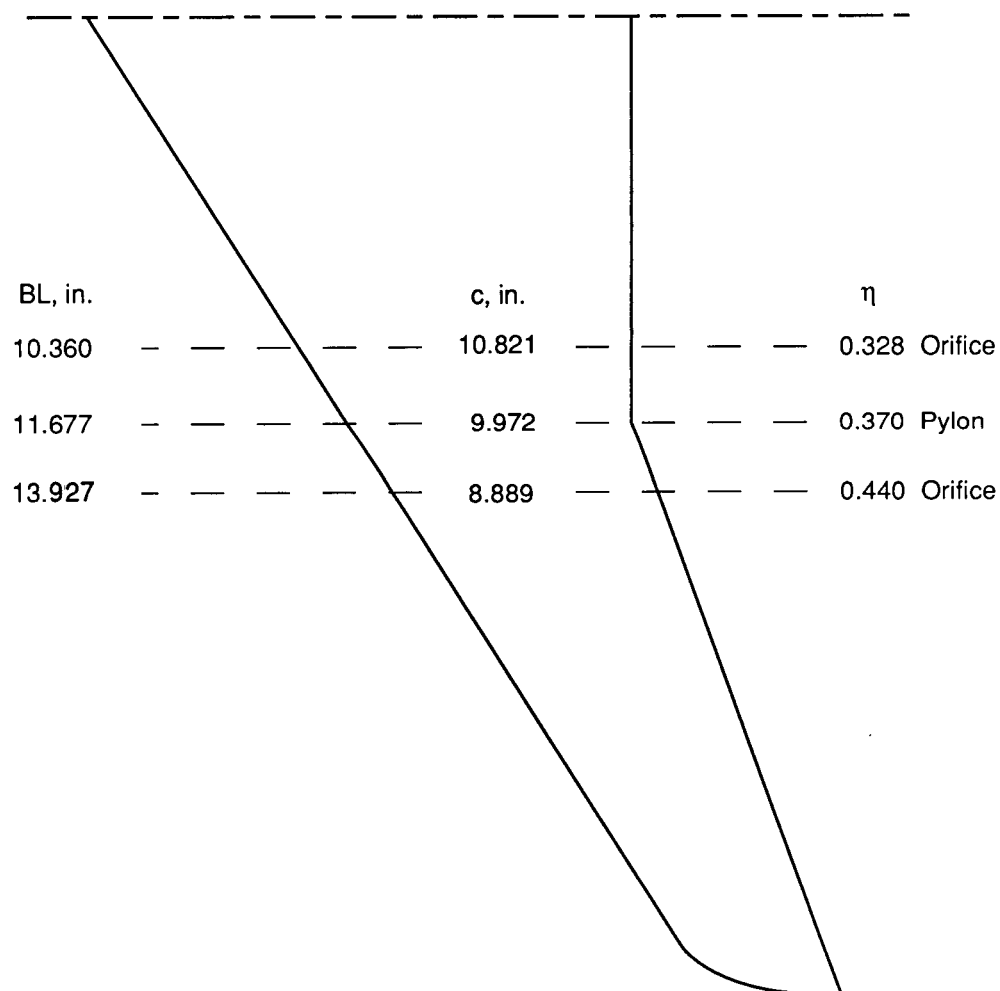


(b) Pylon cross-sectional shapes.



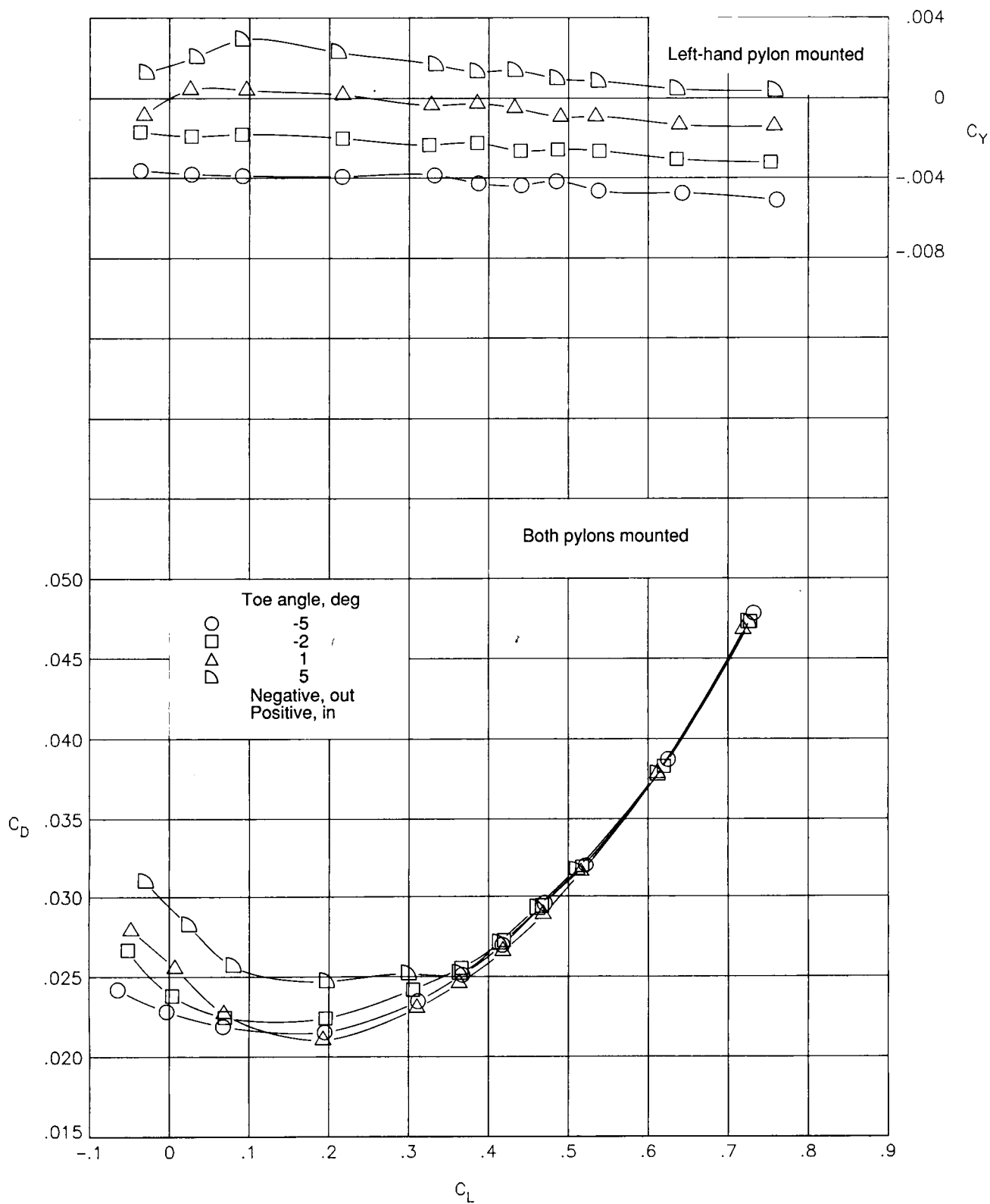
(c) Pylon planform shapes.

Figure 5. Continued.



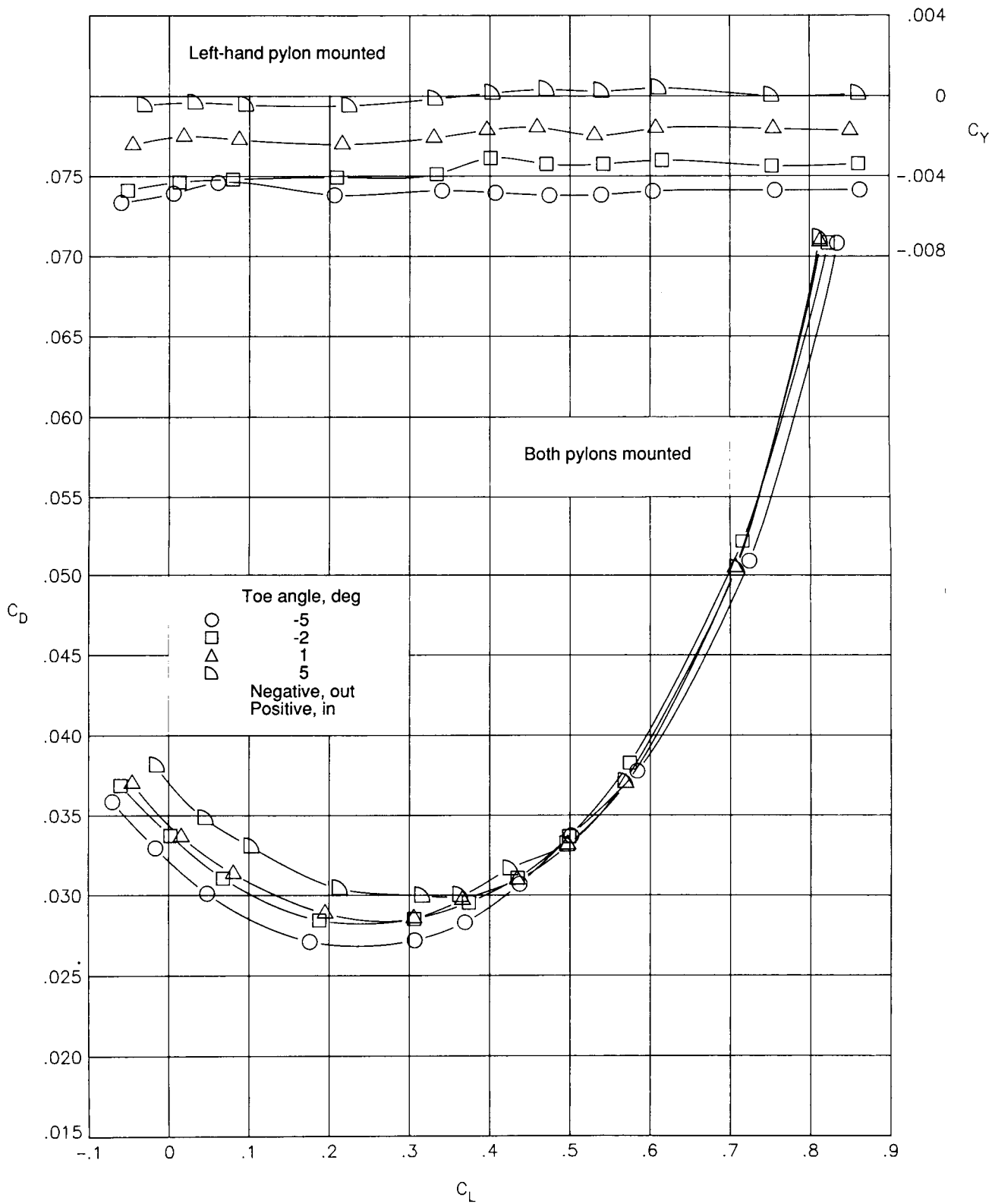
(d) Wing pressure-orifice row locations and pylon placement.

Figure 5. Concluded.



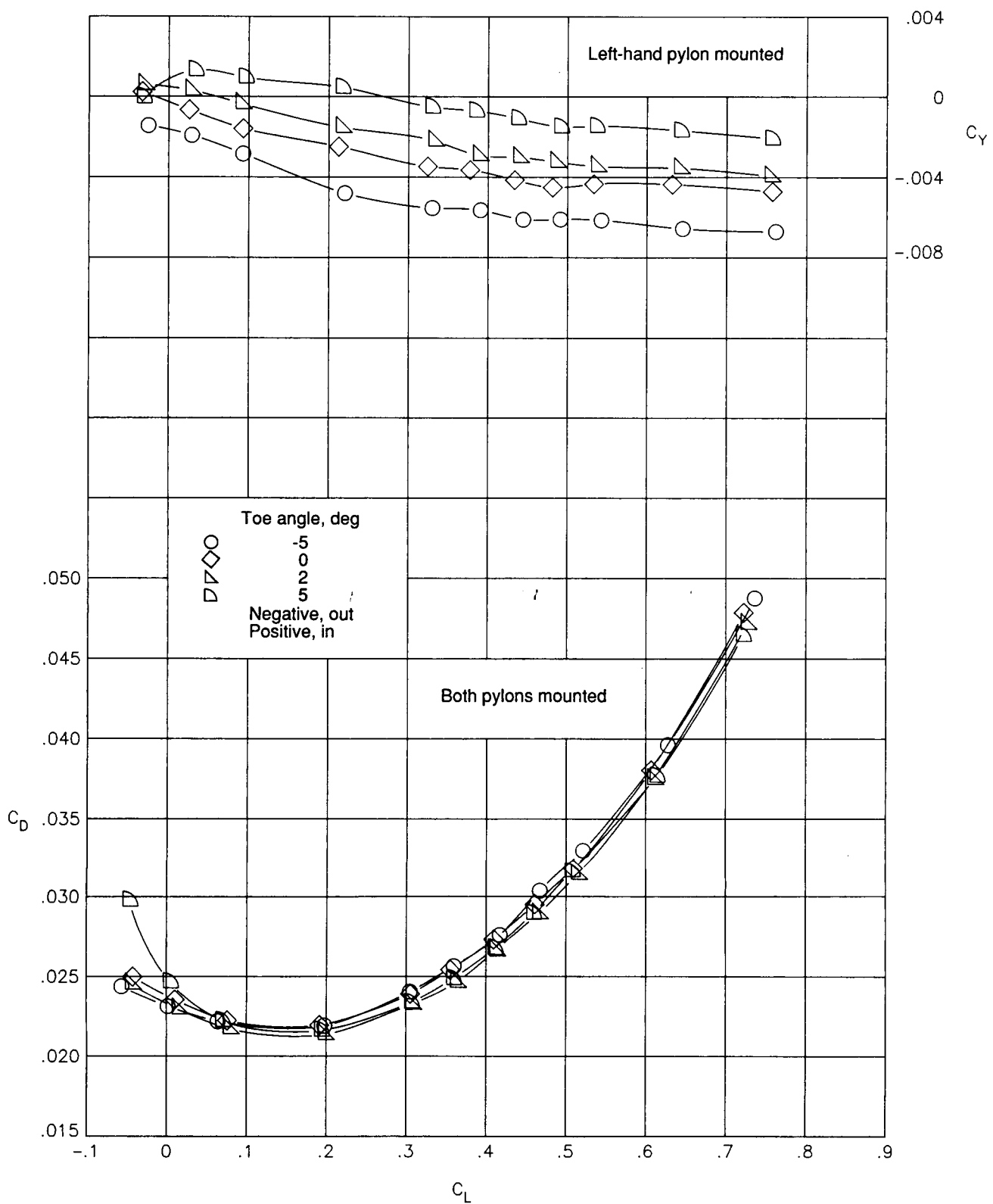
(a) NACA 0012 pylon; $M = 0.7$.

Figure 6. Effect of pylon toe angle on airplane aerodynamic characteristics for conventional pylon shapes.



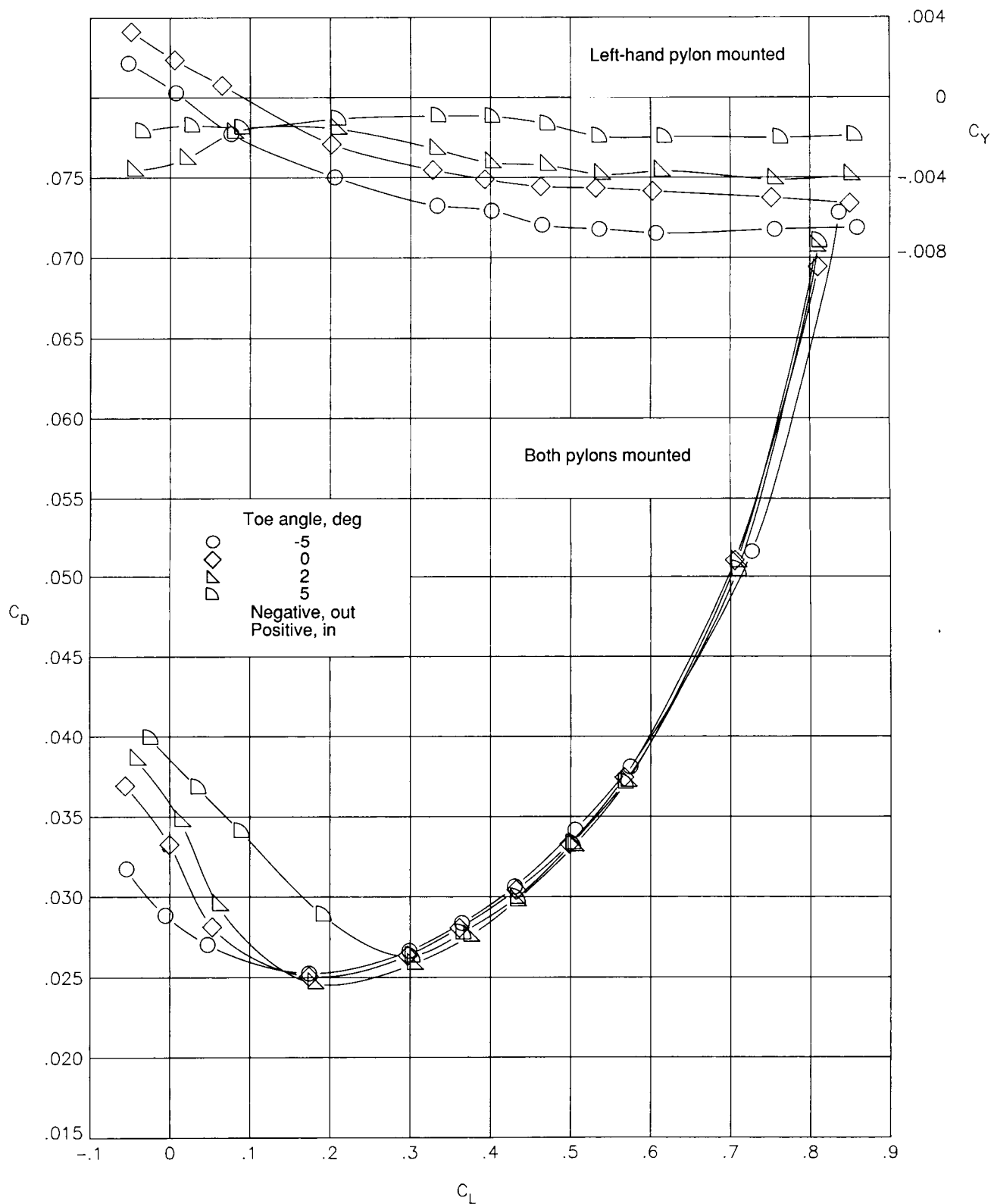
(b) NACA 0012 pylon; $M = 0.8$.

Figure 6. Continued.



(c) NACA 4412 pylon; $M = 0.7$.

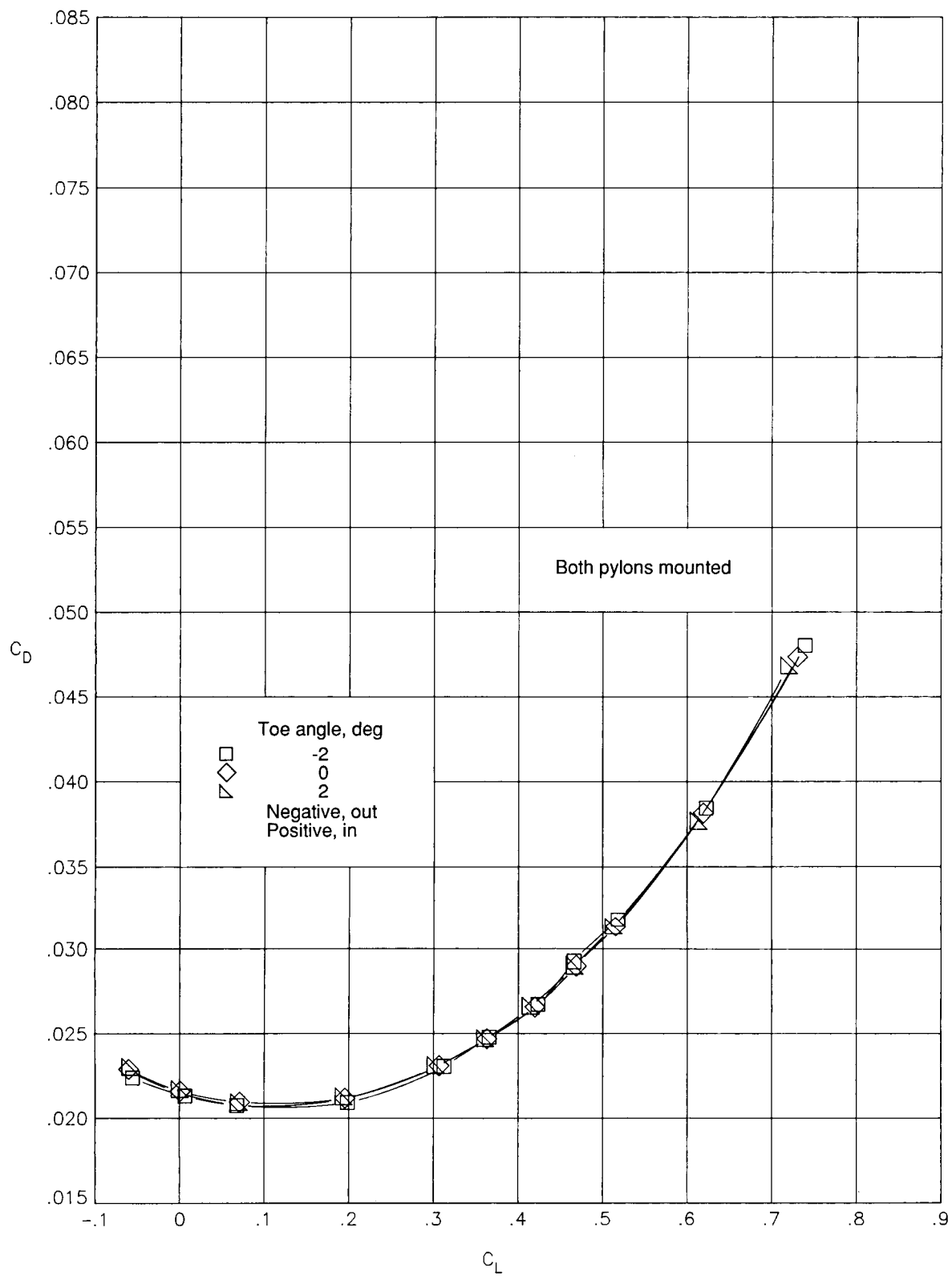
Figure 6. Continued.



(d) NACA 4412 pylon; $M = 0.8$.

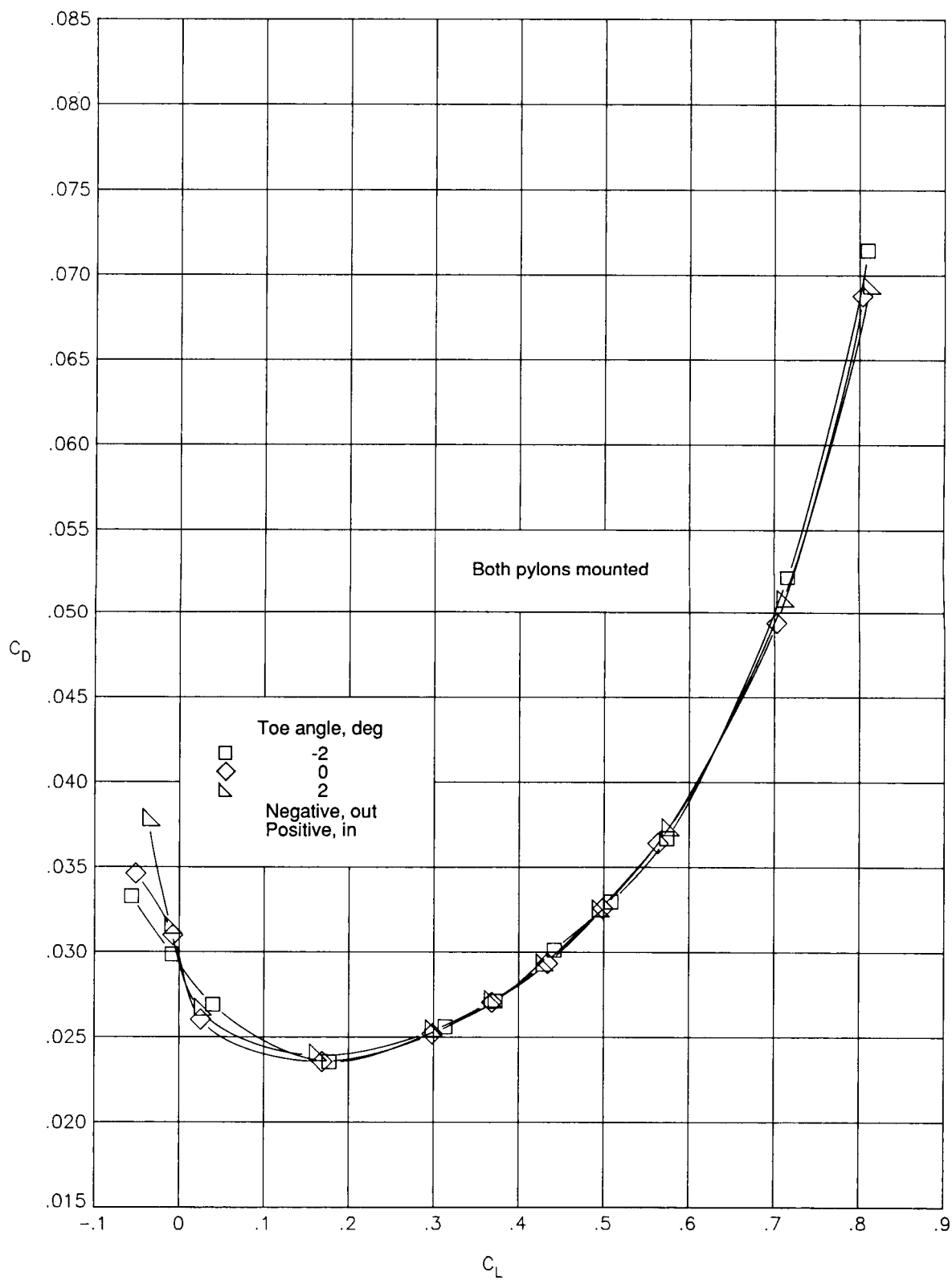
Figure 6. Continued.

ORIGINAL PAGE IS
OF POOR QUALITY



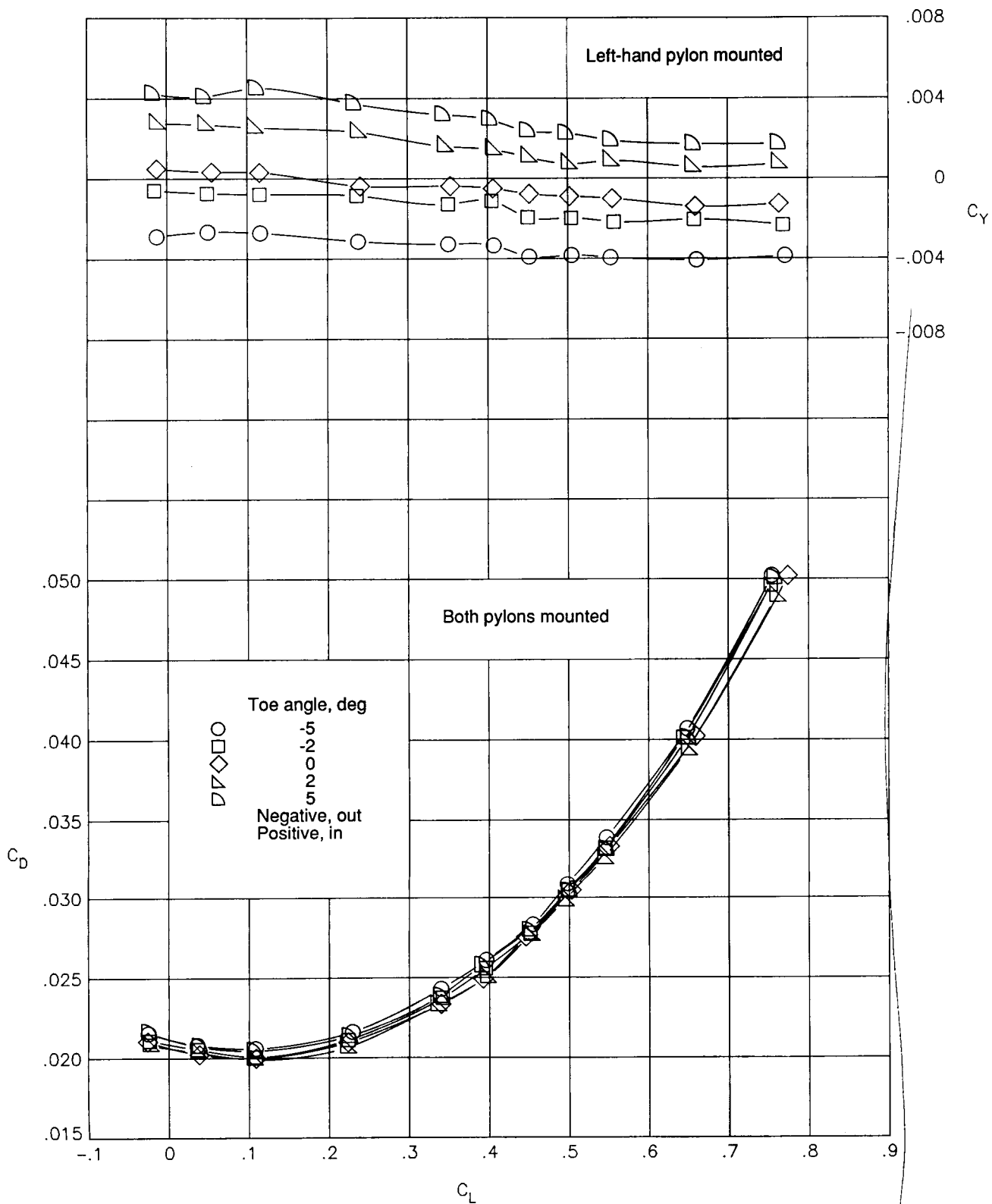
(e) Contoured pylon; $M = 0.7$.

Figure 6. Continued.



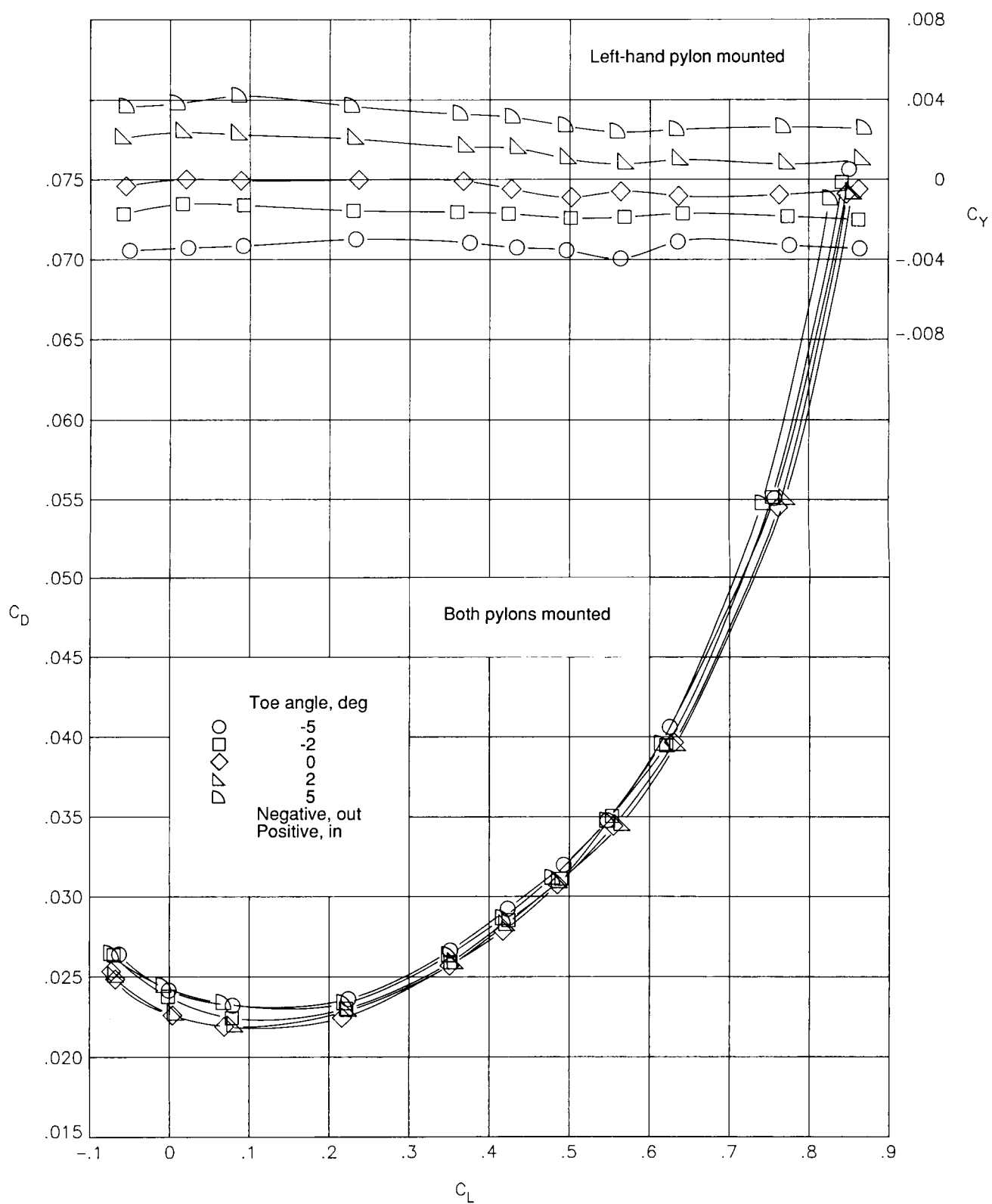
(f) Contoured pylon; $M = 0.8$.

Figure 6. Concluded.



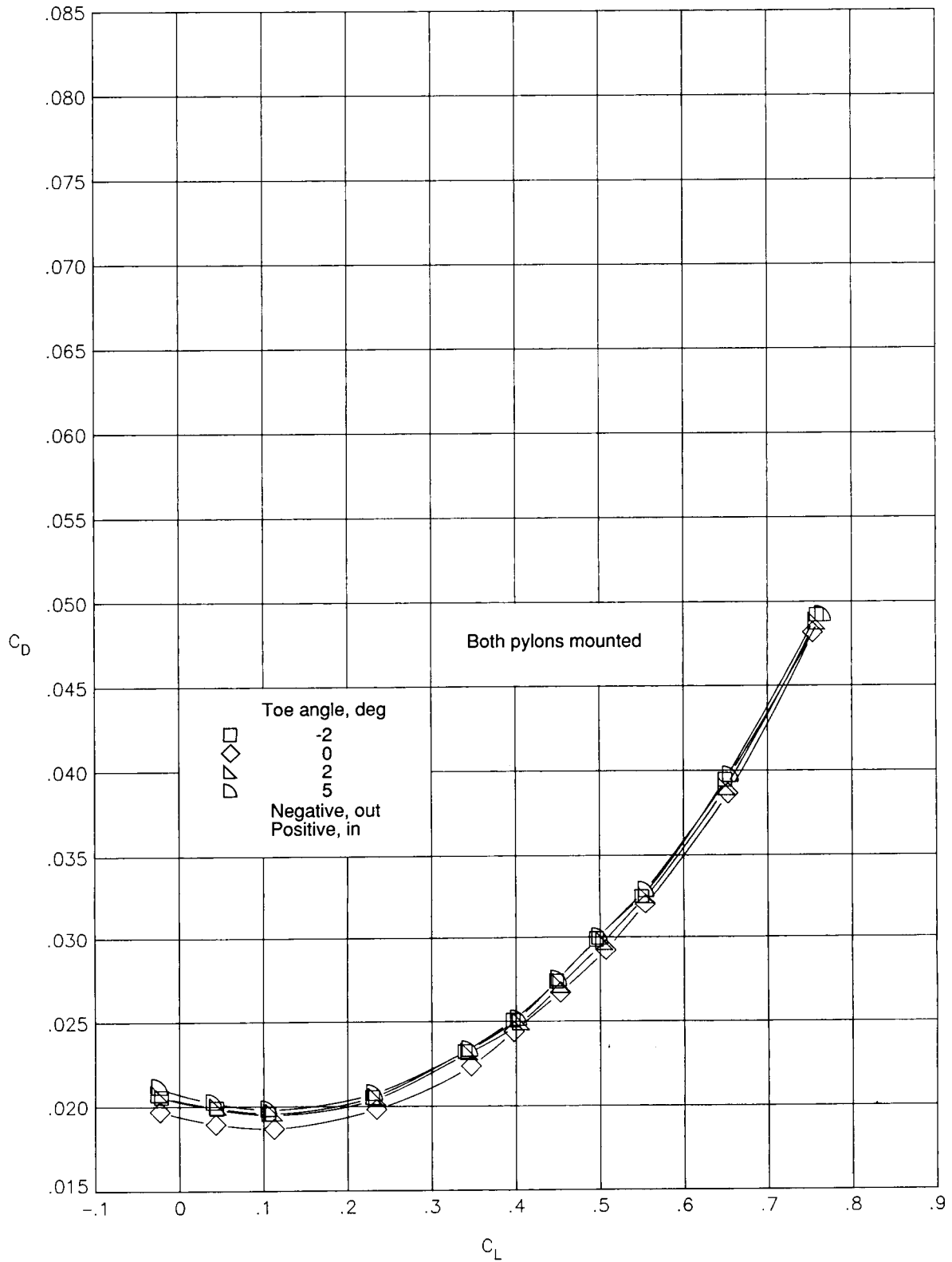
(a) Compression pylon A; $M = 0.7$.

Figure 7. Effect of pylon toe angle on airplane aerodynamic characteristics for compression pylon shapes.



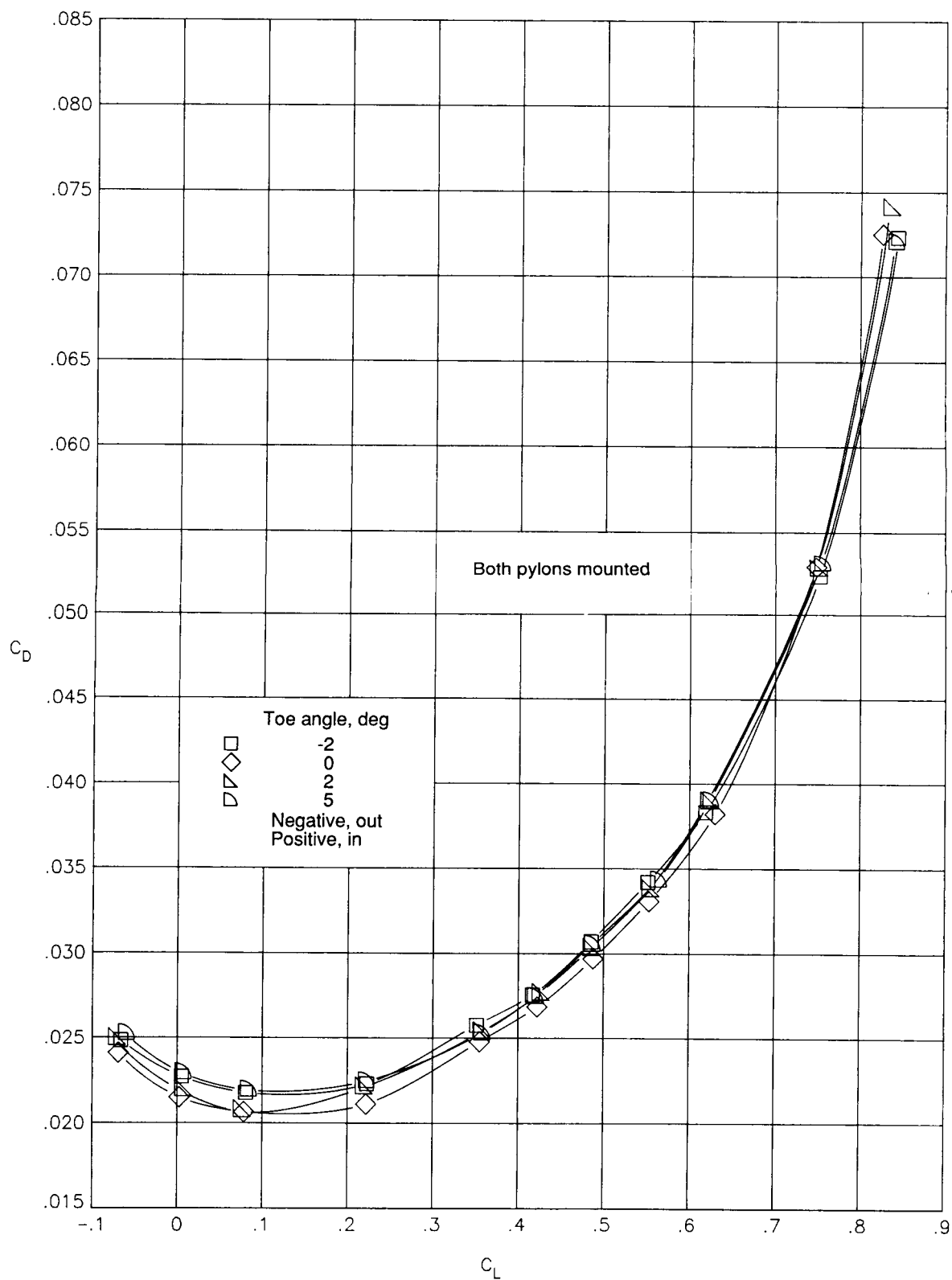
(b) Compression pylon A; $M = 0.8$.

Figure 7. Continued.



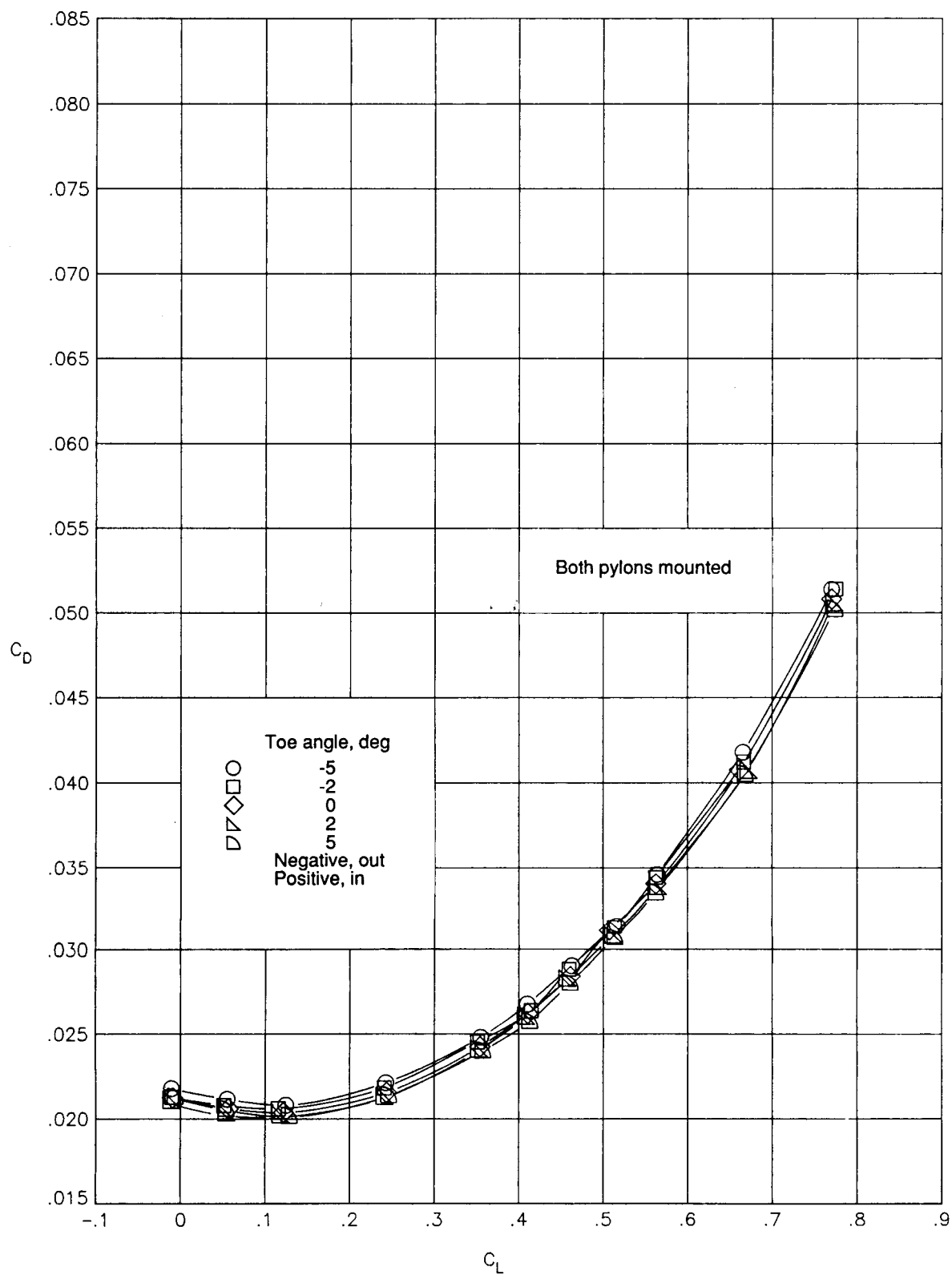
(c) Compression pylon B; $M = 0.7$.

Figure 7. Continued.



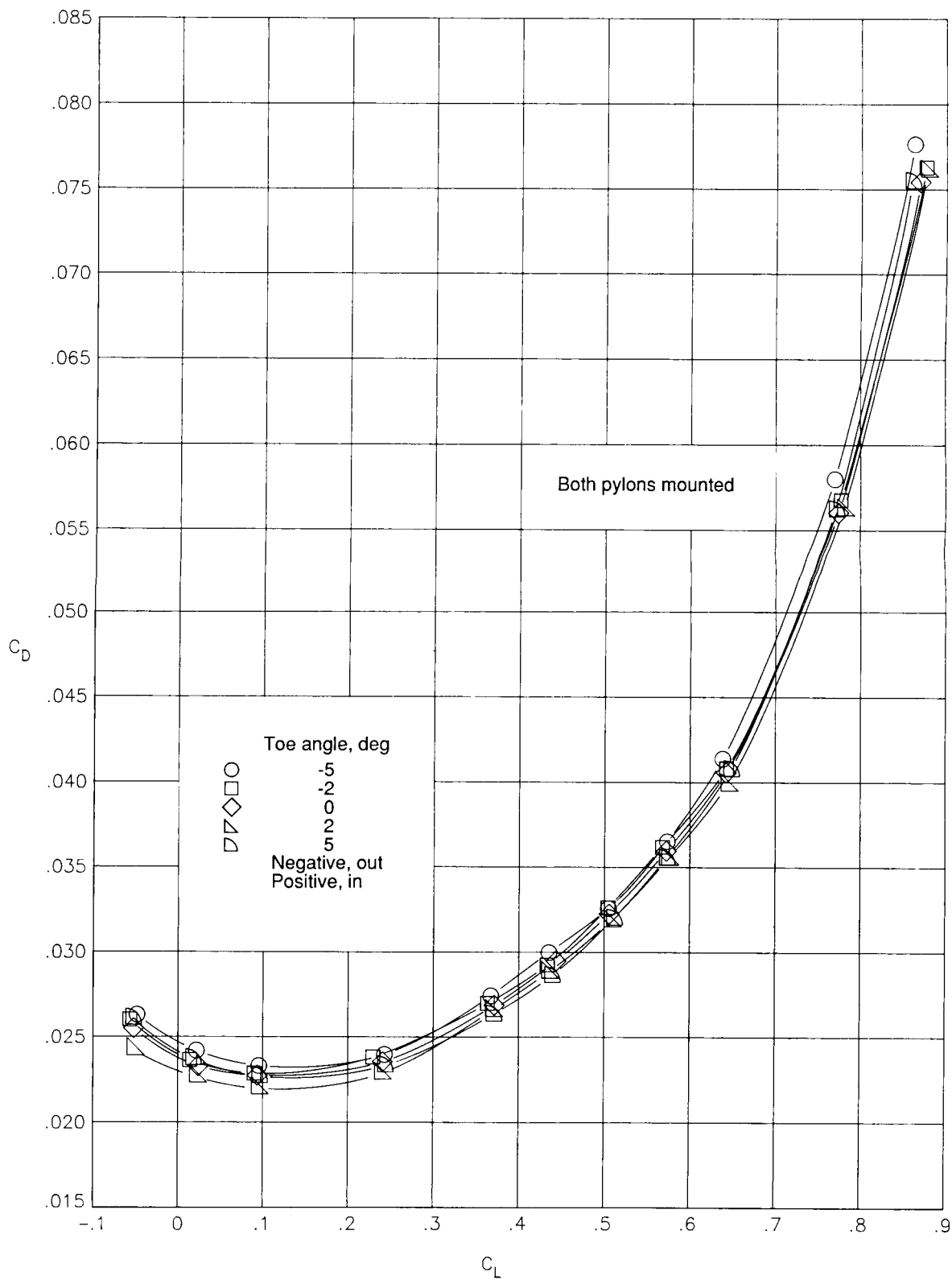
(d) Compression pylon B; $M = 0.8$.

Figure 7. Continued.



(e) Compression pylon C; $M = 0.7$.

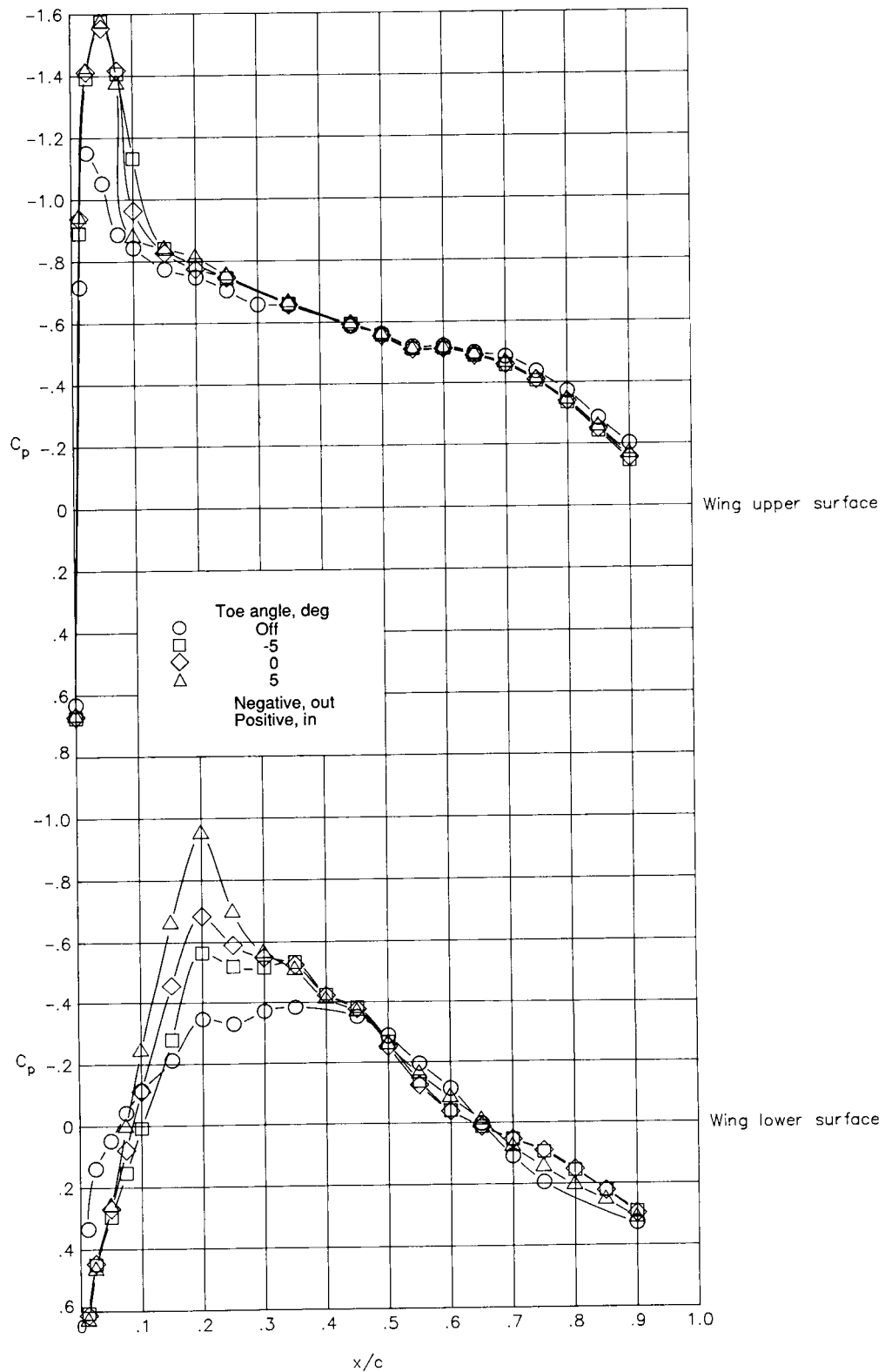
Figure 7. Continued.



(f) Compression pylon C; $M = 0.8$.

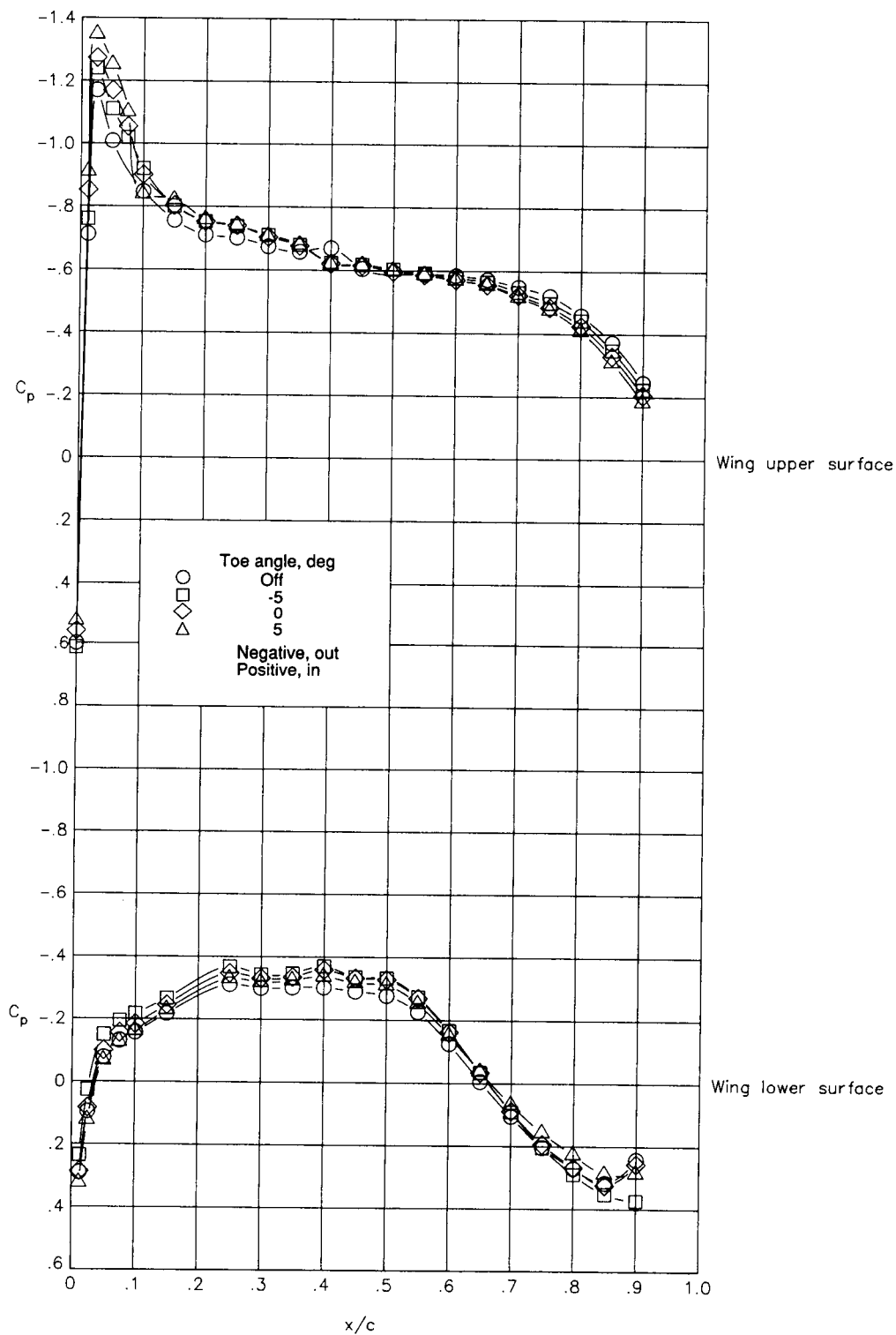
Figure 7. Concluded.

ORIGINAL PAGE IS
OF POOR QUALITY



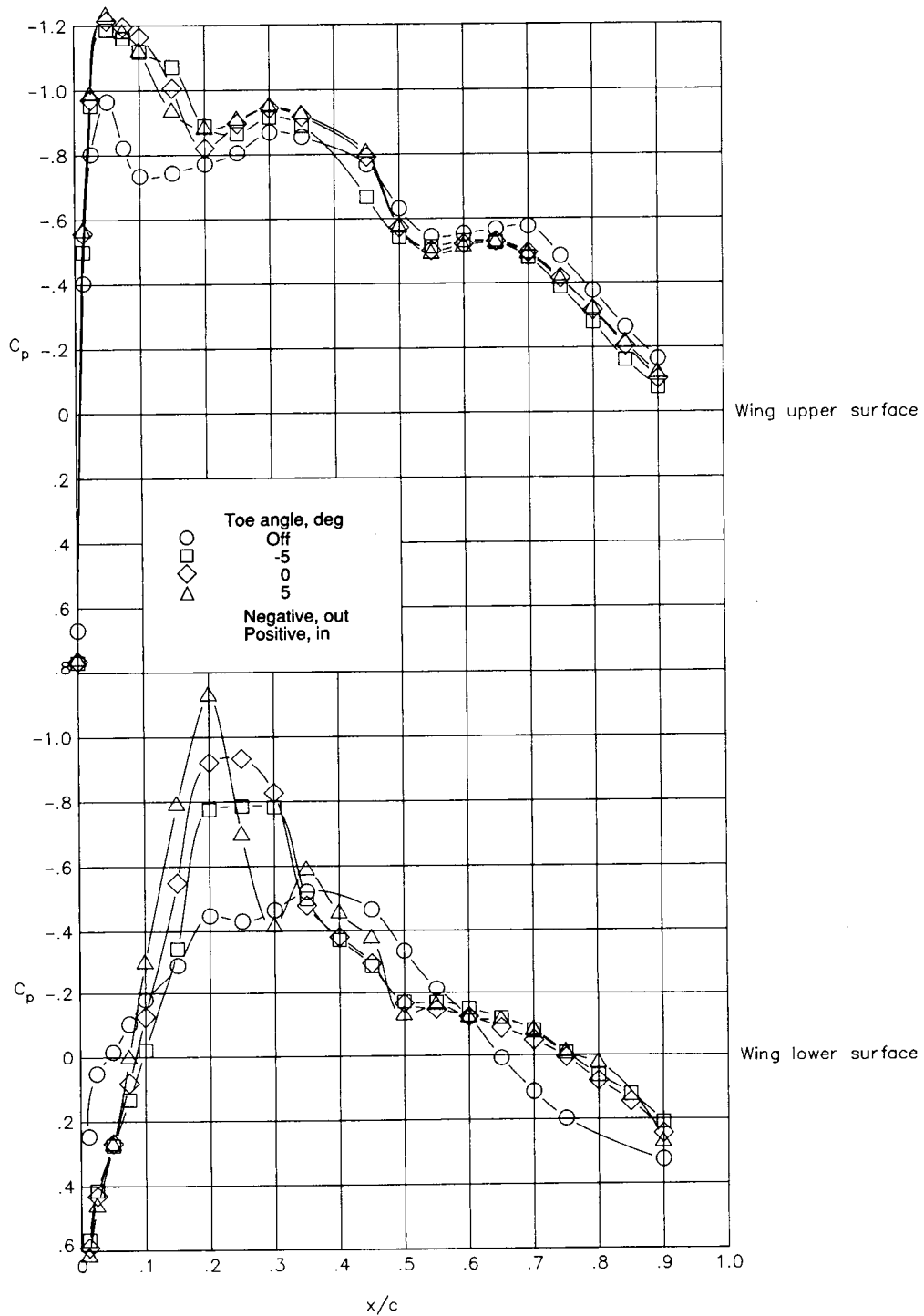
(a) NACA 0012 pylon; $M = 0.7$; inboard row.

Figure 8. Effect of pylon toe angle on wing chordwise pressure distributions for conventional pylon shapes. $C_L \approx 0.5$.



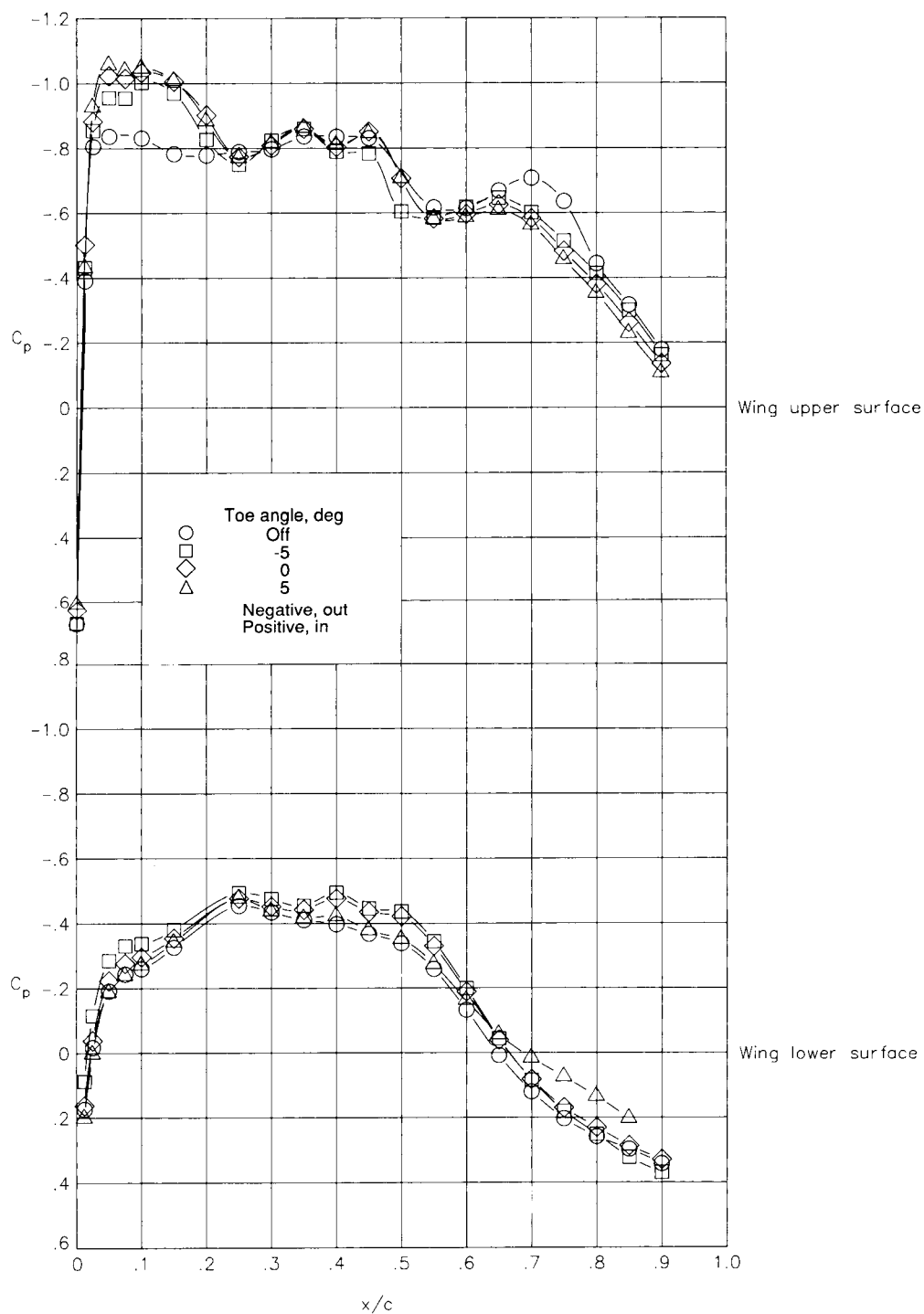
(b) NACA 0012 pylon; $M = 0.7$; outboard row.

Figure 8. Continued.



(c) NACA 0012 pylon; $M = 0.8$; inboard row.

Figure 8. Continued.

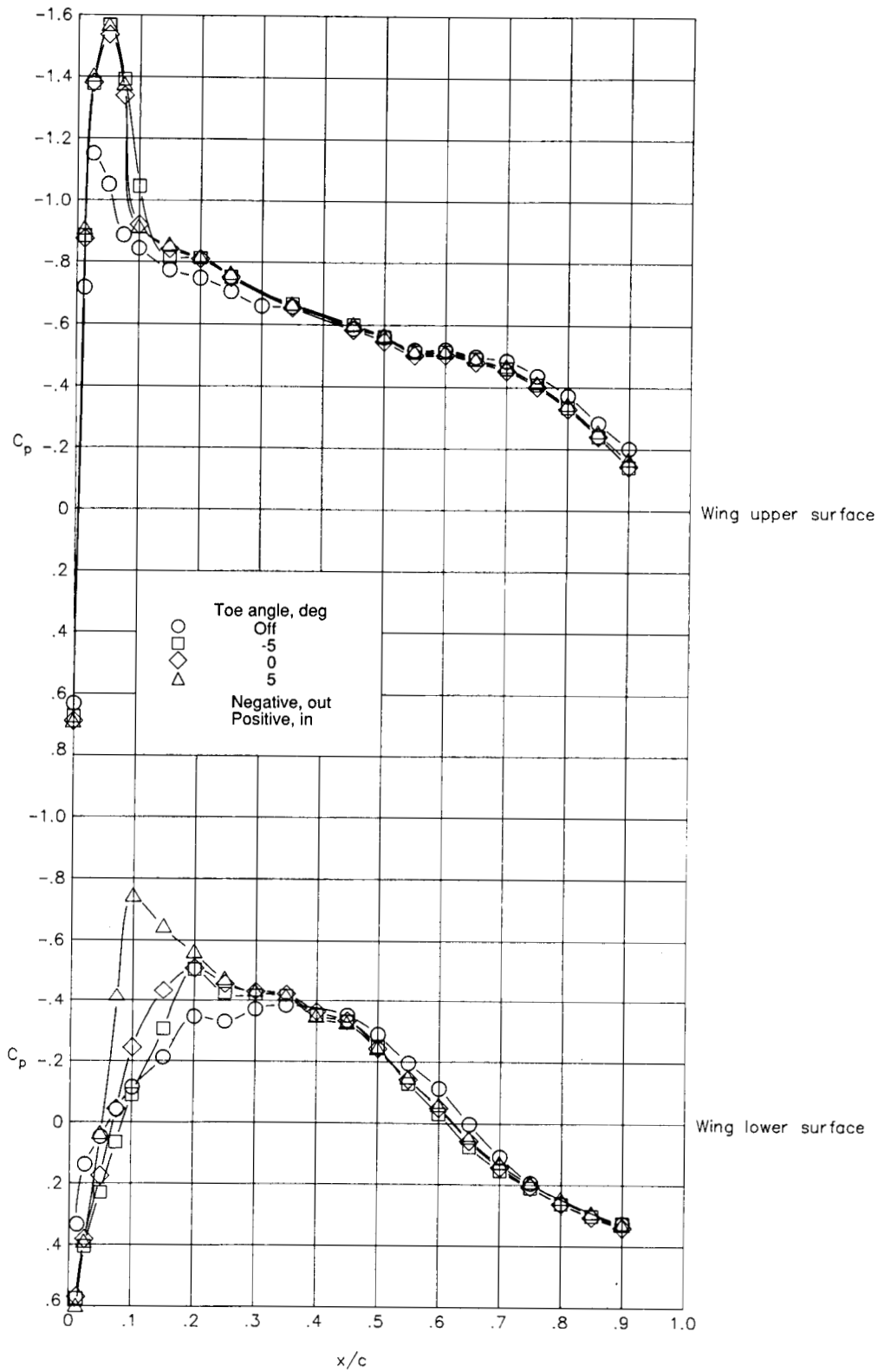


(d) NACA 0012 pylon; $M = 0.8$; outboard row.

Figure 8. Continued.

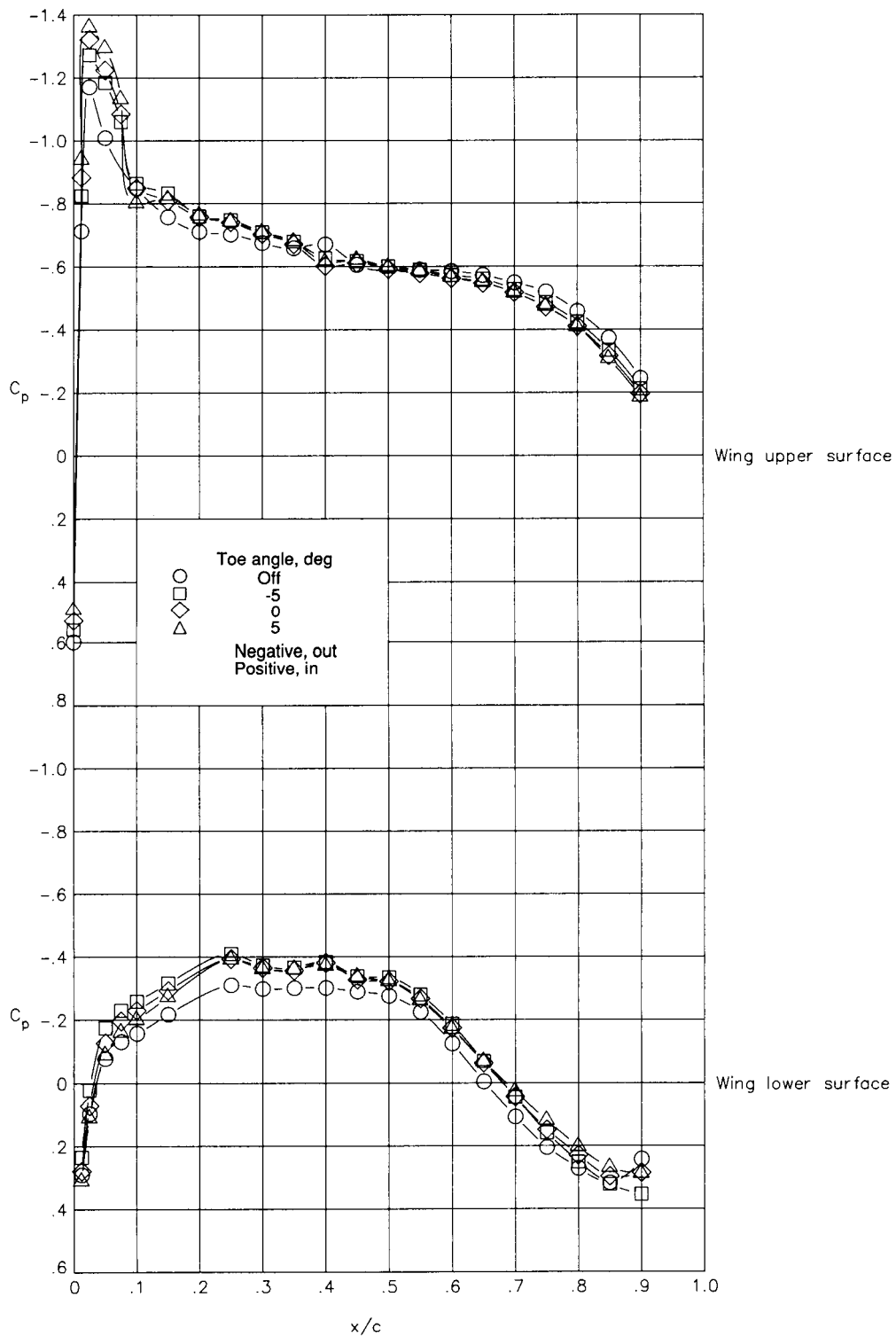
ORIGINAL PAGE IS
OF POOR QUALITY

ORIGINAL PAGE IS
OF POOR QUALITY



(e) NACA 4412 pylon; $M = 0.7$; inboard row.

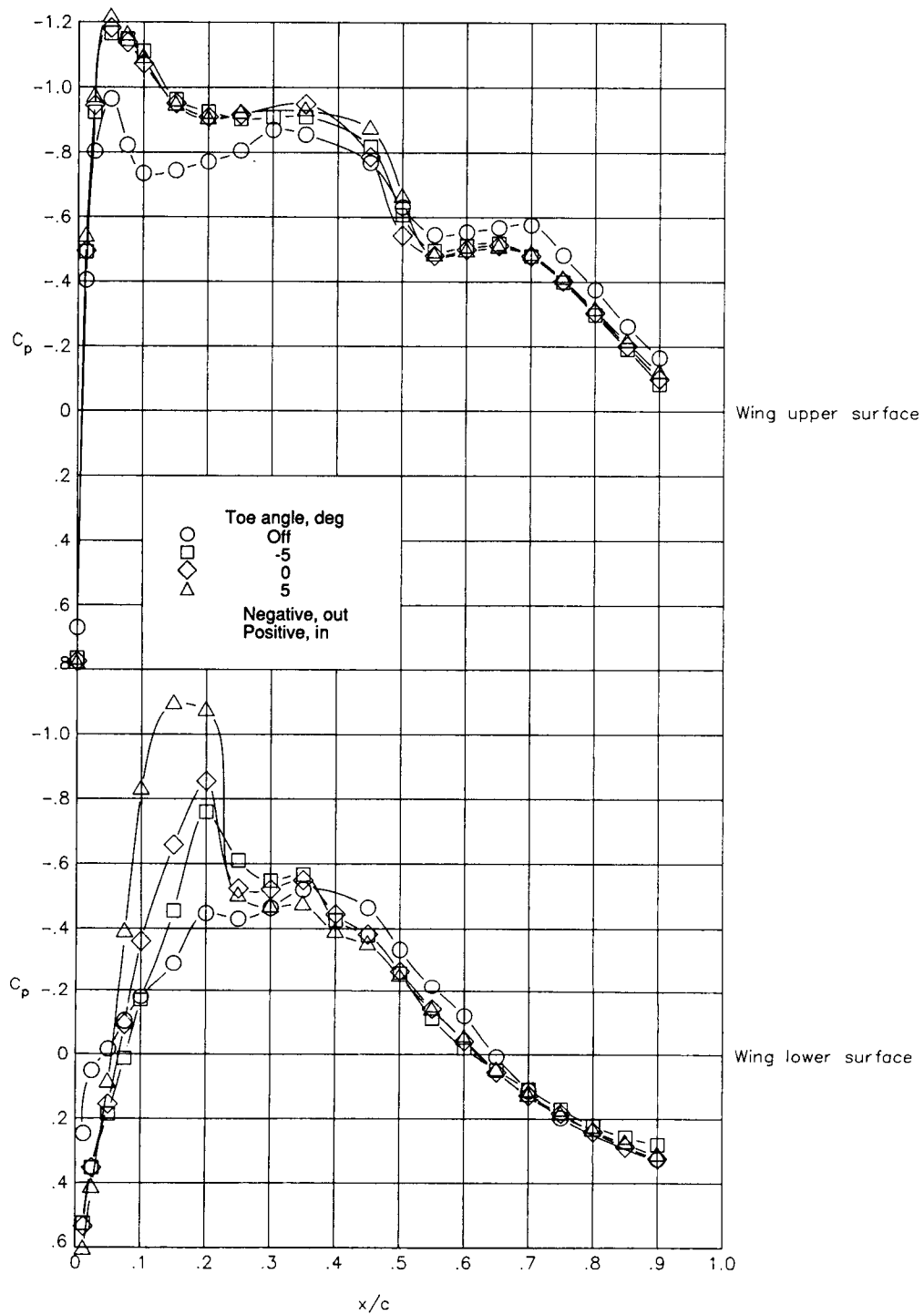
Figure 8. Continued.



(f) NACA 4412 pylon; $M = 0.7$; outboard row.

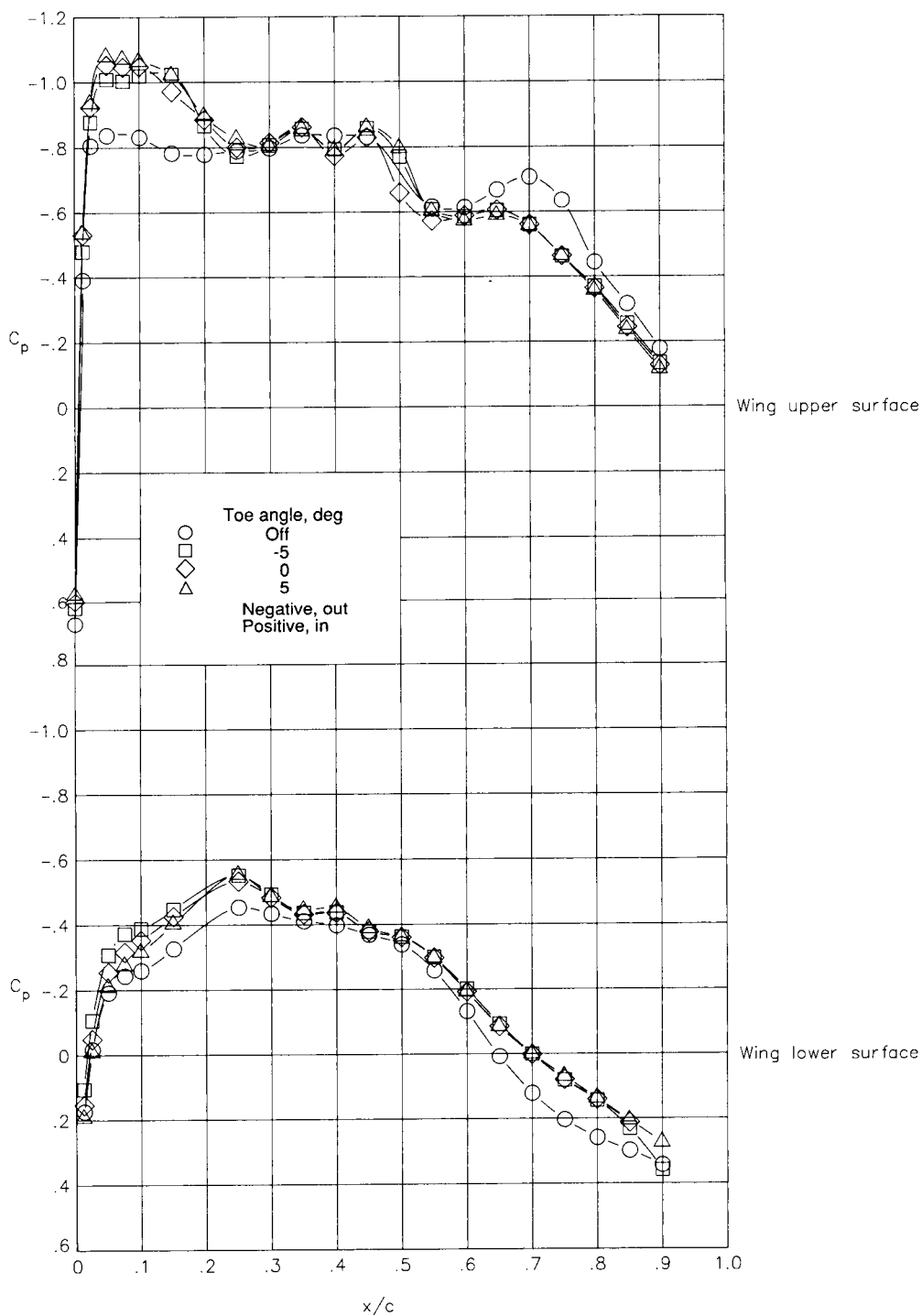
Figure 8. Continued.

ORIGINAL PAGE IS
OF POOR QUALITY



(g) NACA 4412 pylon; $M = 0.8$; inboard row.

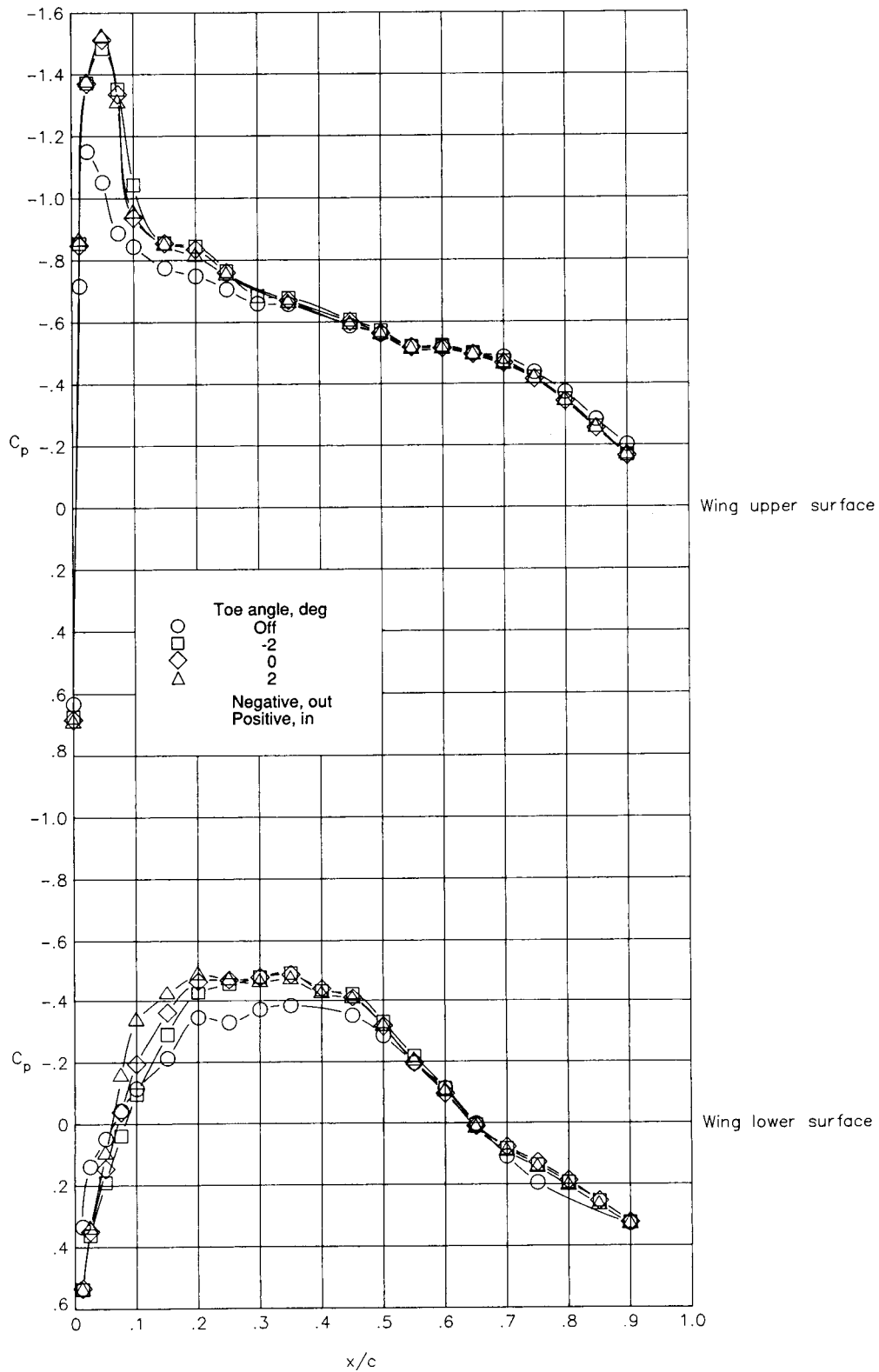
Figure 8. Continued.



(h) NACA 4412 pylon; $M = 0.8$; outboard row.

Figure 8. Continued.

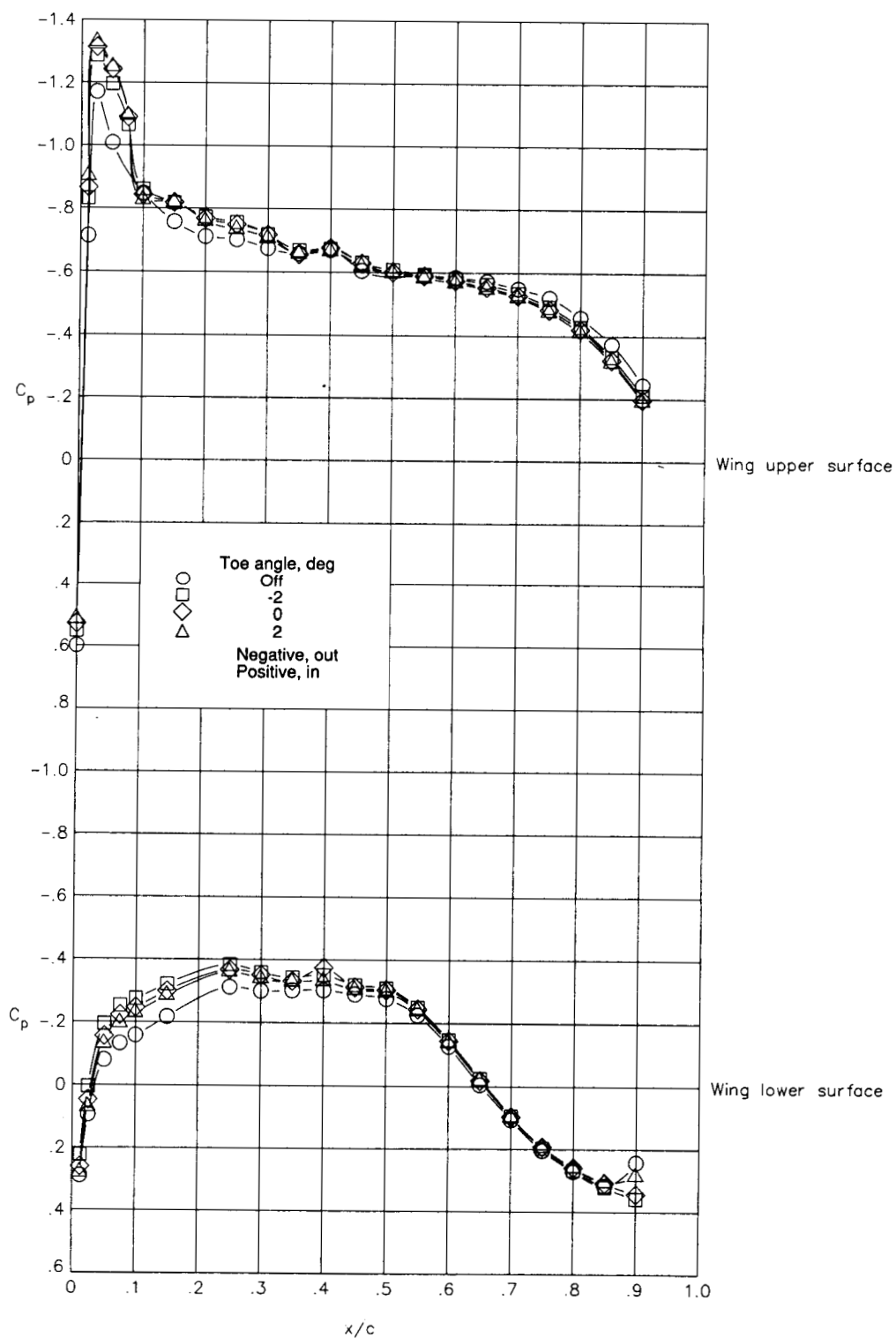
ORIGINAL PAGE IS
OF POOR QUALITY



(i) Contoured pylon; $M = 0.7$; inboard row.

Figure 8. Continued.

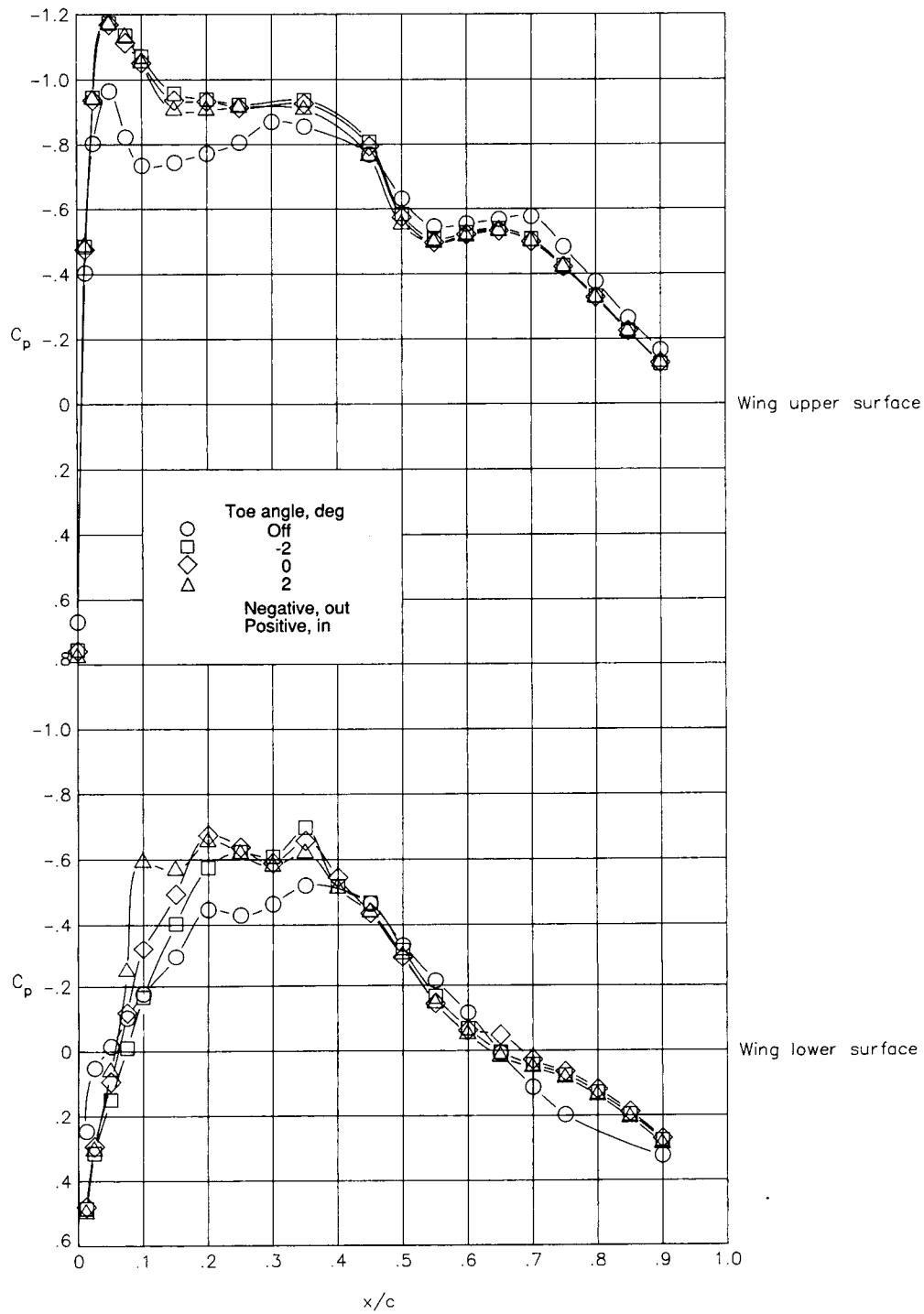
ORIGINAL PAGE IS
OF POOR QUALITY



(j) Contoured pylon; $M = 0.7$; outboard row.

Figure 8. Continued.

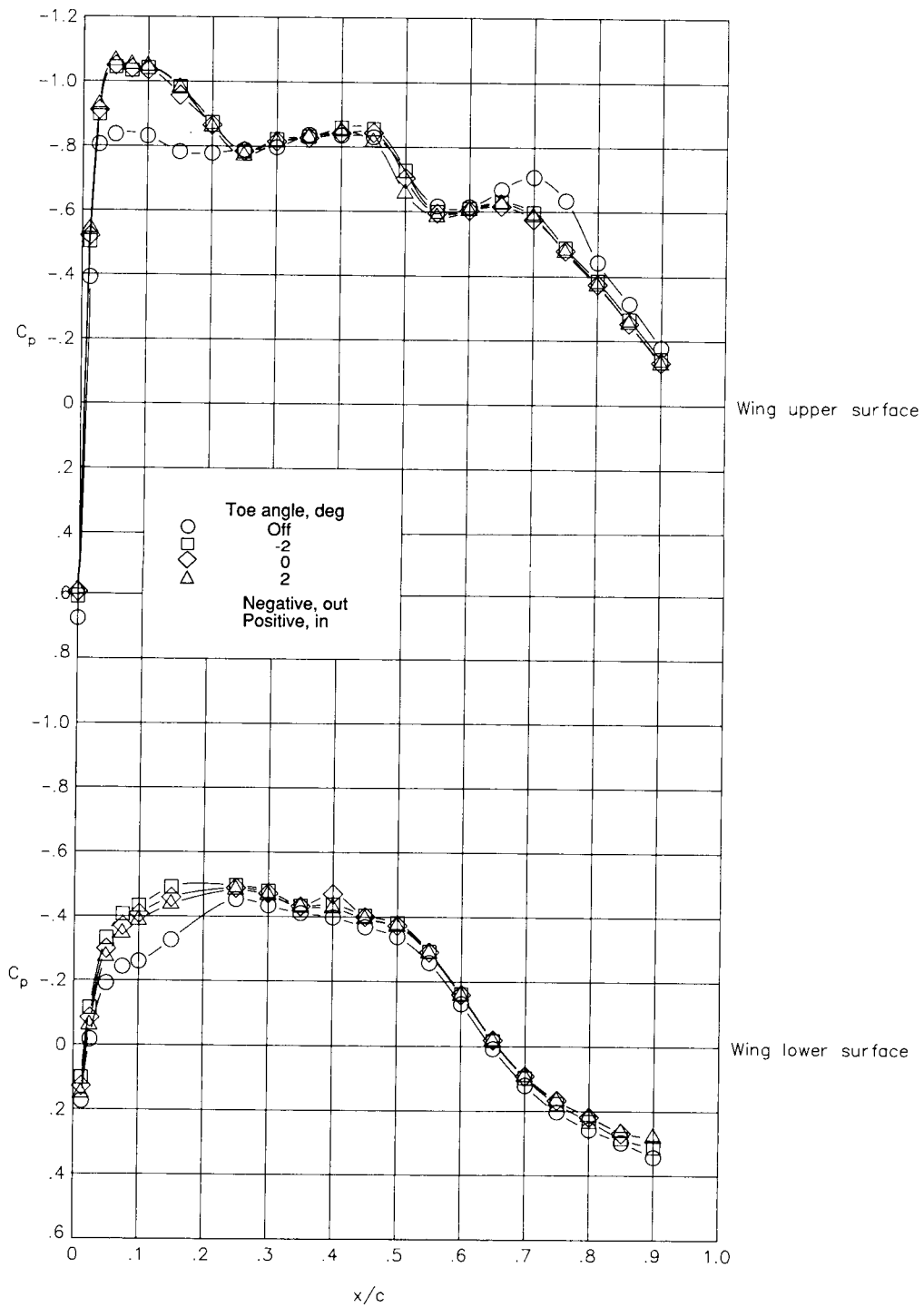
ORIGINAL PAGE IS
OF POOR QUALITY



(k) Contoured pylon; $M = 0.8$; inboard row.

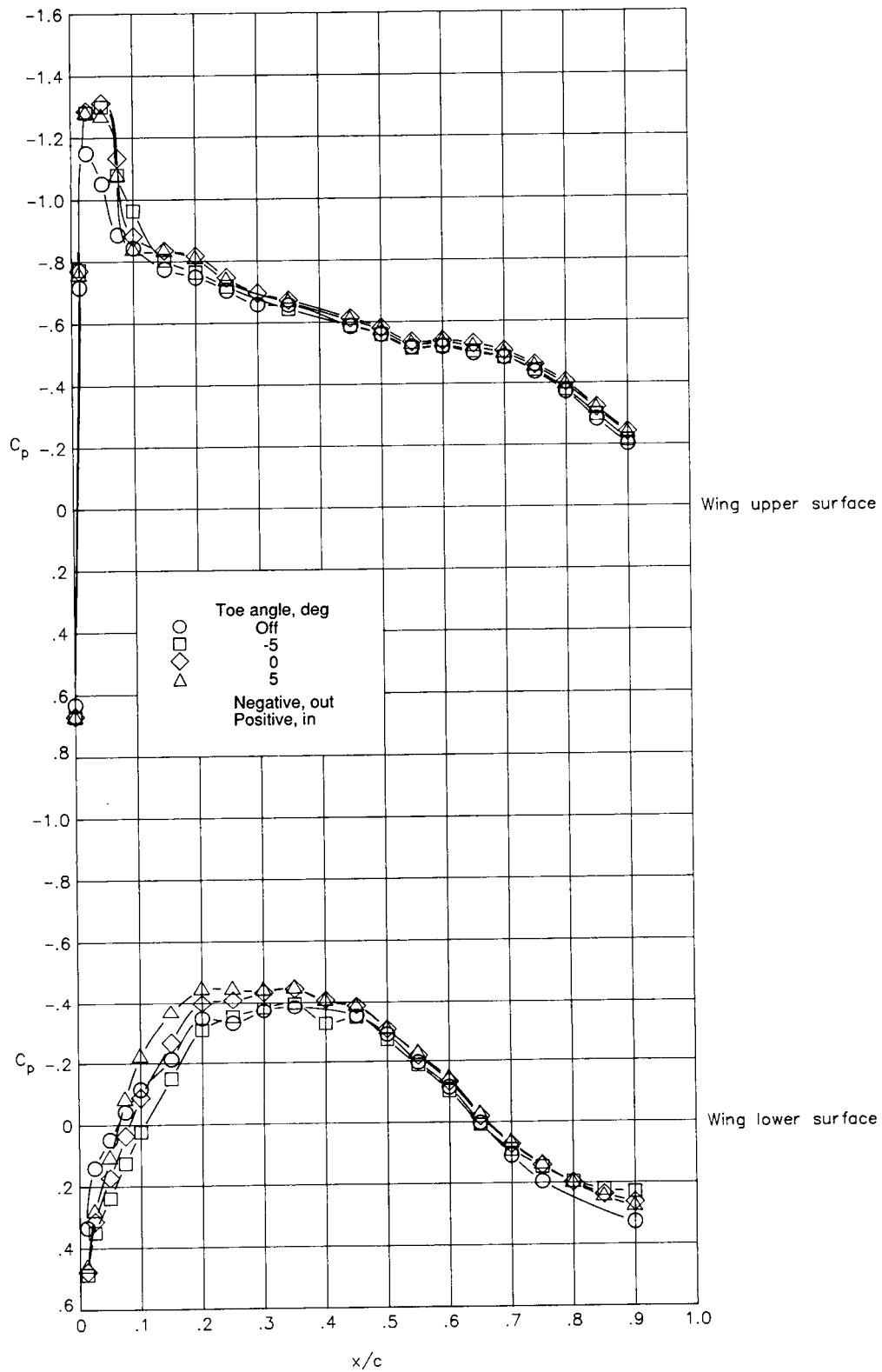
Figure 8. Continued.

ORIGINAL PAGE IS
OF POOR QUALITY



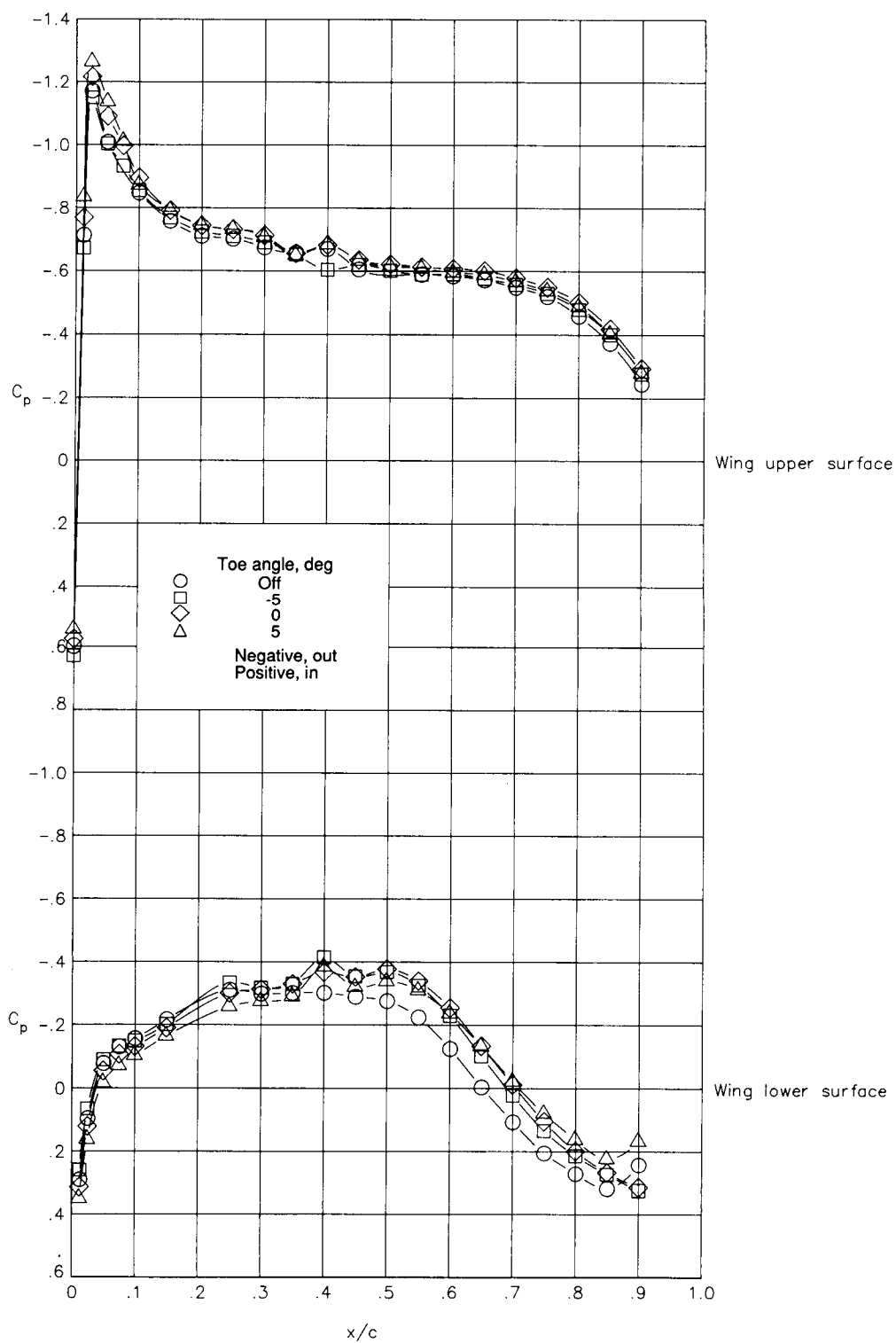
(1) Contoured pylon; $M = 0.80$; outboard row.

Figure 8. Concluded.



(a) Compression pylon A; $M = 0.7$; inboard row.

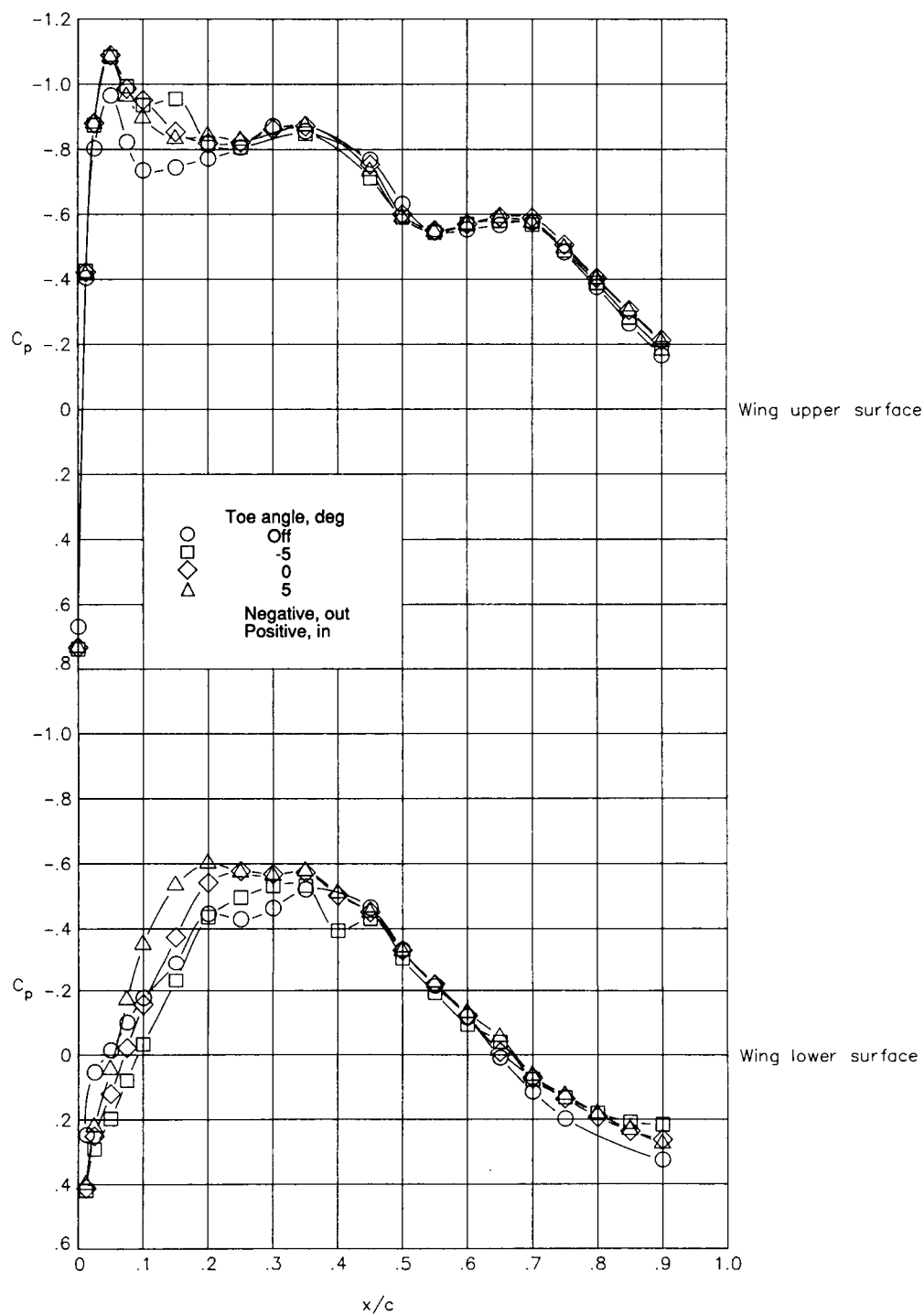
Figure 9. Effect of pylon toe angle on wing chordwise pressure distributions for compression pylon shapes. $C_L \approx 0.5$.



(b) Compression pylon A; $M = 0.7$; outboard row.

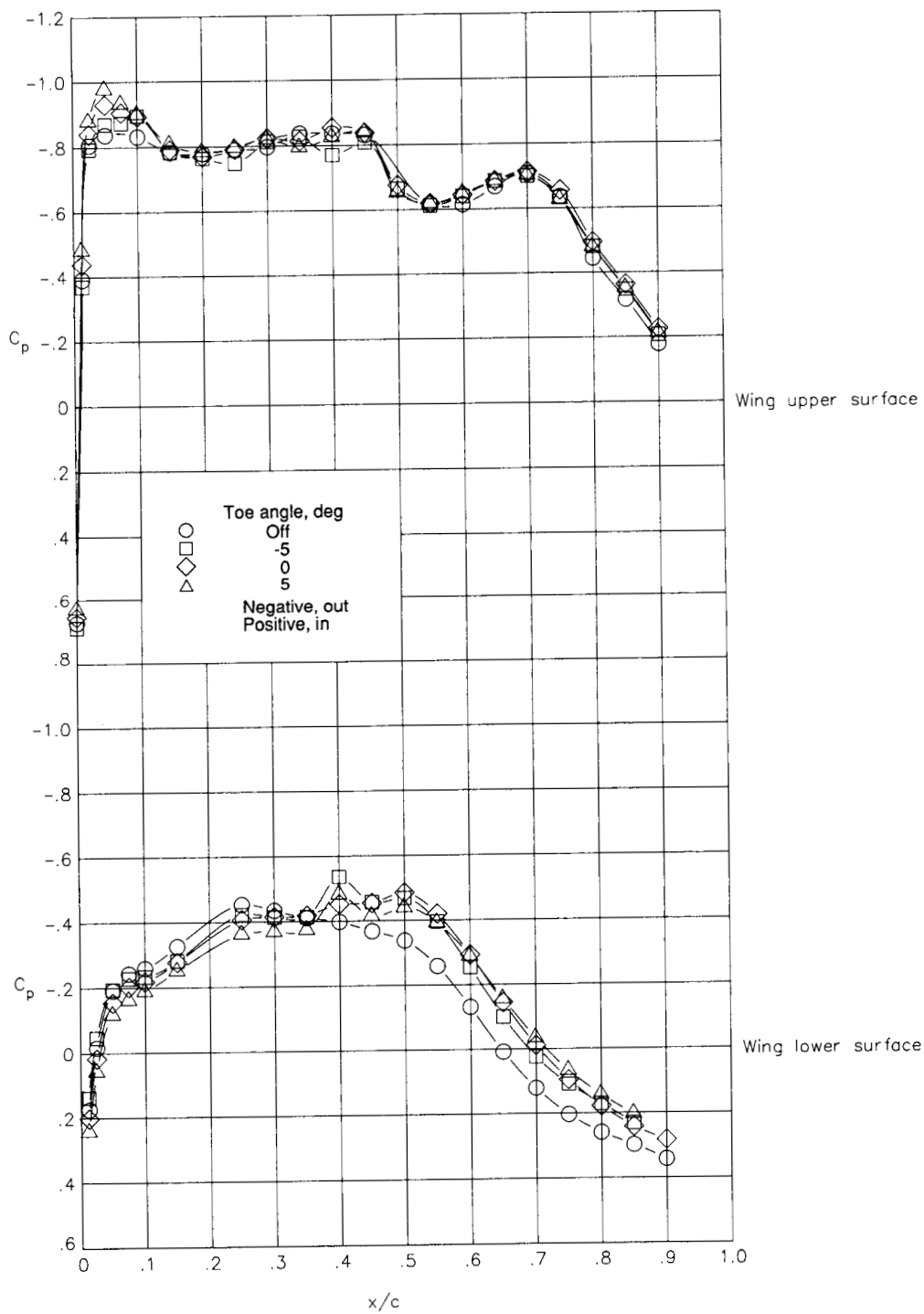
Figure 9. Continued.

ORIGINAL PAGE IS
OF POOR QUALITY



(c) Compression pylon A; $M = 0.8$; inboard row.

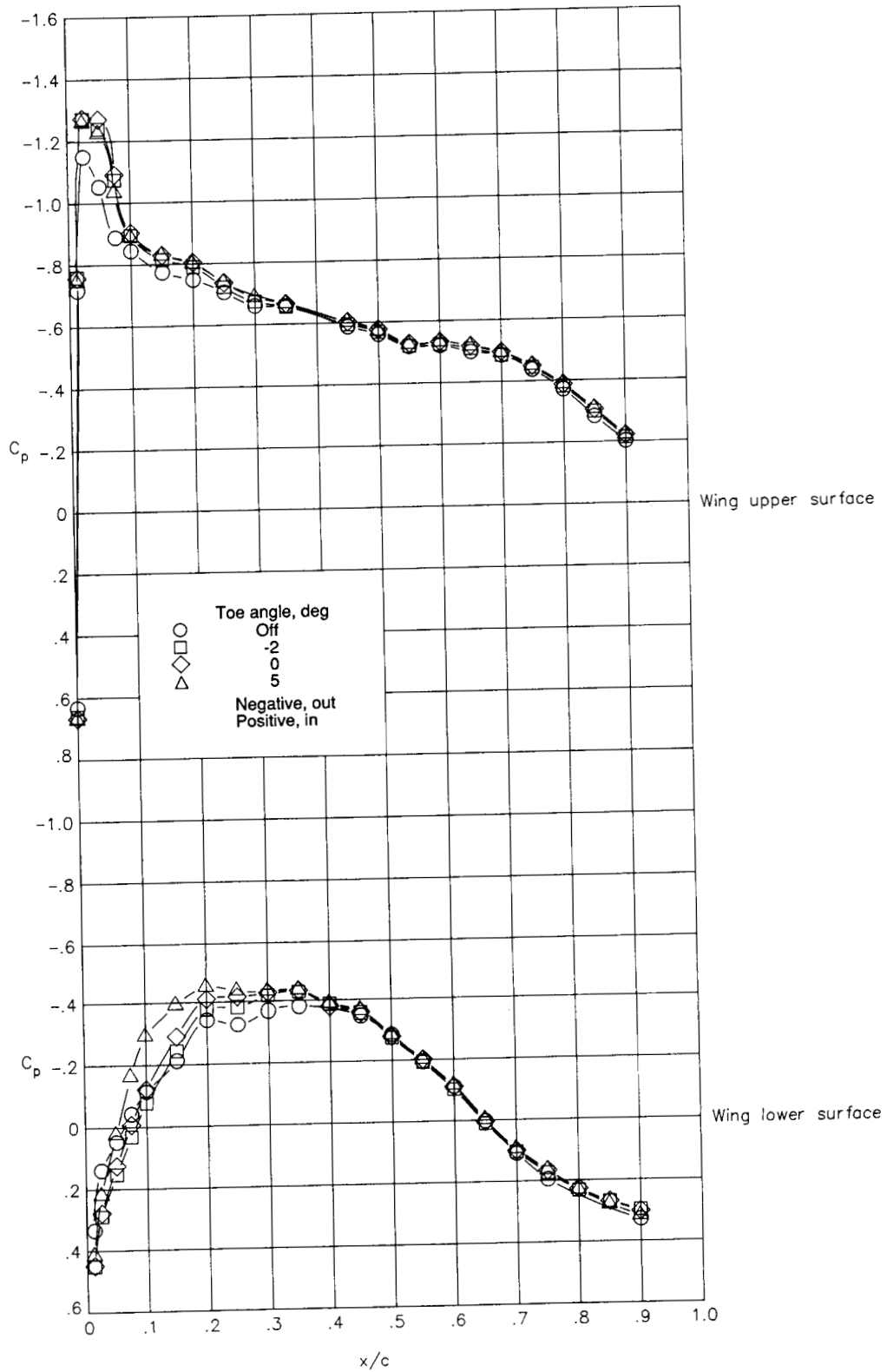
Figure 9. Continued.



(d) Compression pylon A; $M = 0.8$; outboard row.

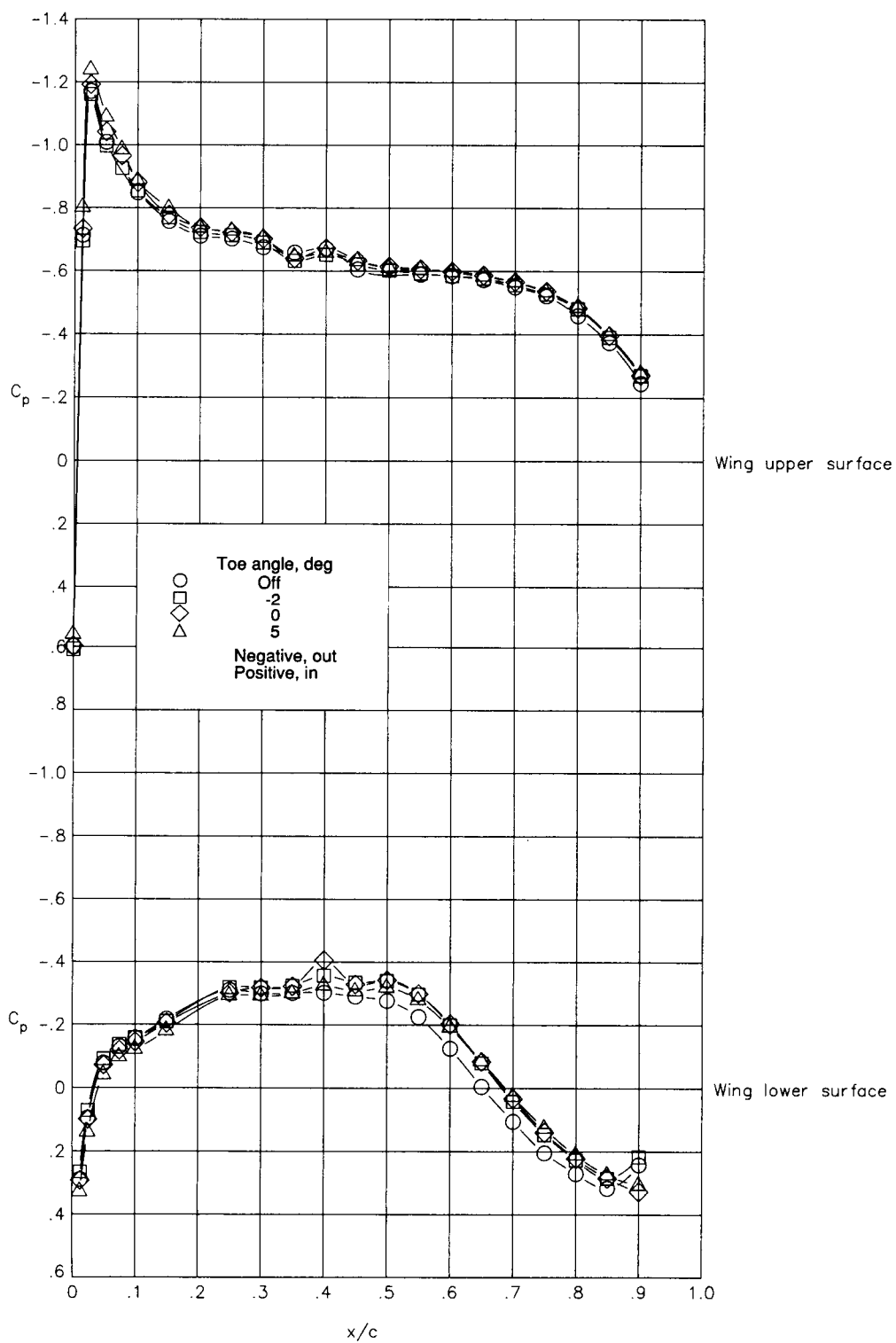
Figure 9. Continued.

ORIGINAL PAGE IS
OF POOR QUALITY



(e) Compression pylon B; $M = 0.7$; inboard row.

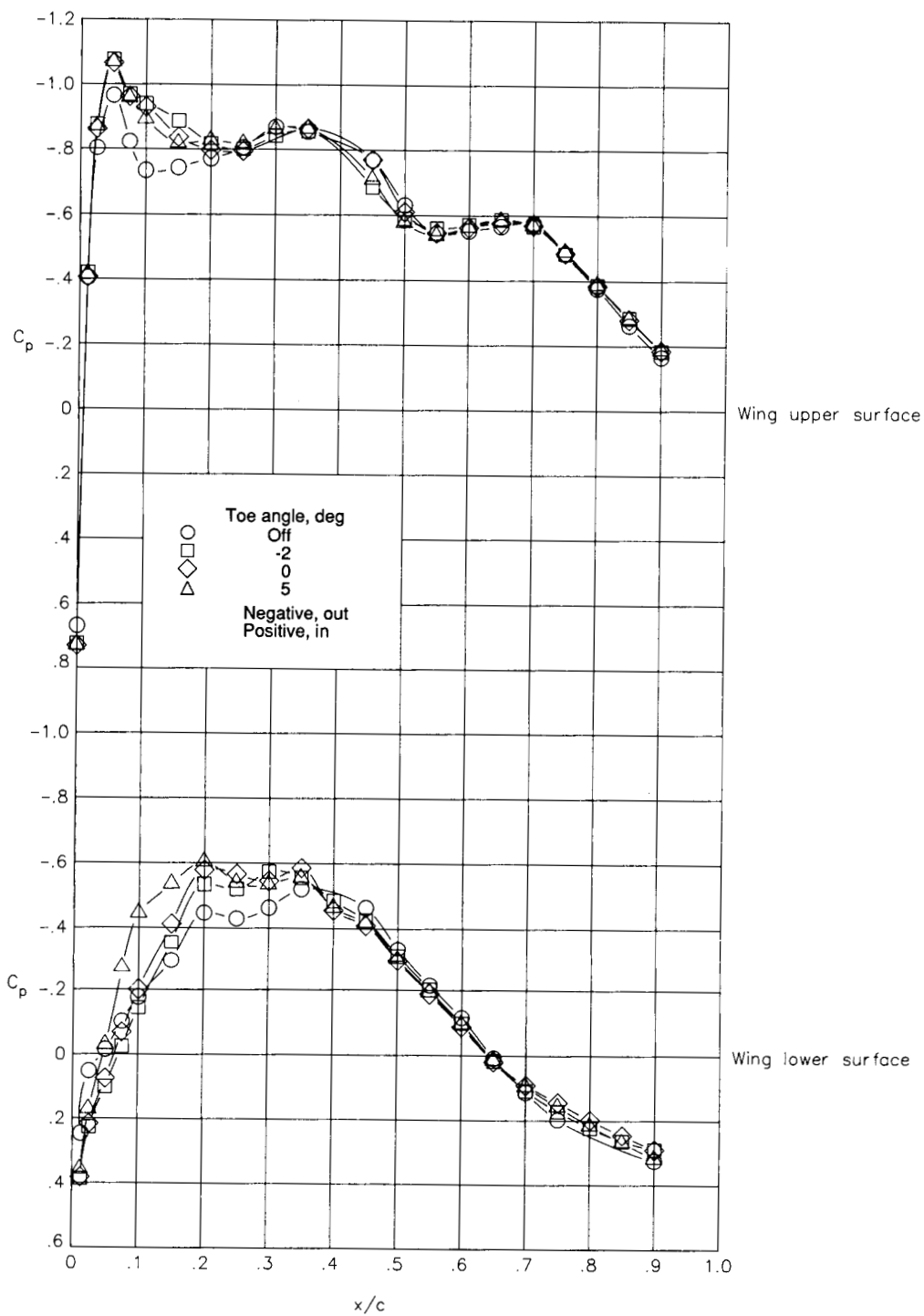
Figure 9. Continued.



(f) Compression pylon B; $M = 0.7$; outboard row.

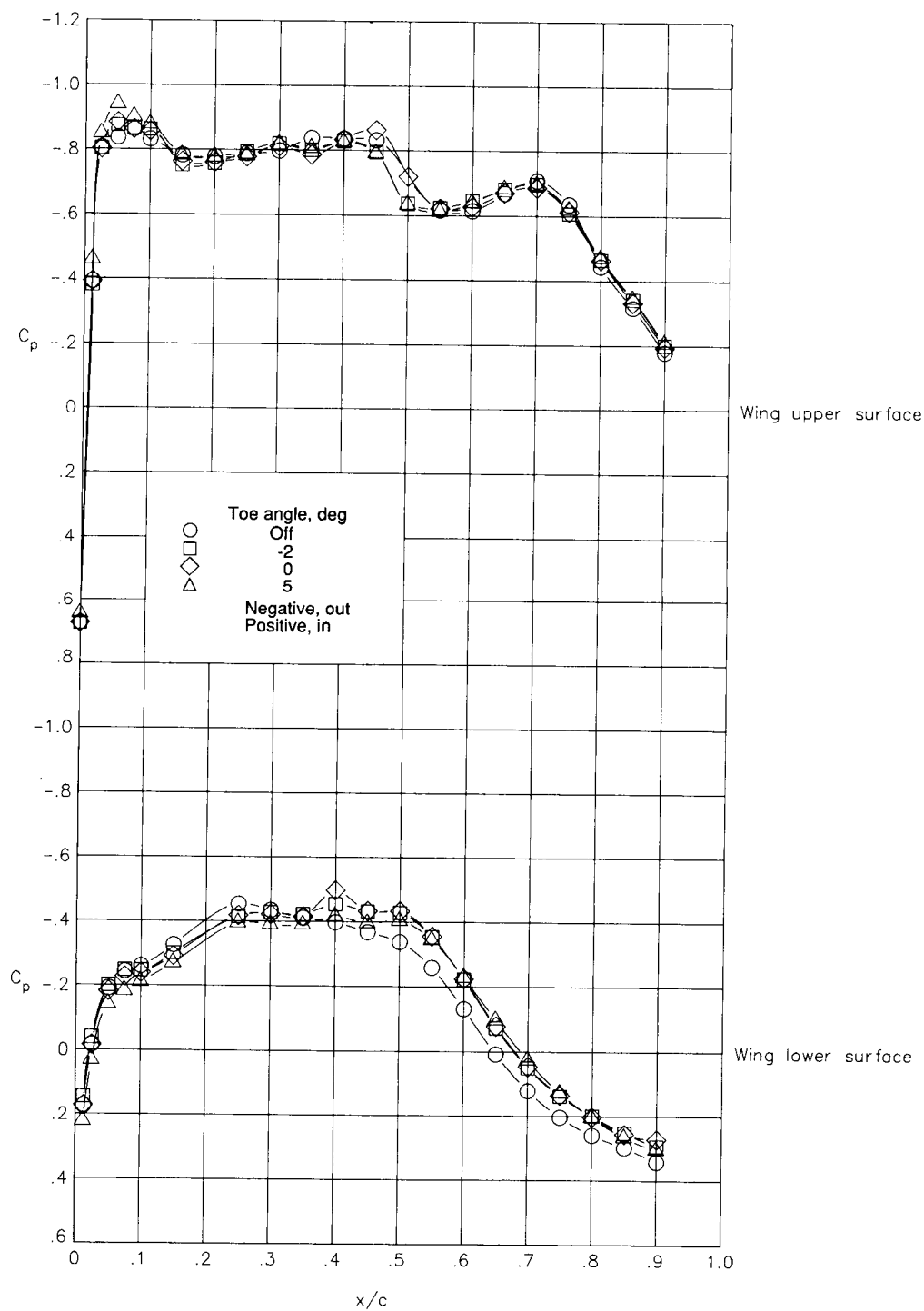
Figure 9. Continued.

ORIGINAL PAGE IS
OF POOR QUALITY



(g) Compression pylon B; $M = 0.8$; inboard row.

Figure 9. Continued.

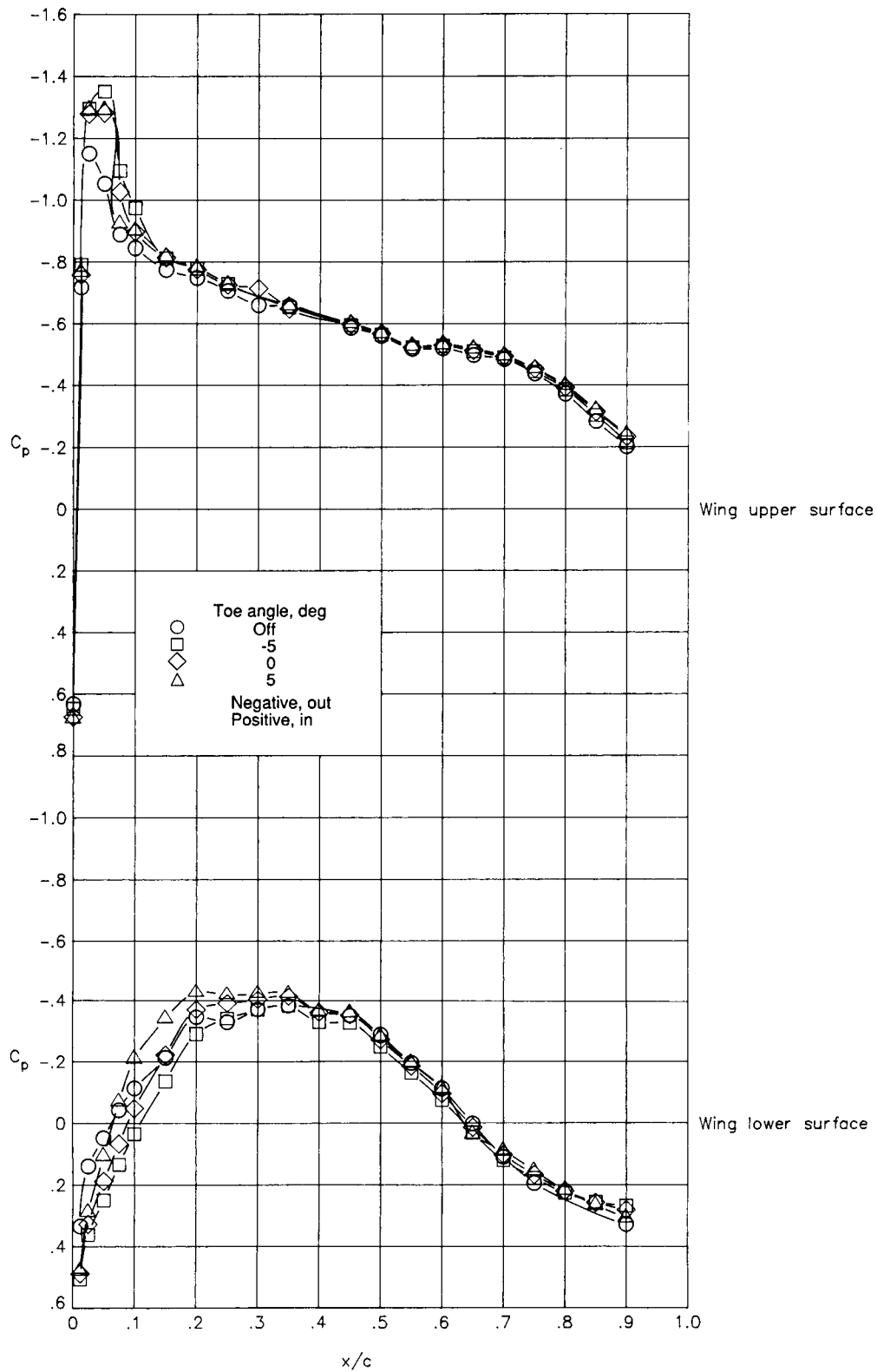


(h) Compression pylon B; $M = 0.8$; outboard row.

Figure 9. Continued.

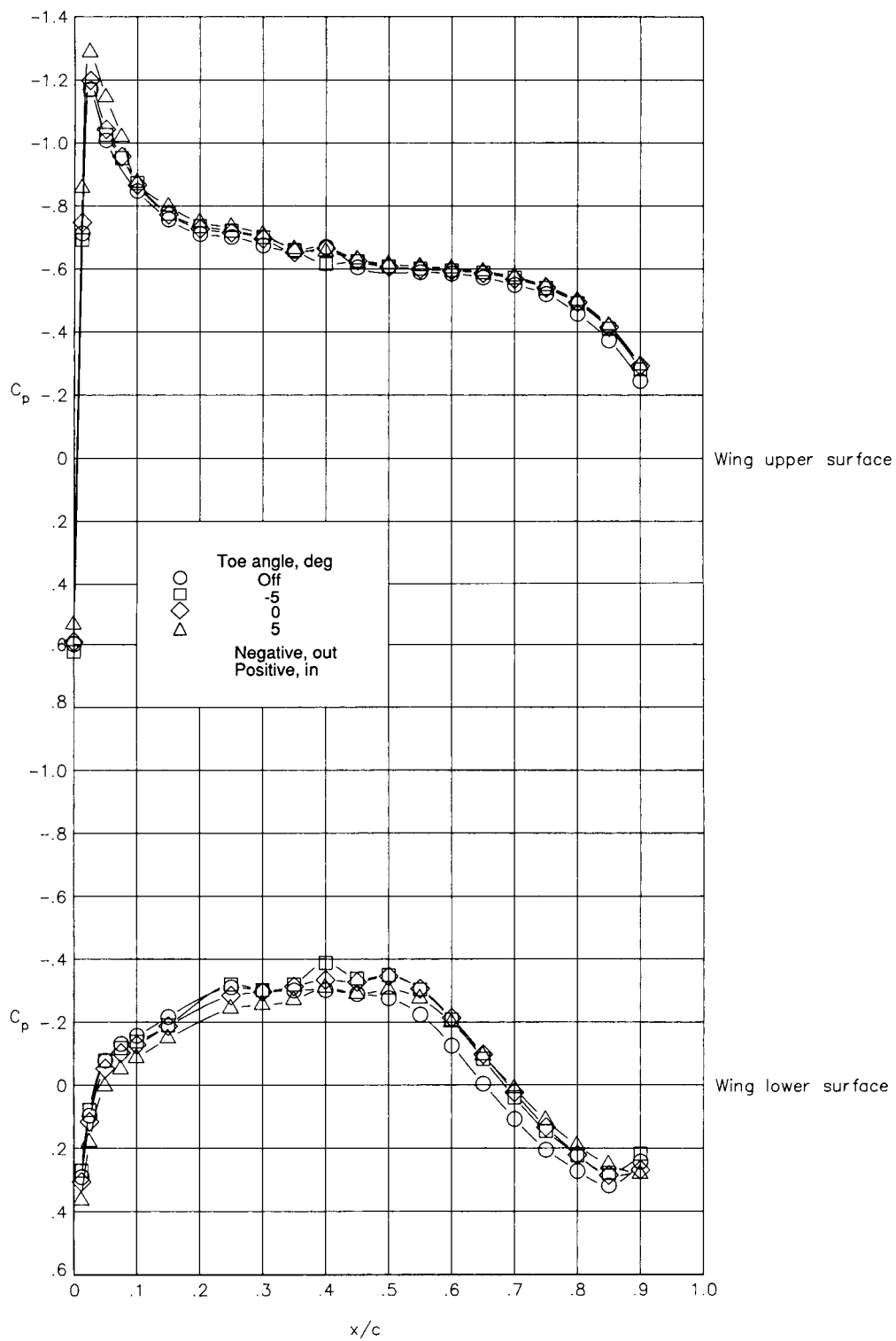
ORIGINAL PAGE IS
OF POOR QUALITY

ORIGINAL PAGE IS
OF POOR QUALITY



(i) Compression pylon C; $M = 0.7$; inboard row.

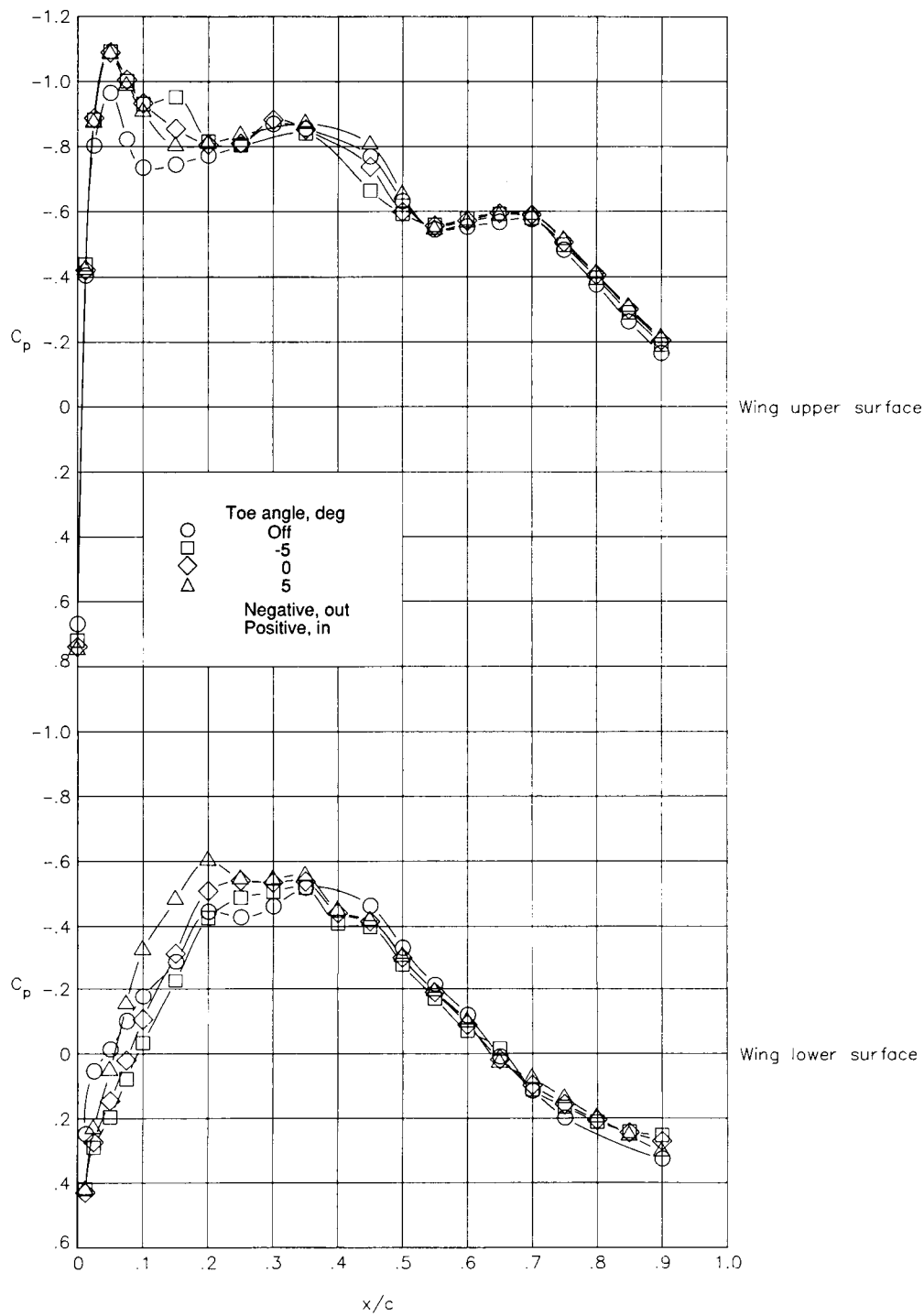
Figure 9. Continued.



(j) Compression pylon C; $M = 0.7$; outboard row.

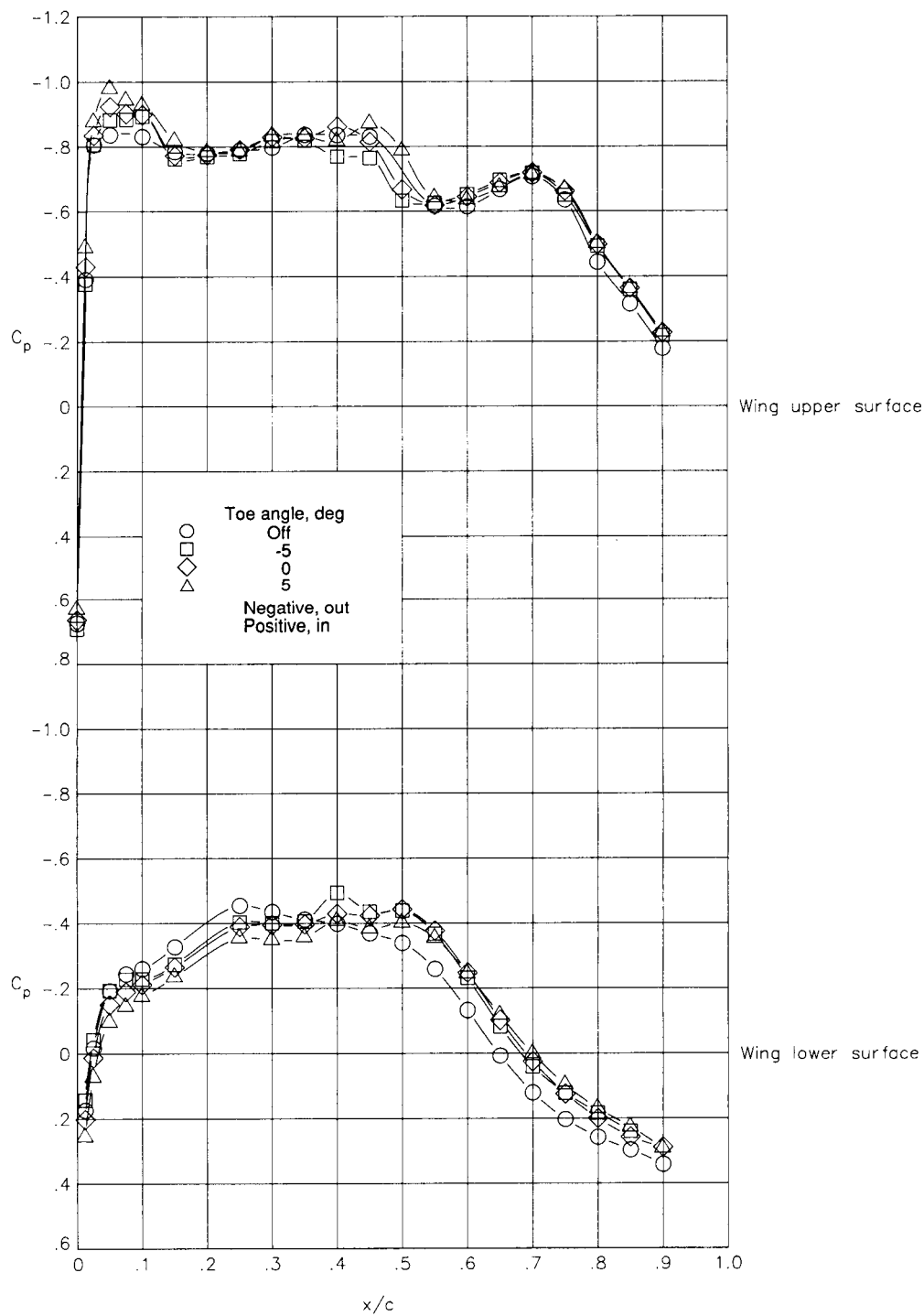
Figure 9. Continued.

ORIGINAL PAGE IS
OF POOR QUALITY



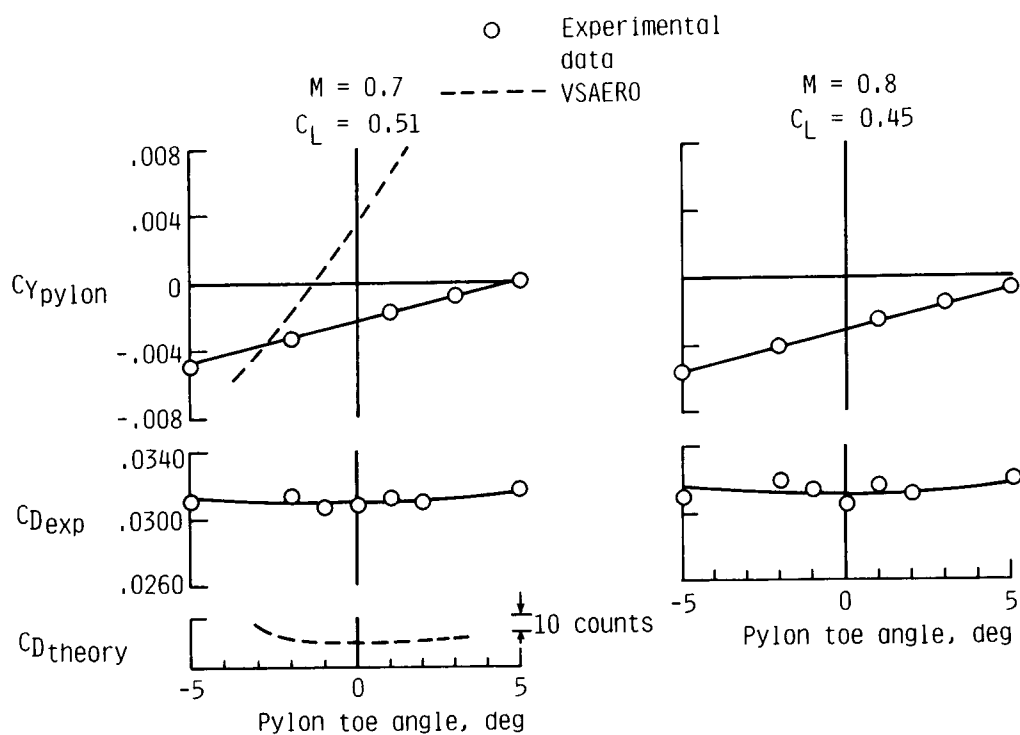
(k) Compression pylon C; $M = 0.8$; inboard row.

Figure 9. Continued.



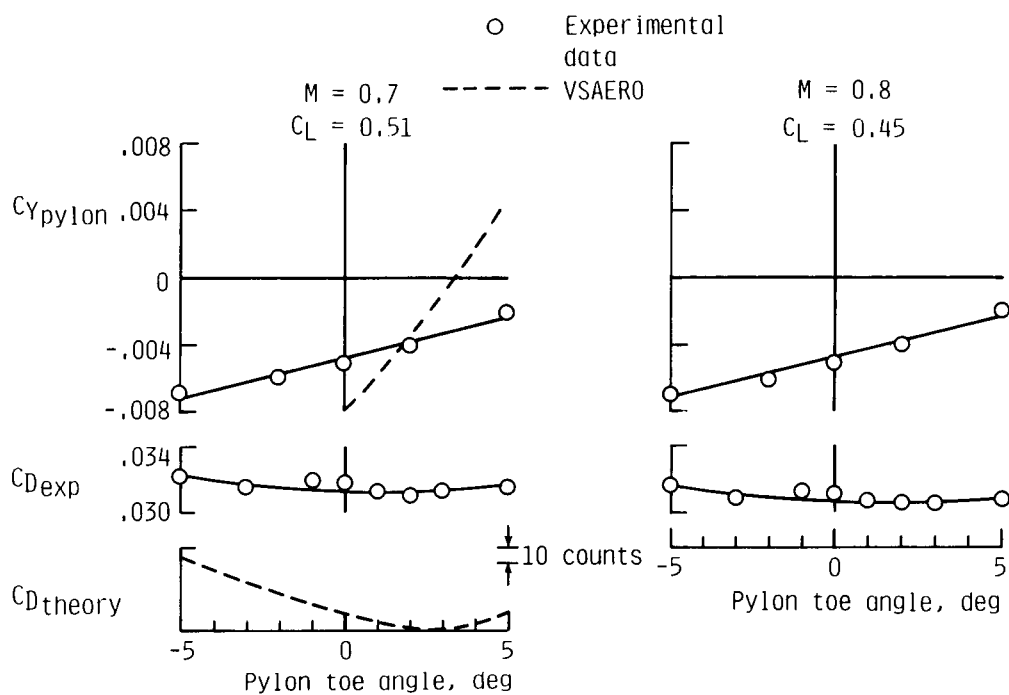
(1) Compression pylon C; $M = 0.8$; outboard row.

Figure 9. Concluded.

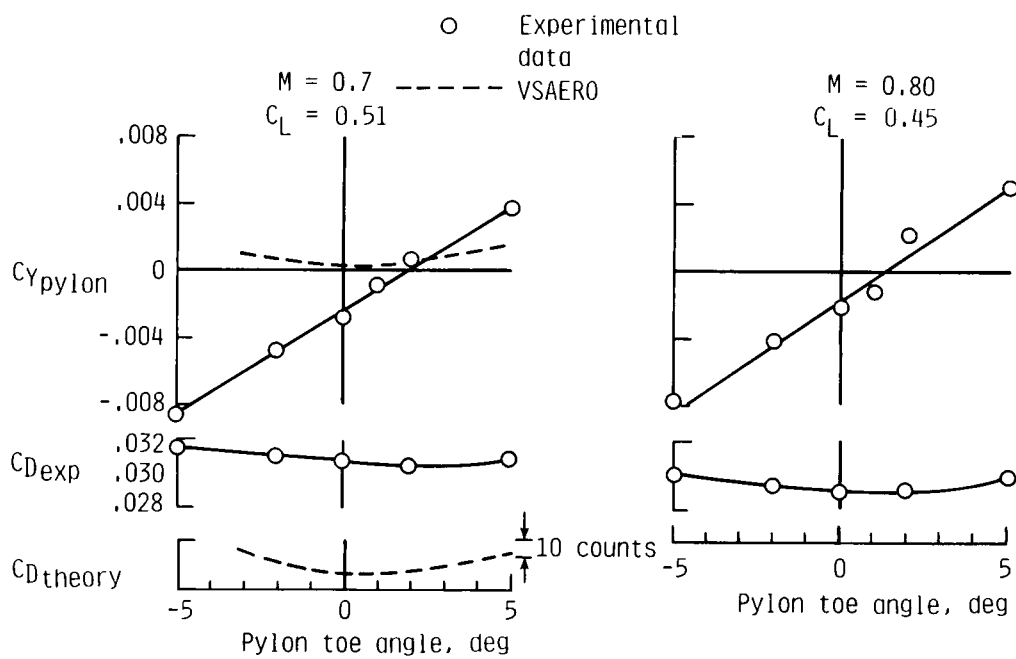


(a) NACA 0012 pylon.

Figure 10. Effect of pylon toe angle on selected aerodynamic characteristics at constant total airplane lift coefficient.



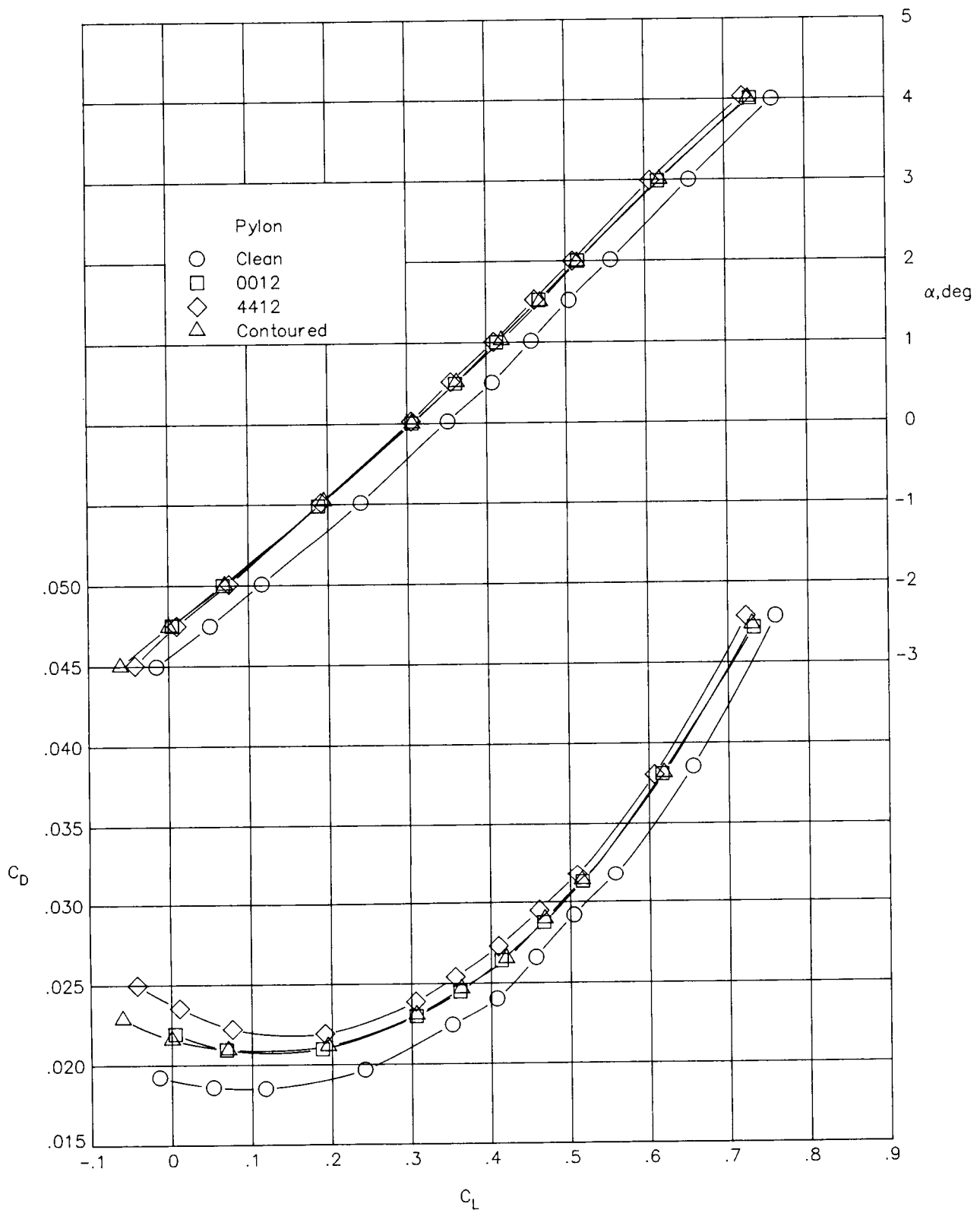
(b) NACA 4412 pylon.



(c) Compression pylon A.

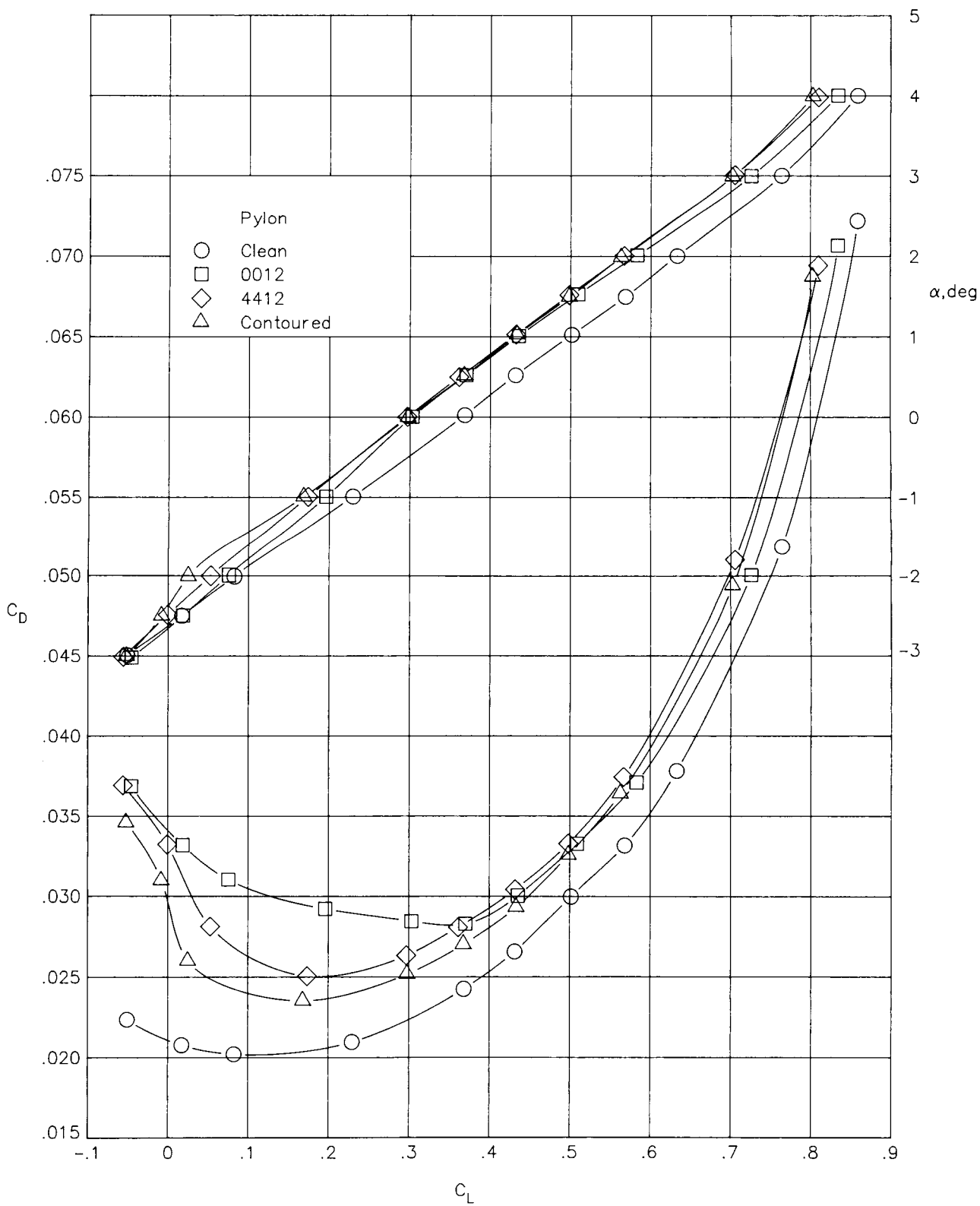
Figure 10. Concluded.

ORIGINAL PAGE IS
OF POOR QUALITY



(a) $M = 0.7$.

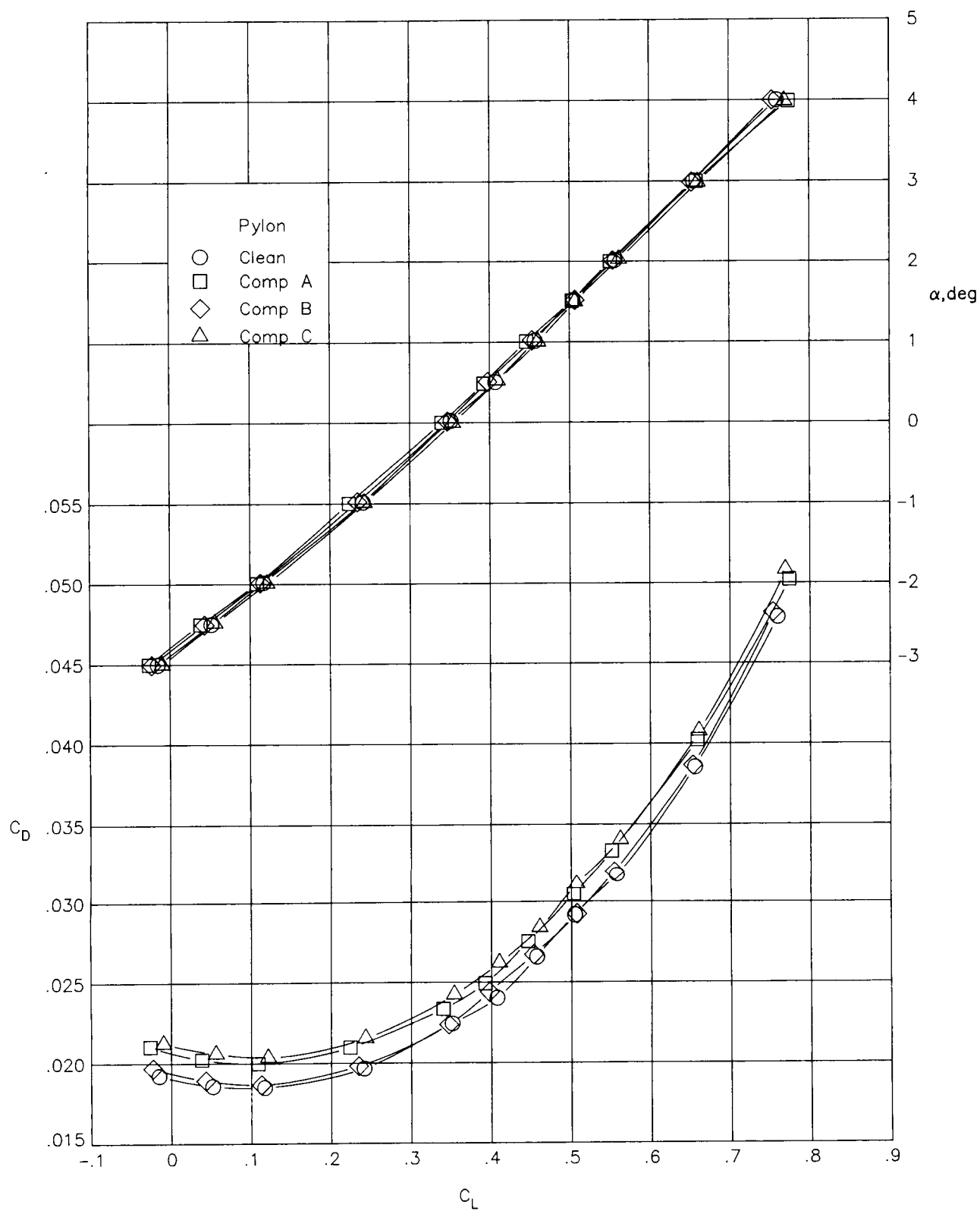
Figure 11. Effect of conventional pylon shape on aerodynamic characteristics for pylon toe angle of 0° .



(b) $M = 0.8$.

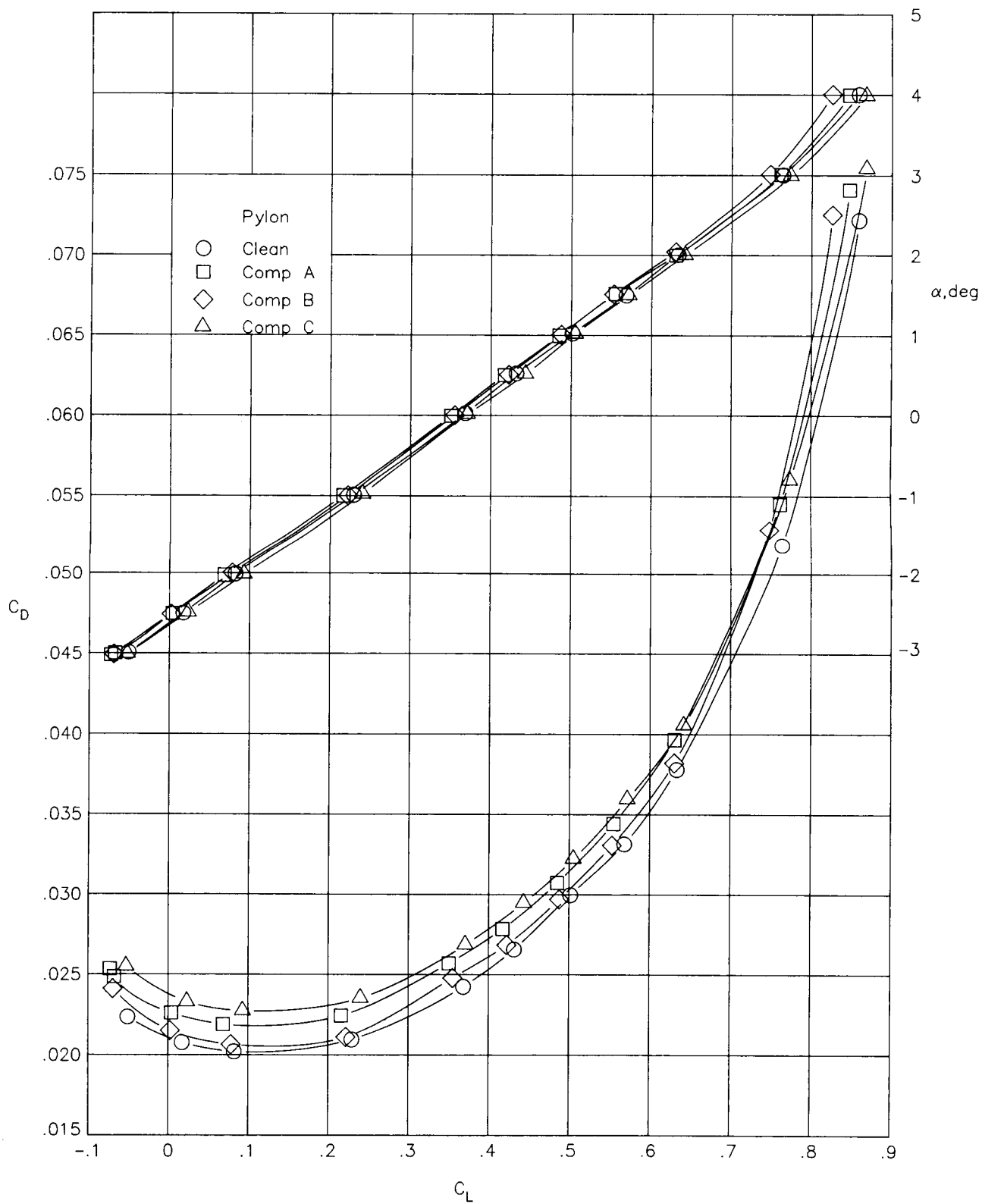
Figure 11. Concluded.

ORIGINAL PAGE IS
OF POOR QUALITY



(a) $M = 0.7$.

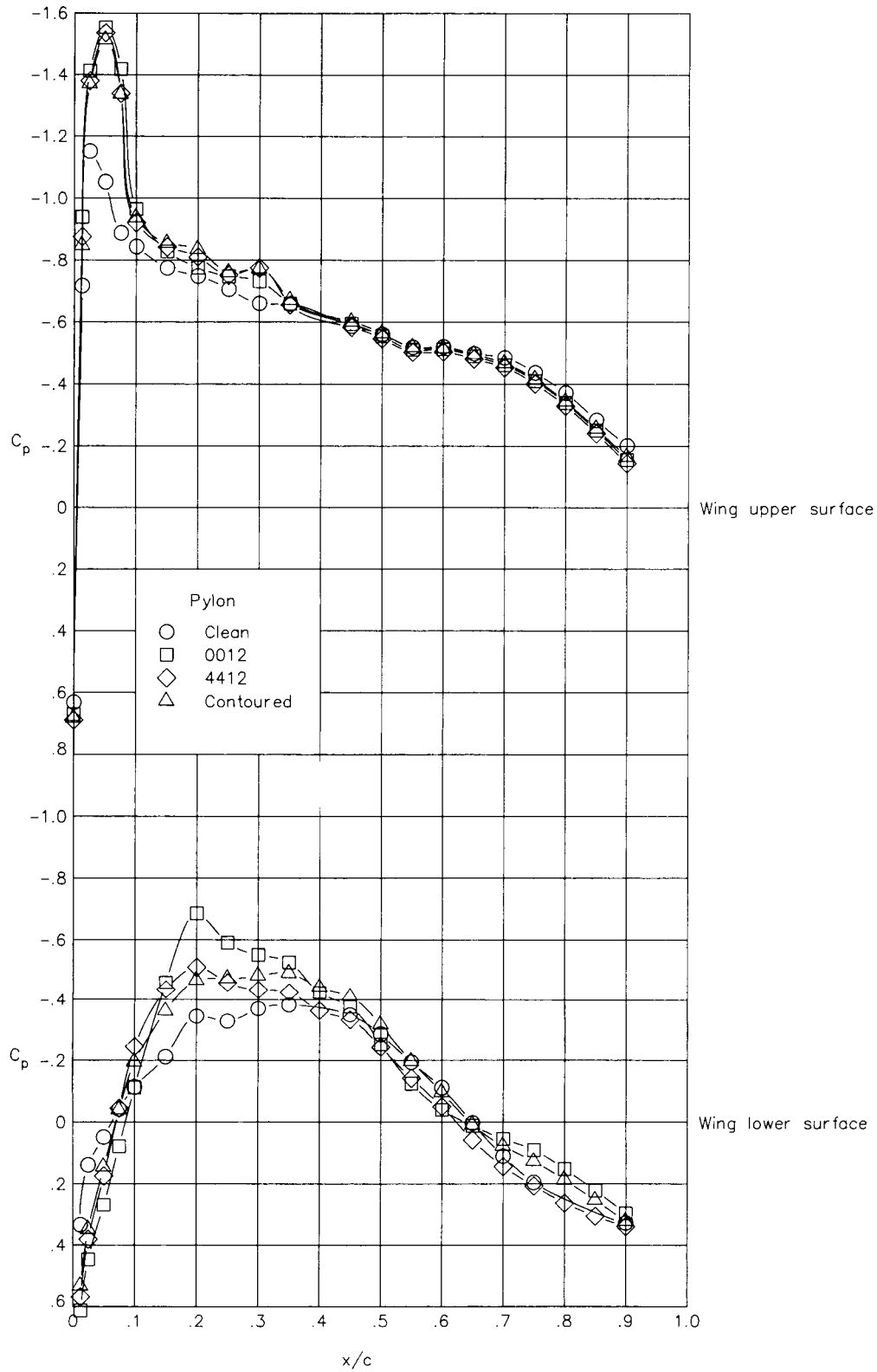
Figure 12. Effect of compression pylon shape on aerodynamic characteristics for pylon toe angle of 0° .



(b) $M = 0.8$.

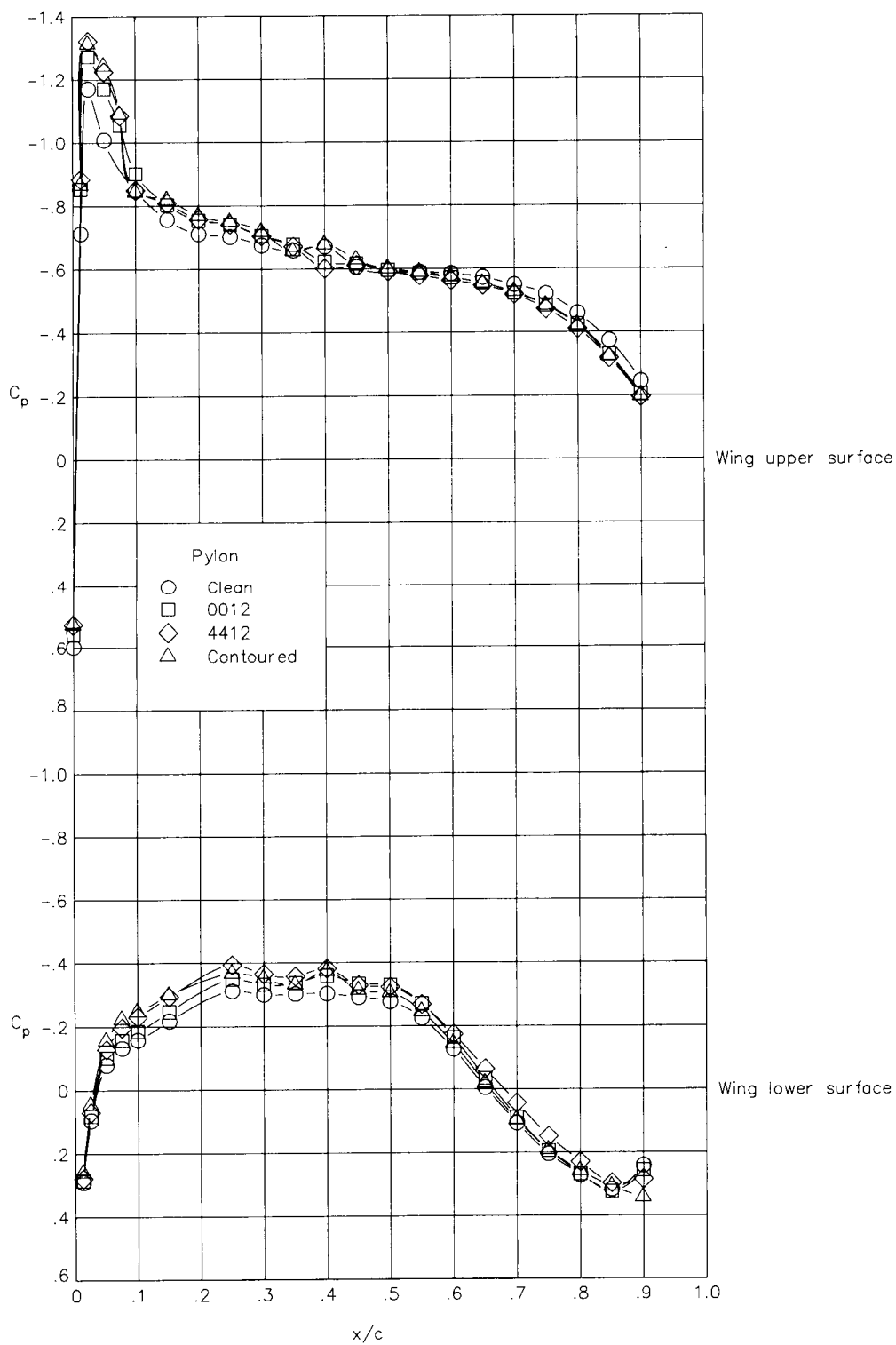
Figure 12. Concluded.

ORIGINAL PAGE IS
OF POOR QUALITY



(a) $M = 0.7$; inboard row.

Figure 13. Effect of conventional pylon shape on wing chordwise pressure distributions for pylon toe angle of 0° . $C_L \approx 0.5$.

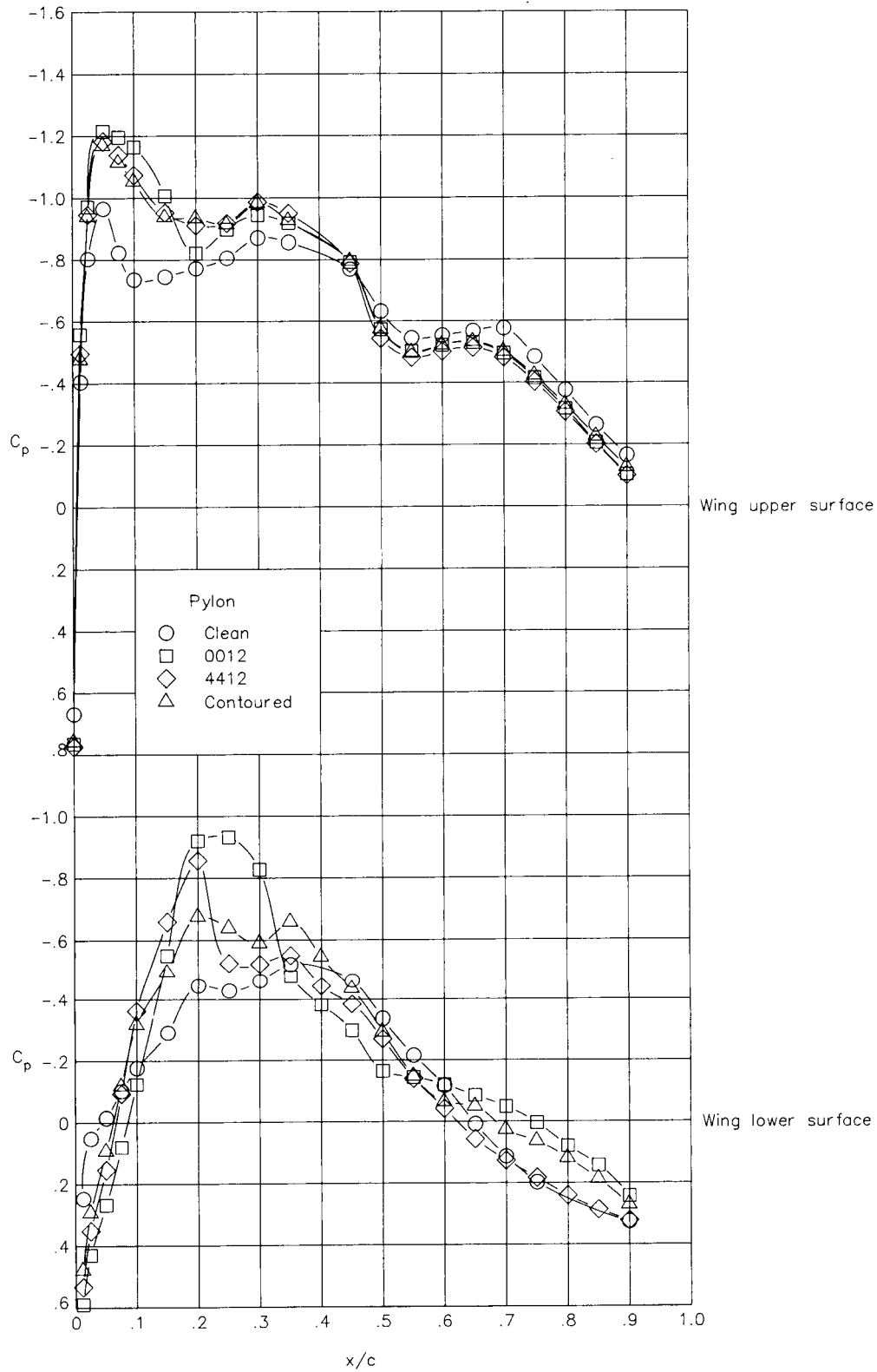


(b) $M = 0.7$; outboard row.

Figure 13. Continued.

ORIGINAL PAGE IS
OF POOR QUALITY

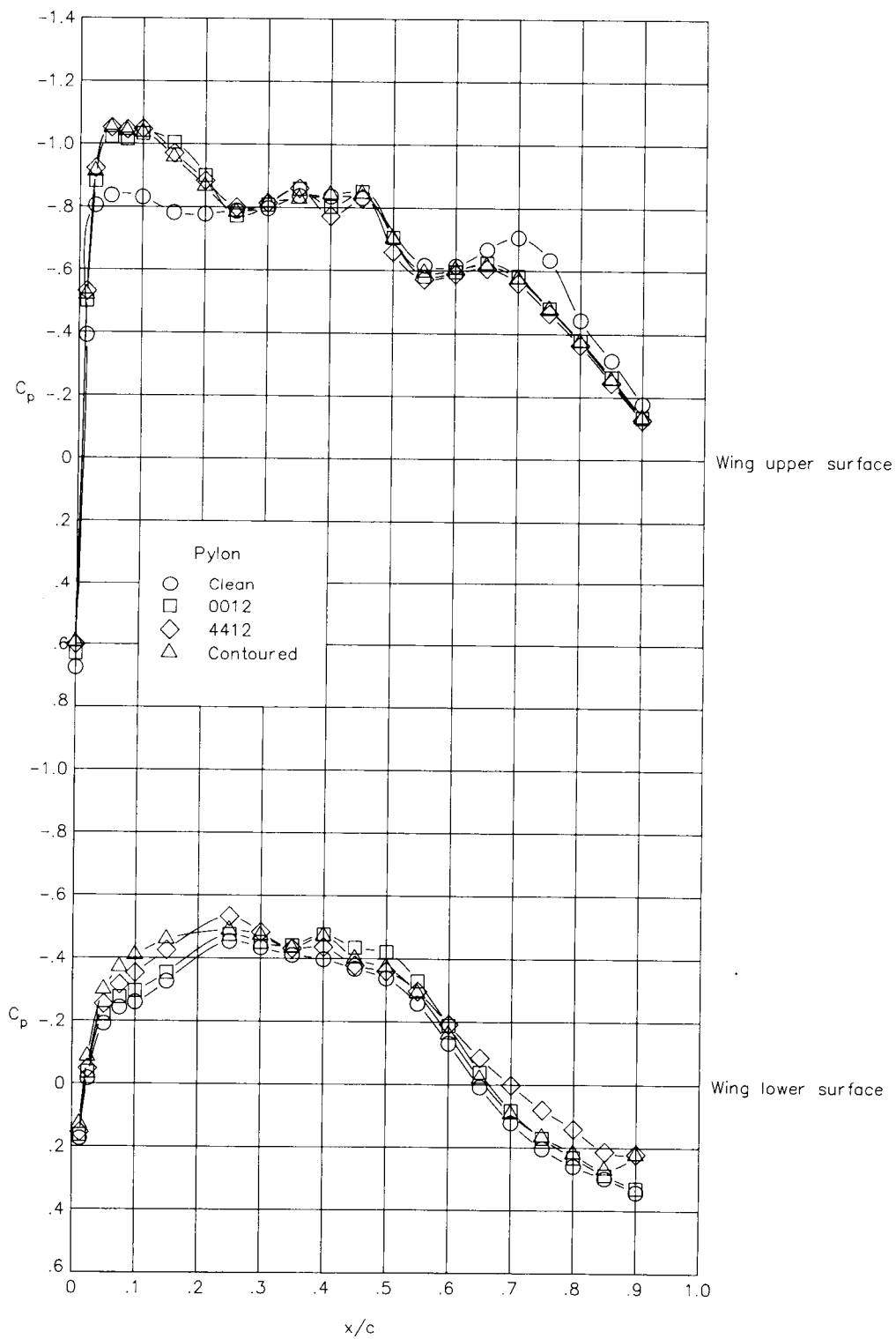
ORIGINAL PAGE IS
OF POOR QUALITY



(c) $M = 0.8$; inboard row.

Figure 13. Continued.

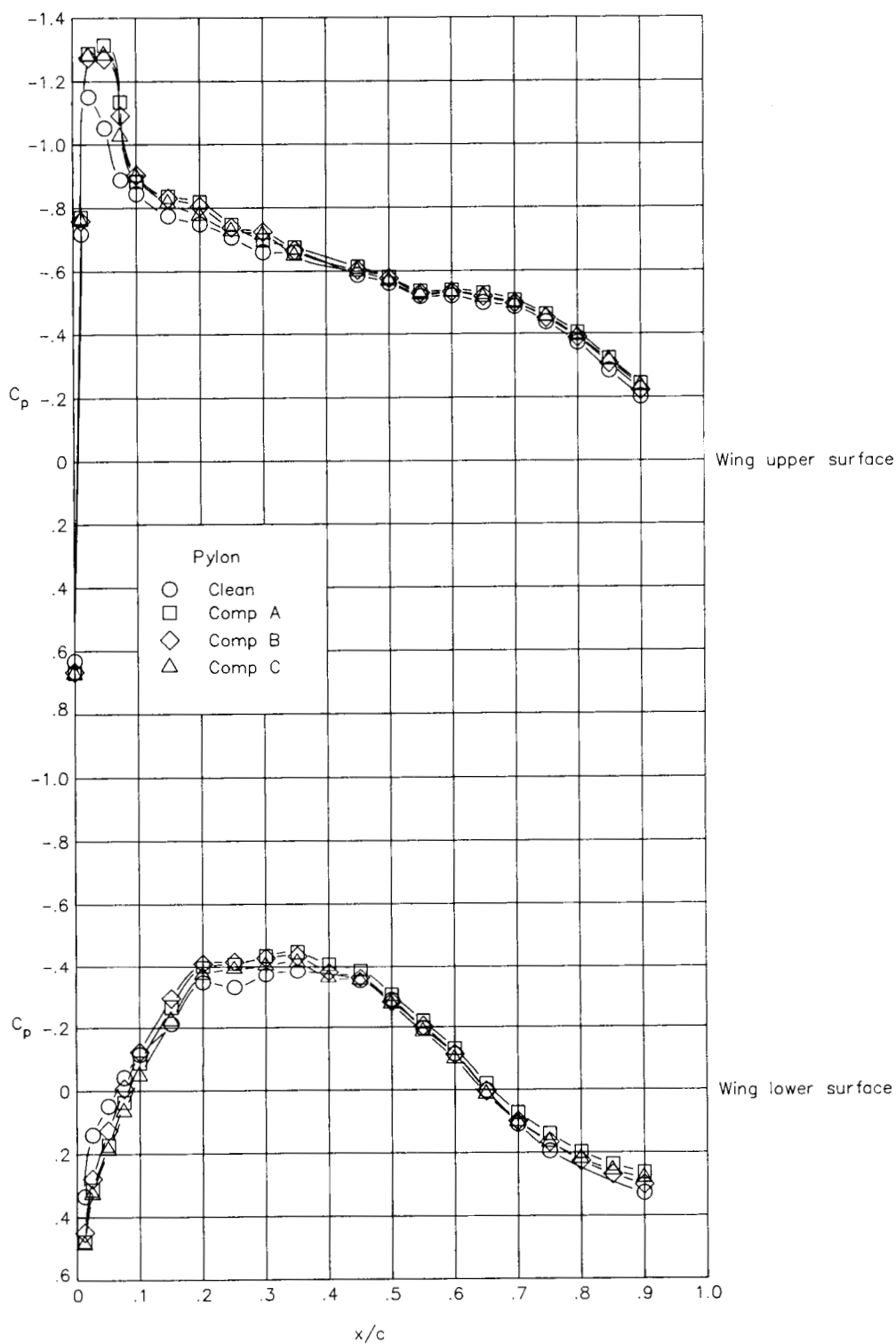
ORIGINAL PAGE IS
OF POOR QUALITY



(d) $M = 0.8$; outboard row.

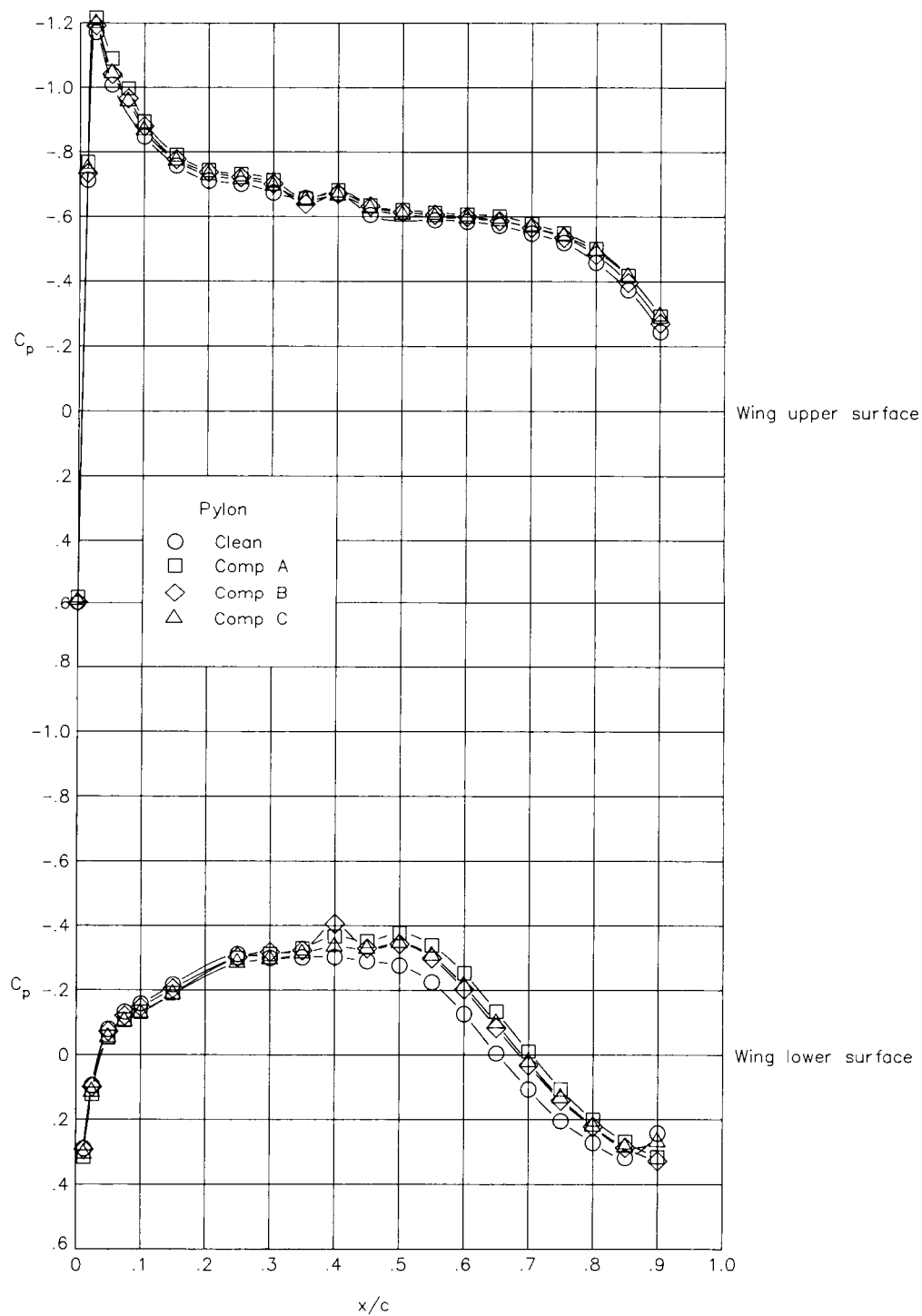
Figure 13. Concluded.

ORIGINAL PAGE IS
OF POOR QUALITY



(a) $M = 0.7$; inboard row.

Figure 14. Effect of compression pylon shape on wing chordwise pressure distributions for pylon toe angle of 0° . $C_L \approx 0.5$.

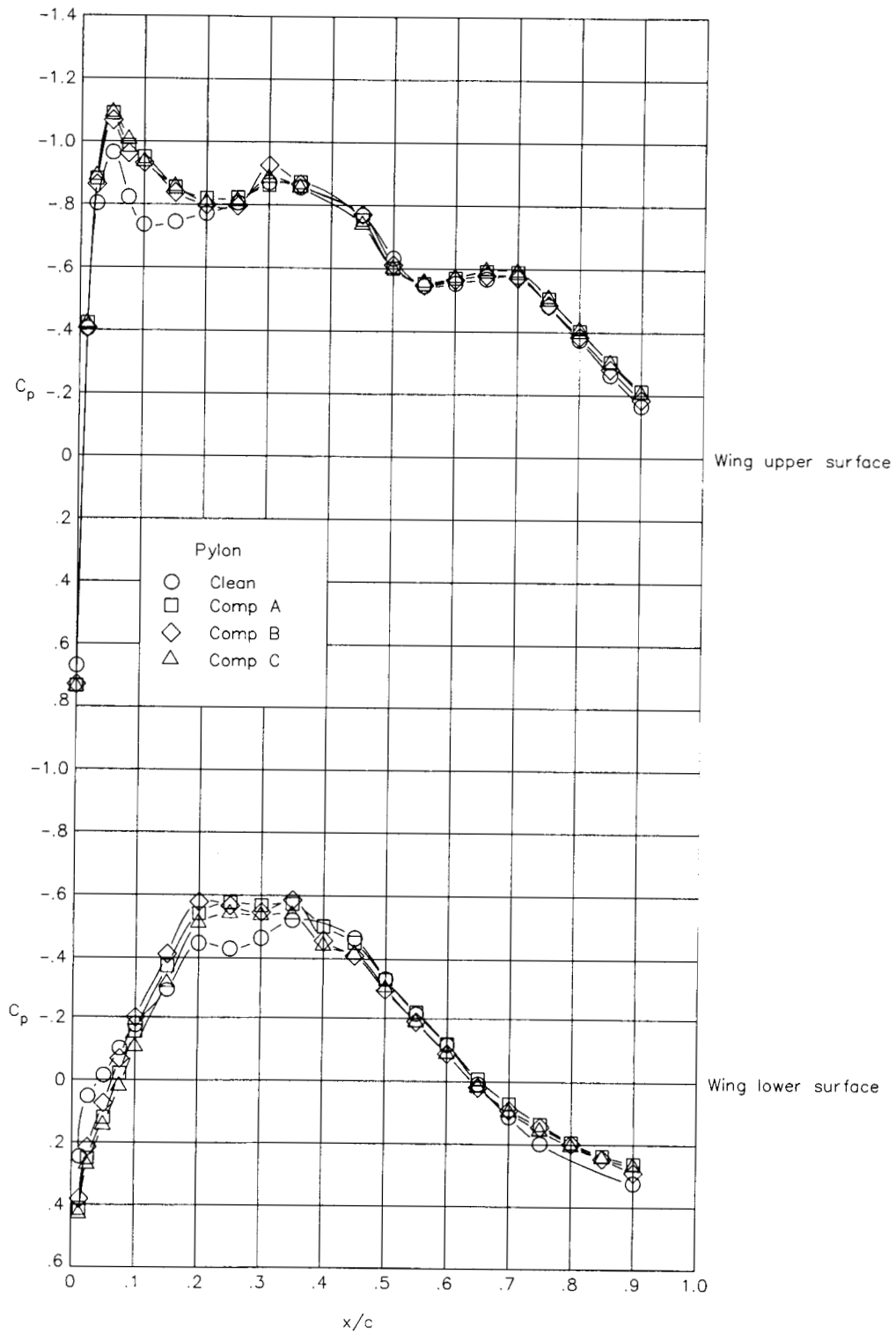


(b) $M = 0.7$; outboard row.

Figure 14. Continued.

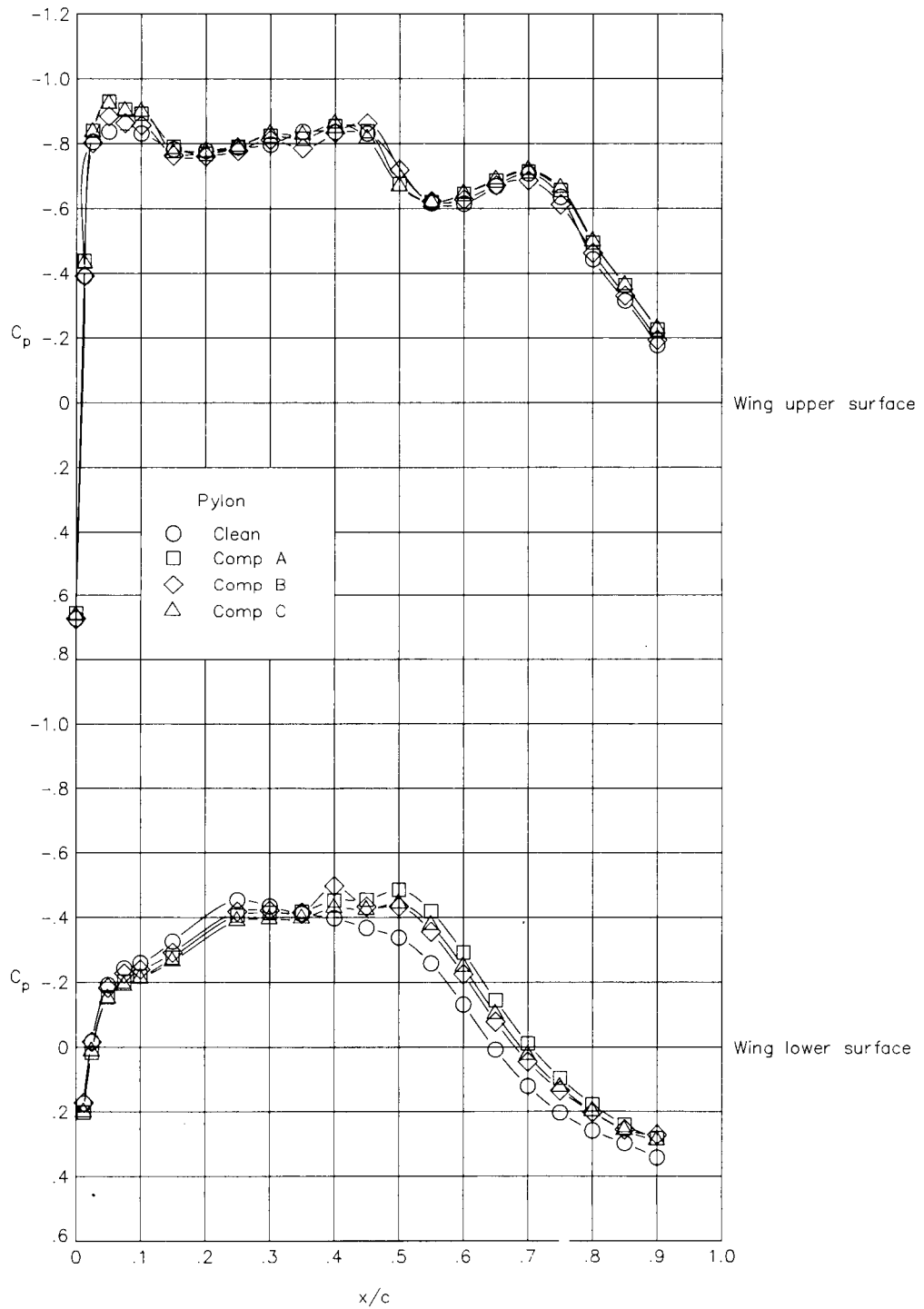
ORIGINAL PAGE IS
OF POOR QUALITY

ORIGINAL PAGE IS
OF POOR QUALITY



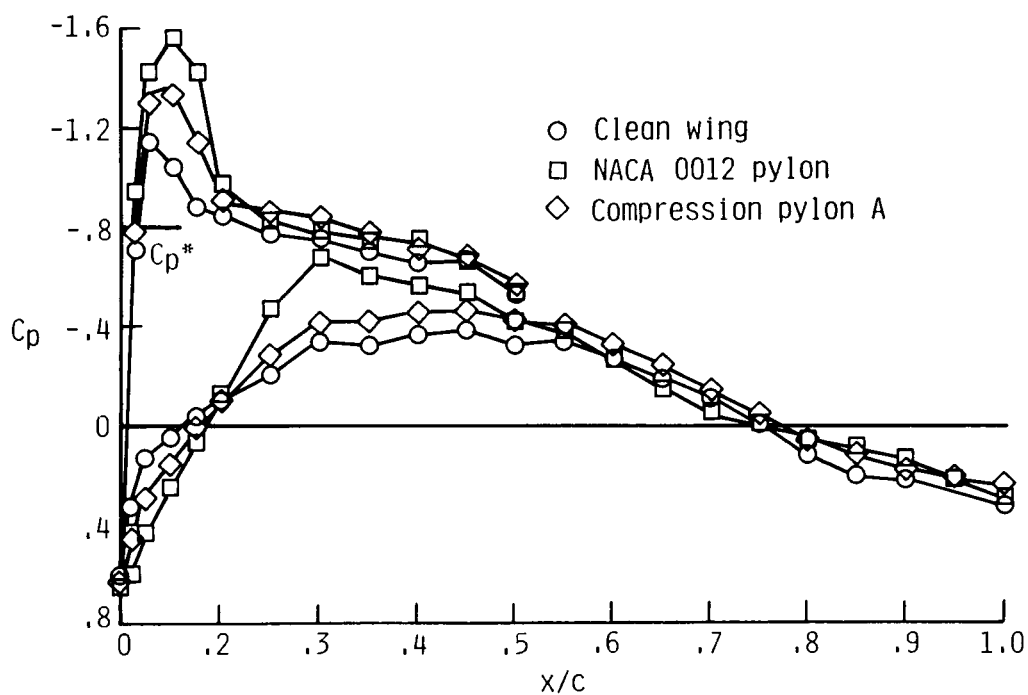
(c) $M = 0.8$; inboard row.

Figure 14. Continued.

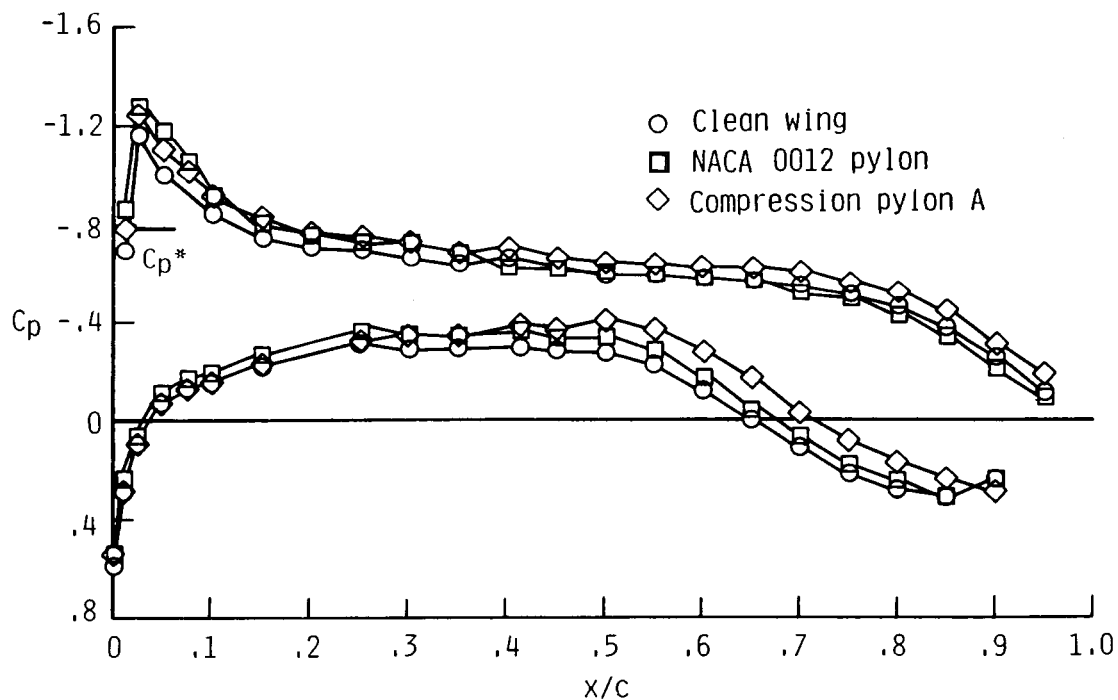


(d) $M = 0.8$; outboard row.

Figure 14. Concluded.

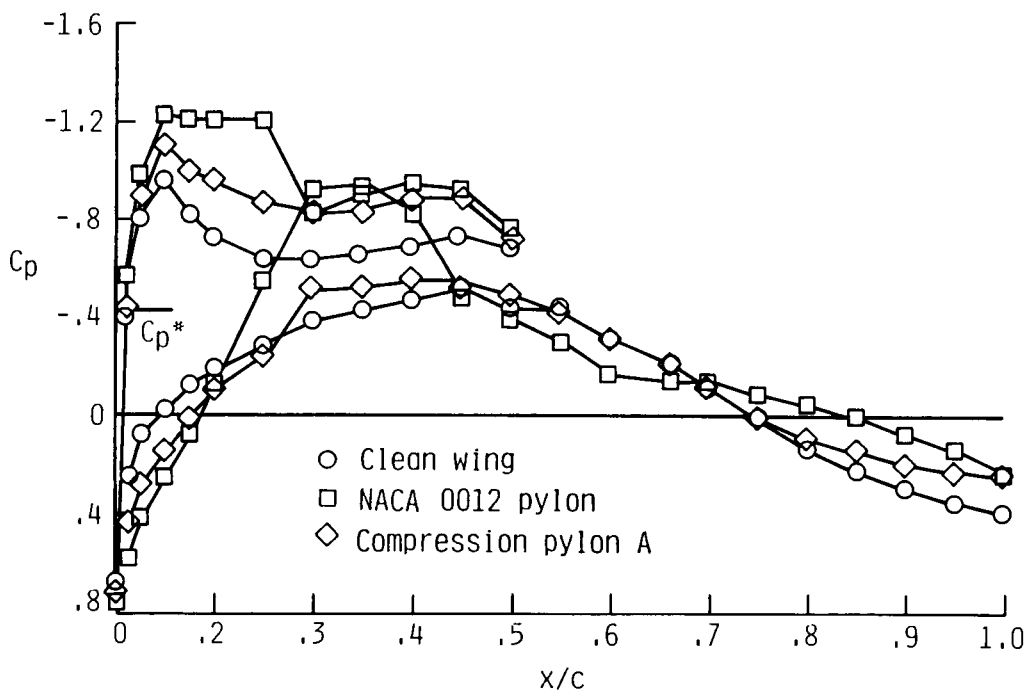


(a) $M = 0.7$; inboard row.



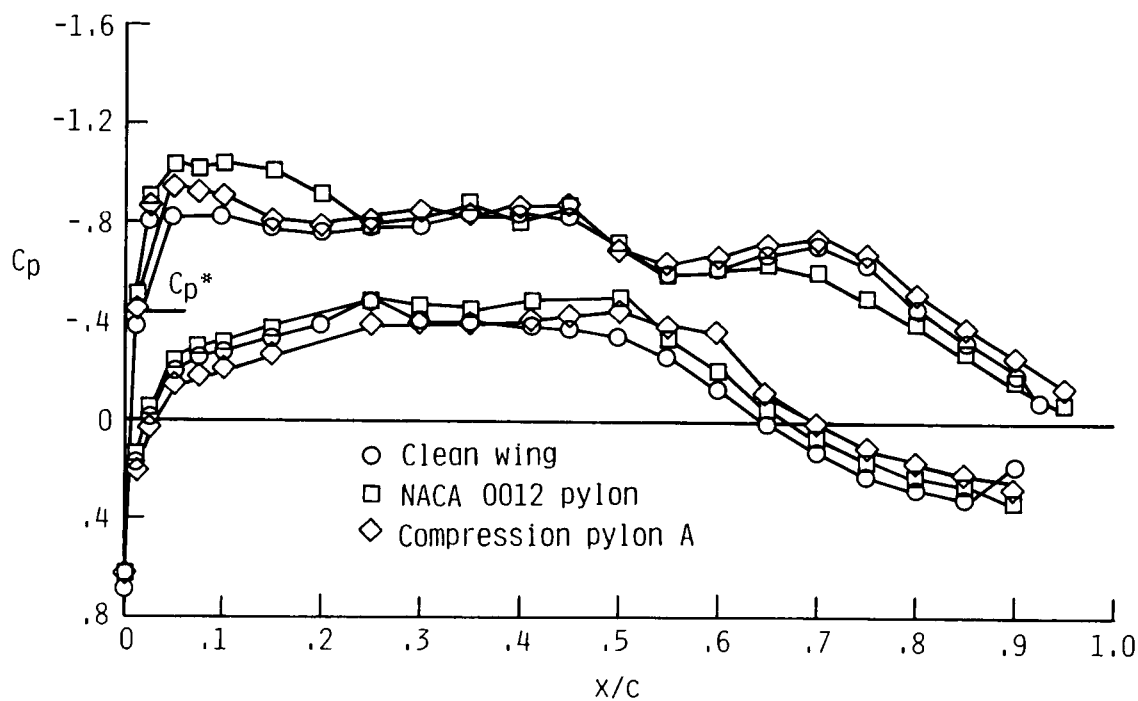
(b) $M = 0.7$; outboard row.

Figure 15. Effect of pylon shape on wing chordwise pressure distributions. $C_L \approx 0.5$.



(c) $M = 0.8$; inboard row.

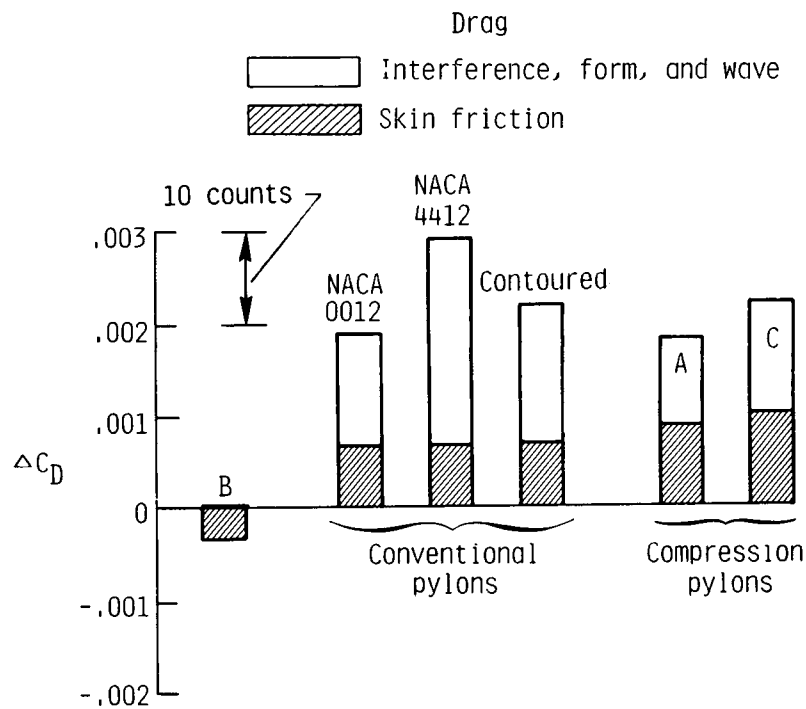
Figure 15. Continued.



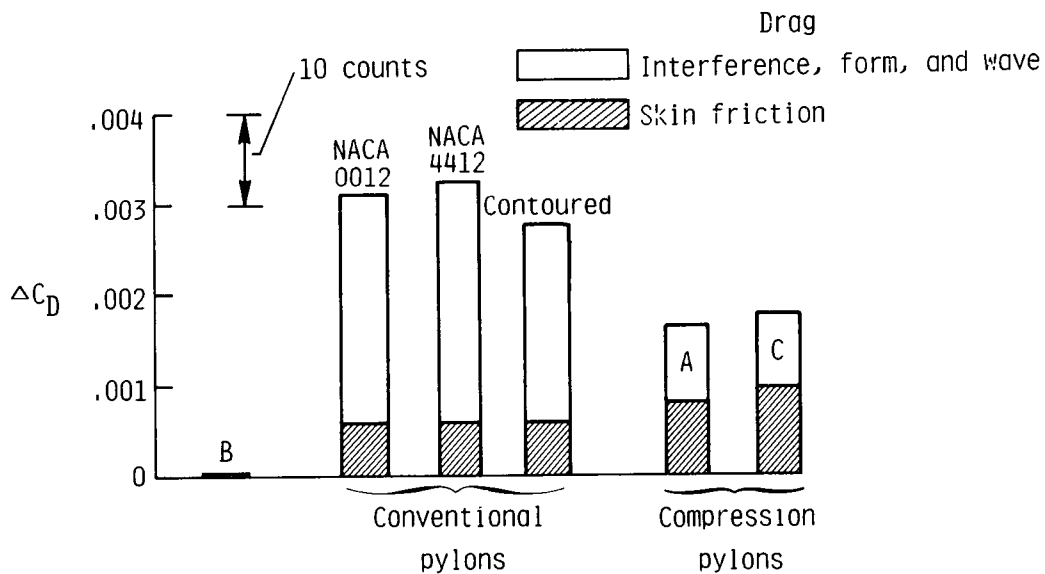
(d) $M = 0.8$; outboard row.

Figure 15. Concluded.

ORIGINAL PAGE IS
OF POOR QUALITY



(a) $M = 0.7$; $C_L \approx 0.51$.



(b) $M = 0.8$; $C_L \approx 0.45$.

Figure 16. Effect of pylon shape on incremental airplane drag for pylon toe angle of 0° .



Report Documentation Page

1. Report No. NASA TP-2877	2. Government Accession No.	3. Recipient's Catalog No.	
4. Title and Subtitle Integration Effects of Pylon Geometry on a High-Wing Transport Airplane		5. Report Date February 1989	
		6. Performing Organization Code	
7. Author(s) John R. Carlson and Milton Lamb		8. Performing Organization Report No. L-16489	
		10. Work Unit No. 535-03-01-01	
9. Performing Organization Name and Address NASA Langley Research Center Hampton, VA 23665-5225		11. Contract or Grant No.	
		13. Type of Report and Period Covered Technical Paper	
12. Sponsoring Agency Name and Address National Aeronautics and Space Administration Washington, DC 20546-0001		14. Sponsoring Agency Code	
15. Supplementary Notes			
16. Abstract An investigation was conducted in the Langley 16-Foot Transonic Tunnel to determine the installation effects of a series of pylons that had differing cross-sectional shapes on the pressure distributions and aerodynamic characteristics of a 1/24-scale high-wing transport. A new concept in pylon cross-sectional shape, the compression pylon, was developed and tested. The tests were conducted at Mach numbers of 0.7 and 0.8 at angles of attack from -3° to 4° with the pylons installed at various toe angles between 5° inboard and 5° outboard. Results of this study indicate that the installed drag was lowest for the compression pylon design, which kept the flow under the wing in the pylon-wing junction comparable to the clean wing velocities.			
17. Key Words (Suggested by Authors(s)) Airframe-propulsion integration Compression pylons Nacelle-ptylon wing integration Air-breathing propulsion Transport airplane Transonic aerodynamics		18. Distribution Statement Unclassified-Unlimited Subject Category 02	
19. Security Classif. (of this report) Unclassified	20. Security Classif. (of this page) Unclassified	21. No. of Pages 76	22. Price A05